Back to Back Active Power Filter for Multi-Generator Power Architecture with Reduced dc-link Capacitor

Jongwan Kim

Dissertation submitted to the faculty of the Virginia Polytechnic Institute and State University in partial fulfillment of the requirements for the degree of

Doctor of Philosophy
In
Electrical Engineering

Jih-Sheng Lai
Rolando Burgos
Steve C Southward
Daniel J Stilwell
Wei Zhou

December 5th. 2019
Blacksburg, Virginia

Keywords: harmonic elimination, 3 phase active power filter, multi-pulse converter, shipboard power system

Back to Back Active Power Filter for Multi-Generator Power Architecture with Reduced dc-link Capacitor

Jongwan Kim

ABSTRACT

Multi-pulse converters have been widely used for a multi-megawatt scale power generating system to comply with harmonic regulations. Among all types of multi-pulse converters, a 12-pulse converter is the most widely used due to the simple structure, which consists of a delta-delta (Δ-Δ) and a delta-wye (Δ-Y) phase-shift transformer pair and it effectively mitigates undesirable harmonics from the nonlinear load.

In the early 2000s, a shunt type passive front-end for a shipboard power system was proposed. By shunting the two gensets with 30° phase angle difference, a single phase-shift transformer effectively eliminates 5^{th} and 7^{th} harmonics. It achieves a significant size and weight reduction compared to a 12-pulse converter while keep the comparable harmonic cancellation performance. Recently, a hybrid type front-end was proposed. On top of the passive front-end, 3 phase active power filter was added and an additional harmonic cancellation was achieved to further eliminate 11^{th} and 13^{th} harmonics. However, the performance of both the passive and hybrid type front-end are highly dependent on the size of the line reactor in ac mains.

A back to back active power filter is proposed in this dissertation to replace Y-Δ transformer in the multi-generator power architecture. The proposed front-end does not include phase-shift transformer and the size and the weight of the overall front-end can be significantly reduced. Due to the active harmonic compensation, the back to back front-

end achieves better power quality and the line reactor dependency is improved. The number of required dc-link capacitors is reduced by half by introducing a back to back configuration and the capacitor size is reduced by adjusting the phase angle difference of genset to cancel out the most significant voltage harmonics in the shared dc-link bus.

The overview of the existing shunt type front-end is provided and the concept of back to back active power filter is validated by simulation and prototype hardware. The comparison between existing front-end and the proposed front-end is provided to highlight the superior performance of back to back active front-end. The dc-link bus current and voltage ripple analysis is provided to explain the dc-link ripple reduction mechanism.

Back to Back Active Power Filter for Multi-Generator Power Architecture with Reduced dc-link Capacitor

Jongwan Kim

GENERAL AUDIENCE ABSTRACT

The transportation electrification has gained more and more attention due to its smaller carbon dioxide emission, better fuel efficiency. The recent advances in power devices, microcontrollers, and transducers accelerate the electrification of transportation. This trend is shown in the propulsion system in marine transport as well and the electric propulsion system has been widely used to meet the strict environmental regulations.

However, the non-linear circuit components such as capacitor and diode in the electric propulsion system draw non-linear current and significantly deteriorate power quality and lead to critical problems such as reduced life span of circuit components Accordingly, a front-end is required to improve power quality. Also, it is desired to have compact and lightweight front-end for installation flexibility and fuel efficiency improvement.

In this dissertation, several front-ends using a phase-shift transformer are reviewed and a detailed analysis is provided to help understand the harmonic cancellation principle of the existing front-end through equivalent circuit analysis, quantitative analysis, and a phasor diagram representation. Based on the analysis of the existing front-ends and shipboard power architecture, lightweight and high-performance front-end is proposed and verified by simulation and prototype hardware.

The performance, size comparison between existing front-end and the proposed front-end is provided to show the advantage of the proposed front-end.

To my wife and son
Hyojung Lee
Jace Jisoo Kim

To my parents
Ju Hyun Kim
Yoon Sook Kwak

To my parents-in-law
Ho Sung Lee
Sung Hee Kim

ACKNOWLEDGMENTS

First of all, I would like to express my genuine gratitude to my advisor, Dr. Jih-sheng Lai, for his guidance and support throughout my entire Ph.D program. His insight and vision have guided me to solve many of the engineering challenges and eventually led me to become a professional engineer. I sincerely respect his academic professionalism and passionate attitude toward life.

I would like to thank my advisory committee Dr. Southward, Dr. Burgos, Dr. Zhou, and Dr. Stilwell for their valuable comments and suggestions throughout my pursuit of Ph.D. degree.

It has been a great pleasure for me to be a member of Future Energy Electronics Center (FEEC). I would like to thank all my colleagues at FEEC. Especially I thank Dr. Michael Jung-Muk Choi and Dr. Sengryul Moon who provided me valuable pieces of advice and wisdom. Also, I thank Dr. Jongwoo Kim and Mr. Moonhyun Lee for sharing their knowledge and experience. The refreshing times that I had with them relieved me a lot.

I thank Dr. Zhen Yu, Mr. Shamim Choudhury, and Dr. Manish Bhardwaj for providing me an internship opportunity at Texas Instruments. Their mentoring and advice extended my knowledge and skill.

With my heartfelt respect, I thank my parents, Mr. Ju Hyun Kim and Dr. Yoon Sook Kwak. Their love, support and dedication always have encouraged and guided me in the right direction in every aspect of my life. I sincerely appreciate my parents-in-law, Mr. Ho Sung Lee and Mrs. Sung Hee Kim for their commitment and faith in my ability. I thank all

of my family for their love and support and will always remember my grandmother, Mrs. Jung Suk Noh for her everlasting love.

Last but not least, I would like to express my genuine appreciation to my wife, Hyojung Lee for her commitment and sacrifice. I will never forget the days that we had in Blacksburg. Without her unconditional love and support, I could not finish my long journey at Virginia Tech. Lastly I thank my beloved son Jace Jisoo Kim who brought me the joy of being a father.

Blacksburg is very special to me. It is the place where I started my marriage, my son was born, and I started and finished my doctoral degree. 4 years at Blacksburg was not always easy but it was the most meaningful time in my life. I will always remember the invaluable lessons and memories from Virginia Tech.

Jongwan Kim

Dec 15, 2019, in Houston

Table of Contents

List of Figures

List of Tables

Chapter 1

Introduction

1.1 Overview of shipboard power system

With the high demand for the alternative propulsion system, which provides smaller greenhouse gas emission and better fuel efficiency, an electric propulsion system has gained more and more attention. In addition to the lower energy consumption and environmental benefits, the electric propulsion system also provides higher flexibility in installation, better comfort due to reduced shaft noise and vibration. The aforementioned advantages have made the shipbuilding industry move toward more electric propulsion systems and eventually, an all-electric propulsion system dominates the market with the states of the art power electronics technologies.

Fig.1 describes the power architecture of the naval shipboard, Queen Elizabeth II [1].

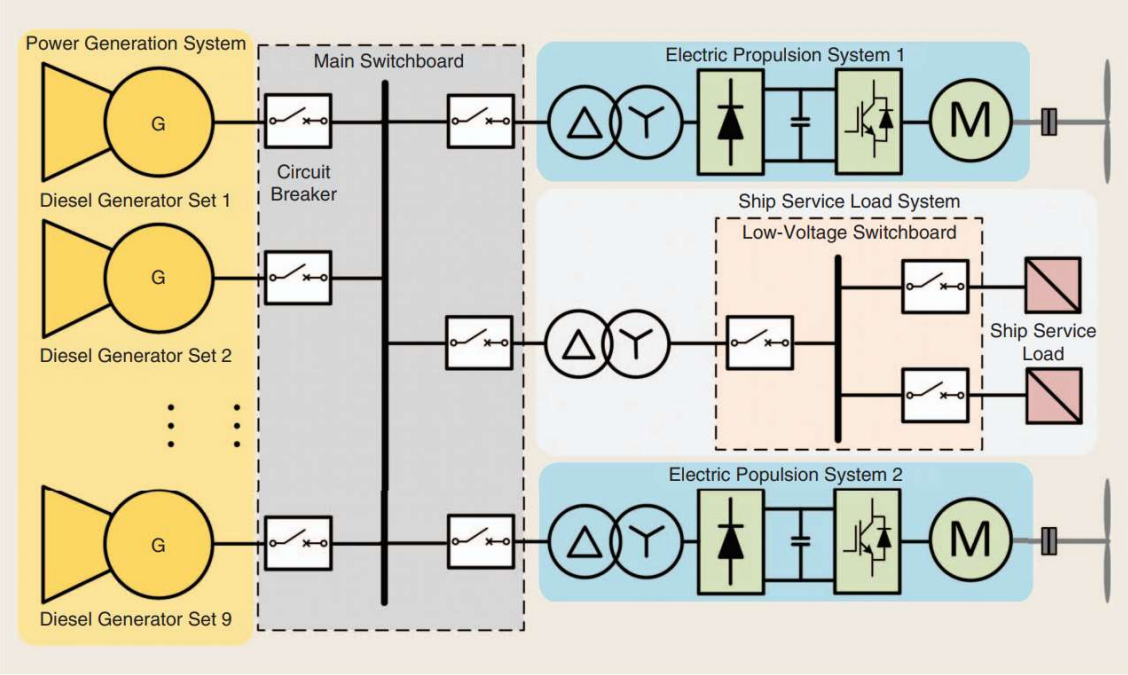

Fig. 1-1 The diesel-electric shipboard power system of the Queen Elizabeth II [1]

As the power generation system supplies all the hotel service load and electric propulsion systems, it is known as an integrated power system (IPS). The most critical property of IPS is the fail-safe operation. Large scale shipboard has multiple diesel engine-generator sets as system redundancy and provides power even in the event of several genset failures. Typically, 4 gensets are installed in the commercial marine transport and naval ship such as Queen Elizabeth II has 9 gensets to maximize the reliability. The arrangement of the 4 genset based hybrid propulsion system is shown in Fig. 1-2 [2].

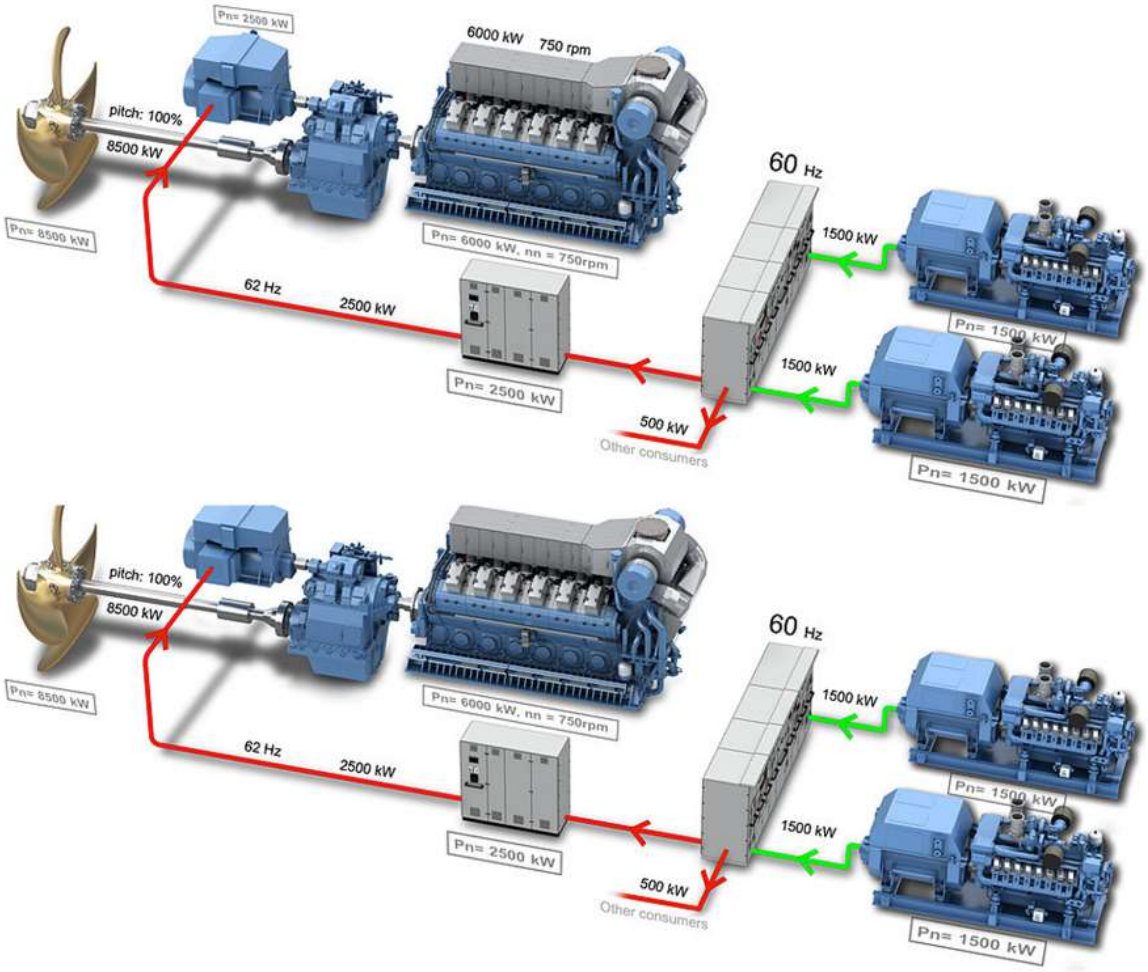

Fig. 1-2. The arrangement of 4 genset-based hybrid-electric propulsion system [2]

The main propulsion system and ship service loads include multiple rectifiers, switch-mode power supplies (SMPSs), and inverters that draw a significant non-linear harmonic current in ac

mains. The non-linear currents flowing through the network eventually induce a harmonic voltage distortion as well. The negative impacts of harmonic current and voltage are:

- Excessive heating and vibration in motor and generator
- Additional heating in magnetic components
- Harmonic resonance in the network
- False tripping of a protection circuit
- Reduced lifespan in power electronics device and magnetic components
- Poor power factor, crest factor

To avoid the severe impact of harmonic distortion on the shipboard power system, harmonic regulations and guidelines were established by several organizations. MIL-STD -1399 specified that the individual harmonic current distortion (THDi) can not exceed 3% of fundamental current at full load. IEEE STD 519 [3] provided a detailed guideline for harmonic regulations. Table 1 provides suggested total harmonic distortion of the voltage (THDv) in different bus voltage range.

Table 1-1. Voltage distortion limits [3]

Bus voltage at PCC	**Individual harmonic (%)**	**Total Harmonic Distortion (THD)**
$V \leq 1.0$ kV	5.0	8.0
$1.0 < V \leq 69$ kV	3.0	5.0
69 kV $< V \leq 161$ kV	1.5	2.5
161kV $< V$	1.0	1.5

In IEEE STD 519, the criteria for harmonic current distortion is total demand distortion (TDD) instead of total harmonic distortion of current (THDi). TDD is calculated as

$$TDD = \frac{\sum_{h=2}^{50} \sqrt{i_h^2}}{i_L} \tag{1.1.1}$$

As TDD is calculated based on the maximum load current i_L, it can be interpreted as THD at maximum load. The benefit of TDD is that it provides a consistent index regardless of the load size. Tables 1-1, 1-2, and 1-3 show harmonic current limit for the individual harmonic components and TDD with respect to the ratio of the short circuit current i_{SC} and the maximum load current i_L [3].

Table 1-2. Current distortion limits for systems rated 120 V through 69 kV [3]

Maximum harmonic current distortion in percent of I_L						
Individual harmonic order (odd harmonics)						
I_{SC}/I_L	$35 \le h \le 50$	$35 \le h \le 50$	$35 \le h \le 50$	$35 \le h \le 50$	$35 \le h \le 50$	**TDD**
<20	4.0	2.0	1.5	0.6	0.3	5.0
20<50	7.0	3.5	2.5	1.0	0.5	8.0
50<100	10.0	4.5	4.0	1.5	0.7	12.0
100<1000	12.0	5.5	5.0	2.0	1.0	15.0
>1000	15.0	7.0	6.0	2.5	1.4	20.0

Table 1-3. Current distortion limits for systems rated 69 kV through 161 kV [3]

Maximum harmonic current distortion in percent of I_L						
Individual harmonic order (odd harmonics)						
I_{SC}/I_L	$35 \le h \le 50$	$35 \le h \le 50$	$35 \le h \le 50$	$35 \le h \le 50$	$35 \le h \le 50$	**TDD**
<20	2.0	1.0	0.75	0.3	0.15	2.5
20<50	3.5	1.75	1.25	0.5	0.25	4.0
50<100	5.0	2.25	2.0	0.75	0.35	6.0
100<1000	6.0	2.75	2.5	1.0	0.5	7.5
>1000	7.5	3.5	3.0	1.25	0.7	10.0

Table 1-4. Current distortion limits for systems rated > 161 kV [3]

Maximum harmonic current distortion in percent of I_L						
Individual harmonic order (odd harmonics)						
I_{SC}/I_L	$35 \le h \le 50$	$35 \le h \le 50$	$35 \le h \le 50$	$35 \le h \le 50$	$35 \le h \le 50$	TDD
<20	1.0	0.5	0.38	0.15	0.1	1.5
20<50	2.0	1.0	0.75	0.3	0.15	2.5
50<100	3.0	1.5	1.15	0.45	0.22	3.75

Also, American Bureau of Shipping (ABS) published a harmonic regulation guideline [4], which provides a detailed explanation from equipment installation to harmonic mitigation solutions. Referred to ABS guideline, THDv can not exceed 5% and individual harmonic voltage distortion can not exceed 3% of fundamental voltage.

To meet these strict harmonic requirements, a front-end has to be installed. The following section provides the existing passive front-end for low and medium voltage marine transport.

1.2 Existing passive front-ends for harmonic reduction

1.2.1 Multi-pulse converter

The early concept of the 12-pulse converter was shown in [5-7] and has been commonly used for a large scale power system. It is the most popular front-end in marine transport owing to a simple and rugged structure. The primary side of the transformer pair has either delta (Δ) or wye (Y) connection and the secondary sides have both delta (Δ) and wye (Y) connections, which will induce 30 degree phase shift. In this configuration, $h = 6k \pm 1$ ($k = 1, 3, 5, \cdots$) harmonics in primary sides are eliminated. As 5^{th} and 7^{th} harmonics are the most significant harmonic contents, a 12-pulse converter significantly improves the power quality in ac mains. By increasing the number of phase-shift transformer pairs the harmonic cancellation performance of the multi-pulse converter is improved [8]. In [9], more than 200 studies on multi-pulse converters were reviewed and analyzed. The multi-pulse converters effectively cancel unwanted harmonics from the non-linear load. However, the series phase-shift transformer pairs increase the size and weight of the system. To overcome the drawback of the multi-pulse rectifier, a hybrid front-end was proposed [10-14]. Also, an autotransformer was employed to reduce the overall size of the front-end [15-18].

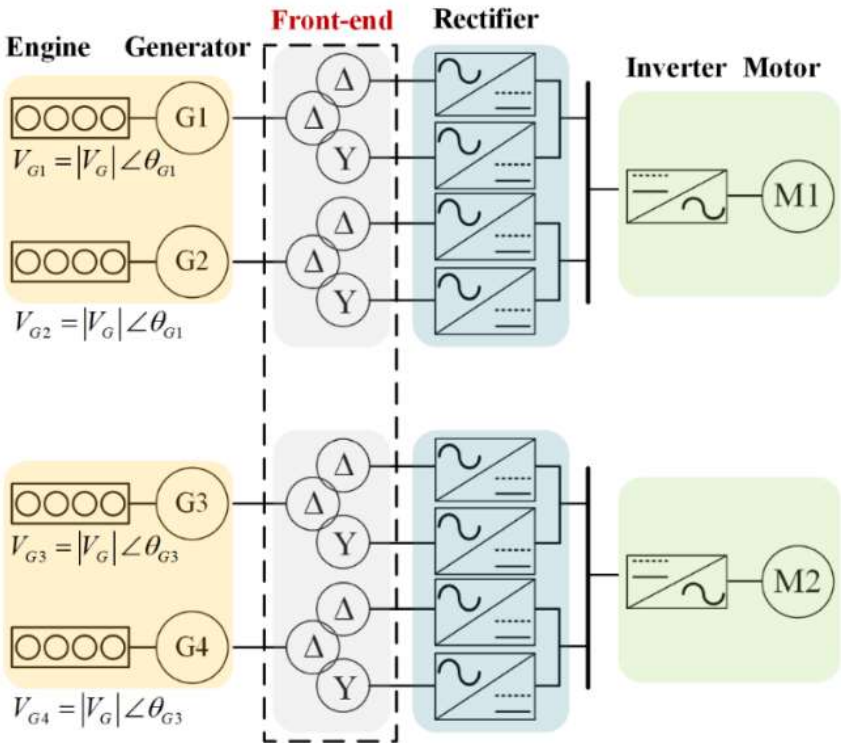

Fig. 1-3 Single line diagram of 12 pulse converter

1.2.2 Shunt phase-shift transformer rectifier

In the early 2000s, a shunt Y-Δ transformer was proposed. It shunts the two generators with 30° phase-shift and eliminates 5th and 7th harmonics [19]. It has been applied to a medium and low voltage shipboard power system where multiple gensets are available for the system redundancy [20-22].

Fig. 1-4 shows the single line diagram of the shunt phase-shift transformer. A single phase-shift transformer is required for every two gensets. Therefore the number of requires transformers is reduced by half. In addition, VA capability of the transformer is significantly reduced [23].

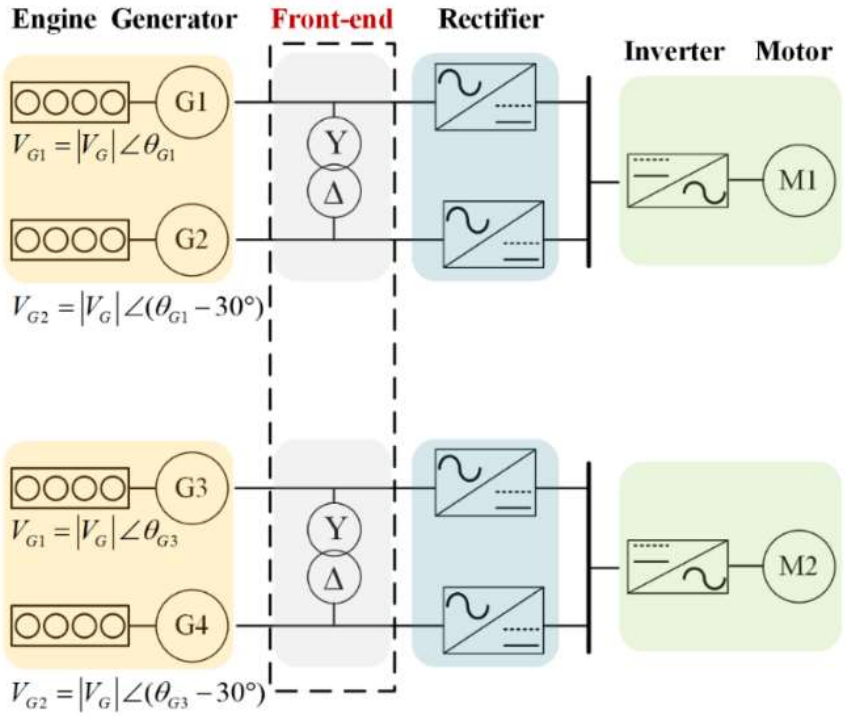

Fig. 1-4 Single line diagram of shunt phase-shift transformer rectifier

The performance of the shunt-phase shift transformer rectifier was verified in [24] and the experimental results showed that it effectively eliminated 5th and 7th harmonics in ac mains with much reduced low-frequency magnetics.

The number of transformers and ratings for 12 pulse converter and the shunt phase-shift transformer rectifier for 4 MW power system are shown in Table 1-5.

Table 1-5. Comparison between the 12-pulse converter and shunt phase-shift transformer rectifier

Component	12-pulse Converter	Shunt Ph-shift TX
TX type	Y-Y and Y-Δ pair	Y-Δ
VA rating	1.1 MVA	0.275 MVA
# of required TX	2	1
Total VA rating	2.2 MVA	0.275 MVA
Genset synchronization with phase shift angle	NO	YES
Harmonic Cancellation Principle	The summation of i_{LY} and $i_{L\Delta}$	The differential of i_{L1} and i_{L2}

12 pulse converter is fully engaged in the fundamental power transfer from genset to VFD and therefore, VA rating for the transformer has to be larger than the maximum generator output. However, the shunt type front end is only engaged in the harmonic currents and the required VA rating can be noticeably reduced. Referred to [25], the advantages of the shunt phase-shift transformer front-end are

- Size reduction in phase-shift transformer (87.5% reduction)
- Significant savings in space and weight (35-40% reduction)
- Transformer loss reduction (5-7% reduction)
- Overall fuel efficiency improvement (9% improvement)

The prerequisite requirement of 30° phase-shifted condition can be easily achieved in IPS where the individual genset phase angle is controllable.

1.3 The objective and scope of the dissertation

Shunt type front-end performs as comparable to 12 pulse converter with significantly reduced transformer size. However, there are two major drawbacks. First of all, the harmonic cancellation performance is largely dependent on the ratio between transformer leakage inductance and a line reactor in ac mains. Second, similar to the 12-pulse converter, it requires additional transformers to eliminate higher-order harmonics such as 11^{th} and 13^{th} components, which will increase the system size and cost.

The objective of this research is to propose an active shunt type front-end using SiC devices that further improve the harmonic cancellation performance without increasing the size and weight of the system.

Active harmonic compensation has been demonstrated excellent harmonic cancellation performance but it has not been widely adopted due to high cost and power device performance

limitations such as switching frequency and the maximum blocking voltage. The advent of wideband gap devices such as silicon carbide (SiC) and gallium nitride (GaN) overcome critical issues and opened the new era of power electronics owing to their superior performance. These devices make active front-end as a realistic and practical solution for the medium and low voltage power systems. The radar chart of Si, SiC, and GaN devices are provided in Fig. 1-7 [26]. In almost every aspect, wide bandgap devices outperform Si device.

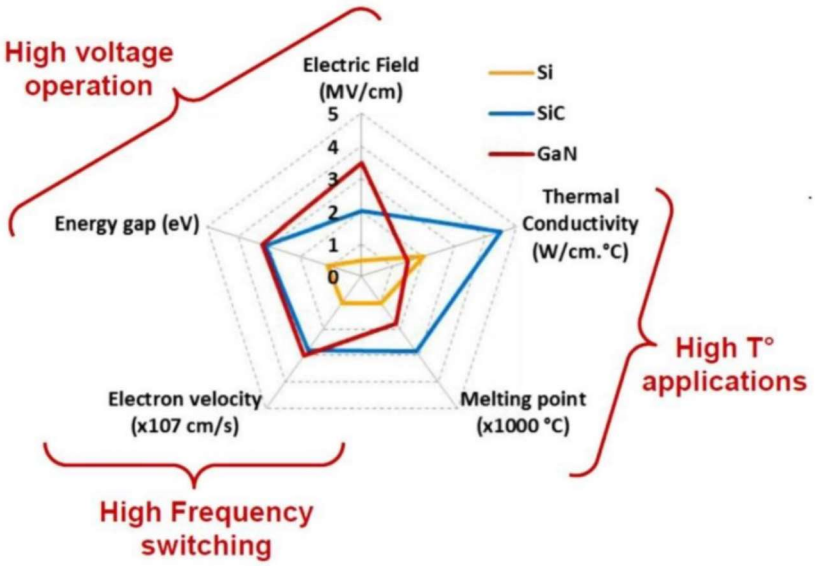

Fig. 1-5 Radar chart of Si, SiC, and GaN devices [26]

The cost trends for 1.2 kV, 3.3 kV, and 10 kV SiC MOSFET are provided in Fig. 1-6, 1-7, and 1-8 respectively. The cost drops rapidly since 2011. The price of SiC device is still higher than Si device but the superior performance of justifies the expensive price especially in high-performance applications such as Tesla Model 3.

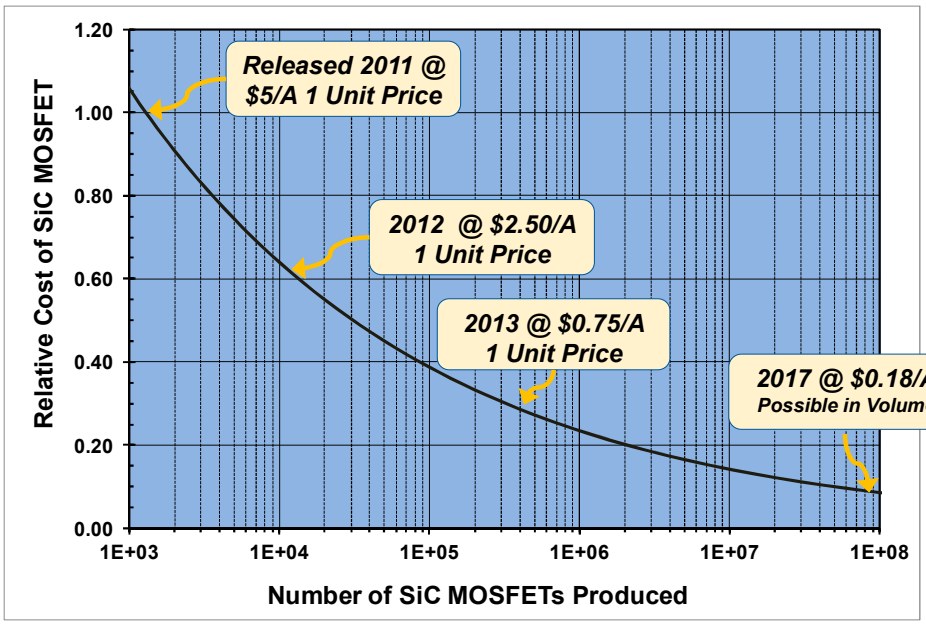

Fig. 1-6 1.2 kV SiC MOSFET projected cost trend [27]

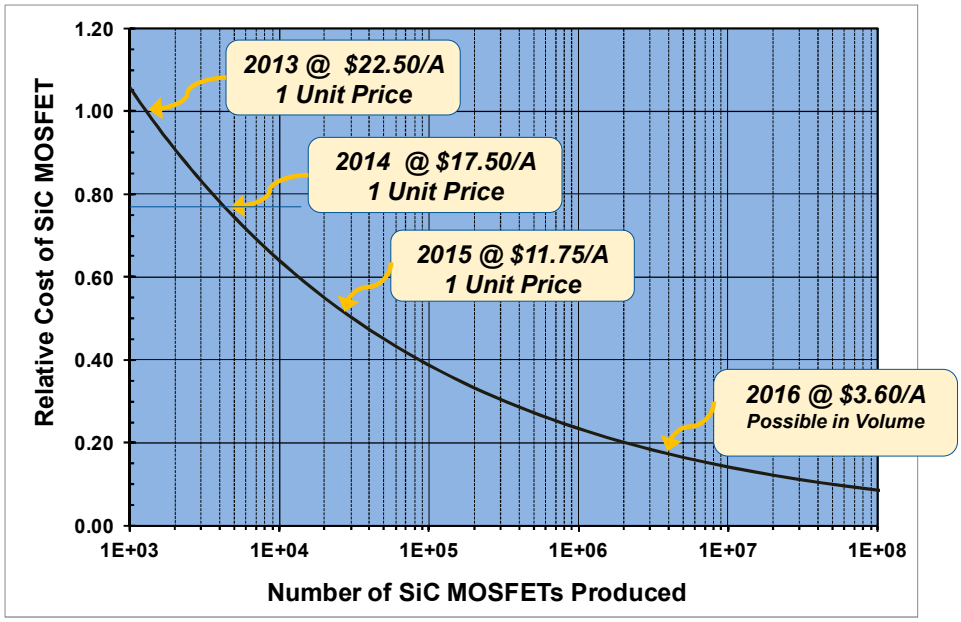

Fig. 1-7 3.3 kV SiC MOSFET projected cost trend [27]

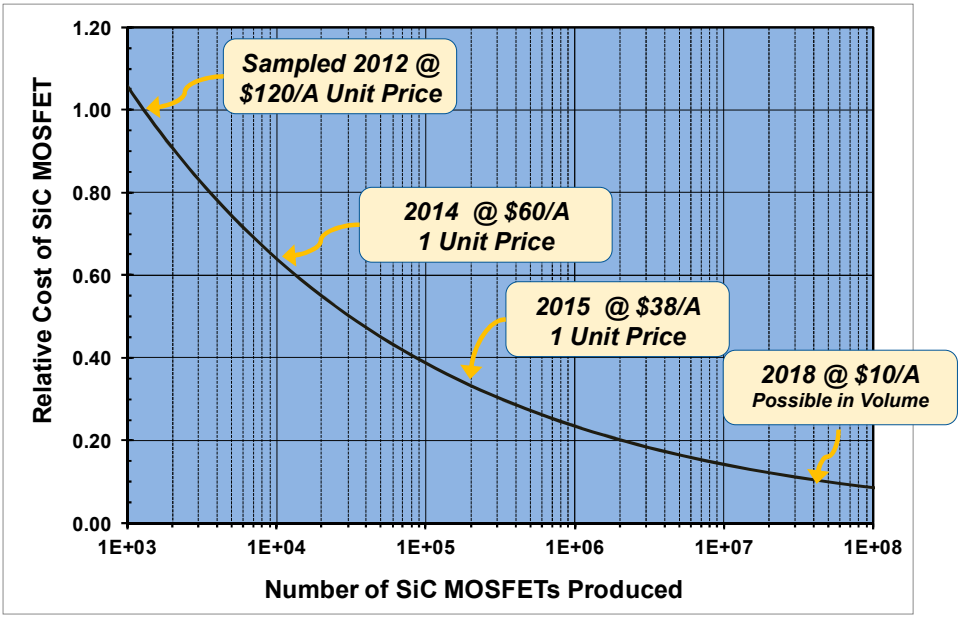

Fig. 1-8 Fig. 1-9 10 kV SiC MOSFET projected cost trend [27]

Given that the typical voltage rating for the shipboard power system is 440 V or 690 V, 1.2 kV SiC device is a promising and practical option, considering that 1.2 kV SiC devices are easily available on the market. As the active front-end selectively feeds the harmonic components, the required current rating is only a fraction of the fundamental component in ac mains and therefore the device current rating is not critical.

In the proposed active front-end, the number of a required dc-link capacitor is reduced by half by introducing a back to back configuration and the voltage ripple is reduced by adjusting the phase angle difference of genset to cancel out the most significant voltage harmonics in the shared dc-link bus. This will eventually reduce the size of the capacitor and extend the lifespan as well.

1.4 Outline of the dissertation

The dissertation consists of 5 chapters and the outline is as follows:

Chapter 1 provides an introduction and background of the multi-genset shipboard power system and the necessity of front-end. It covers the objective and scope of the dissertation as well.

Chapter 2 shows a detailed analysis of the shunt phase-shift transformer rectifier including the harmonic cancellation principle, working condition, and the impact of the non-ideal phase shift angle between the generators. The analysis includes single-phase equivalent circuit analysis, phasor diagram analysis and verification from simulation and experimental test set up.

Chapter 3, a hybrid front-end with an additional shunt APF is discussed. It includes the derivation of 11^{th} and 13^{th} harmonic cancellation mechanism, control loop design, and verifications from simulation and experimental test set up.

Chapter 4, back to back type APF is proposed and the performance of the proposed front-end is verified with the prototype hardware. The impact of phase angle difference on the shared dc-link bus voltage is investigated and the optimal phase angle difference is derived from analytical analysis. The control loop design, simulation, and experimental results are followed.

Chapter 5 provides a conclusion of this dissertation

Chapter 2

Analysis of Shunt Phase-Shift Transformer Rectifier

Since 2004, the shunt phase-shift transformer rectifier has been used for more than 70 low/medium voltage vessels. The concept of the shunt type front-end was presented in the early patent [28] but it did not include detailed explanations for how 5^{th} and 7^{th} harmonics are eliminated. In [24], the mathematical analysis of the shunt phase-shift transformer was provided and experimentally validated. However, the analysis is limited to the ideal condition where the two gensets are 30° phase shifted. In practical operating conditions, there is no guarantee that the phase shift angle of two gensets stays at 30°. In the transient state, it may not close to 30° and severely impact the performance of the front-end. Furthermore, the analysis assumed that the leakage inductance of the transformer was negligible compared to the line reactor in ac mains. Therefore, the impact of non-zero leakage impedance was not fully verified.

In this section, the impact of non-ideal phase-shift angle and leakage impedance are validated through an equivalent circuit block diagram, mathematical derivation. To validate the analytic derivation, simulation and experimental test results are provided.

2.1 Equivalent circuit analysis

It is very difficult to analyze the actual shipboard power system due to high complexity. The overall system has to be simplified for easier analysis. Fig.2-1 shows the block diagram of 2 gensets based shipboard power system with the shunt phase-shift transformer. The electric propulsion system is simply modeled as a resistive load with a capacitor and diode bridge rectifier.

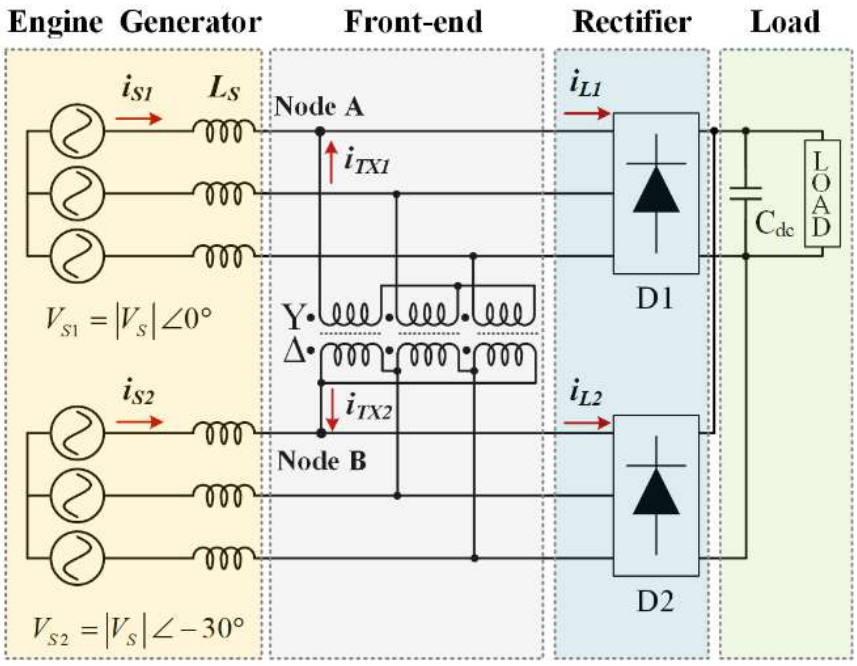

Fig. 2-1 The circuit diagram of shipboard power system with the shunt phase-shift transformer front-end

The voltage of genset1 and genset2 are presented as V_{S1} and V_{S2} respectively. The magnitude of V_{S1} and V_{S2} are the same but V_{S2} lags V_{S2} by 30°. The source impedance is provided as L_S and installed at both genset sides. i_{S1} and i_{S2} are the source currents in genset1 and genset2 individually. i_{TX1} and i_{TX2} are the transformer current in Y-side and Δ-side. For easier derivation, the two transformer currents are defined in the opposite direction. i_{L1} and i_{L2} are Y-side and Δ-side load currents which contain a huge amount of harmonic components. Based on the 3 phase circuit diagram and the initial analytical derivation from [24], a single-phase equivalent circuit can be derived and depicted in Fig. 2-2. A single-line equivalent circuit is presented in Fig. 2-2. The output voltage and a source impedance of genset are V_{S1} and Z_{S1} respectively. The nonlinear load is modeled as an impedance Z_{dc} and a harmonic voltage source V_{Load}, which generates all the $h = 6n \pm 1$ (n = 1, 2, 3, ⋯) harmonics [29].

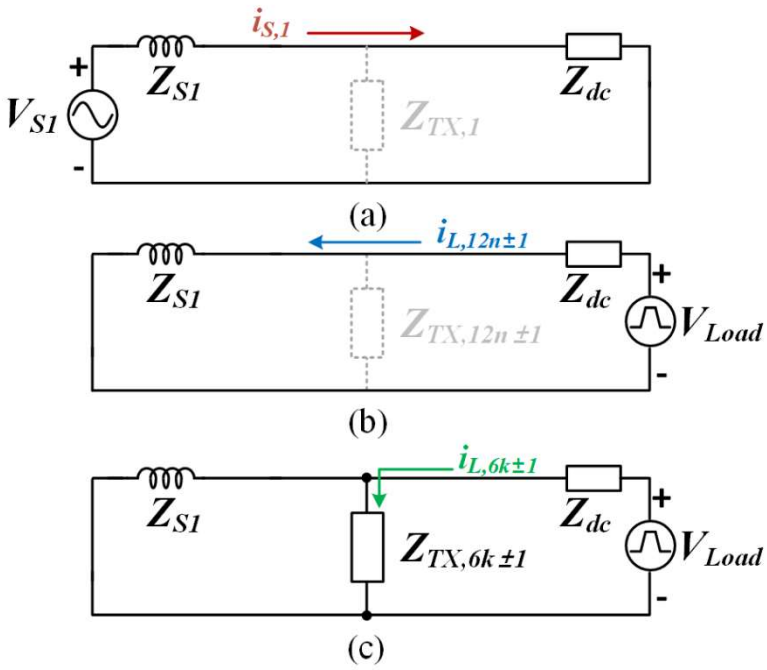

Fig. 2-2 Single-phase equivalent circuit diagram (a) the fundamental current conduction path and (b) $12n \pm 1$ harmonic conduction path (c) $6k \pm 1$ harmonic conduction path

The shunt phase-shift transformer does not provide conduction paths for the fundamental and $12n \pm 1$ (n = 1, 2, 3, ···) components. Therefore, the entire fundamental component is transferred from source to load. In the same way, all the $12n \pm 1$ (n = 1, 2, 3, ···) generated by non-linear load propagate from load to source side. In contrary, $6k \pm 1$ (k = 1, 3, 5, ···) harmonic components originated from non-linear load are trapped in the transformer and do not propagate to the source side. The impact of transformer leakage impedance Z_{TX} is observed in Fig.2-2 (c). As $6k \pm 1$ can flow through either Z_{S1} or $Z_{TX,\ 6k\pm1}$, the amount of harmonic components in source current and transformer current can be calculated from the current division rule. The harmonic voltage source V_{Load} and the network impedance determines the harmonic load current and presented as

$$i_{Load,h} = \frac{v_{Load,h}}{Z_{dc,h} + (Z_{S,h} \,||\, Z_{TX,h})}. \tag{2.1.1}$$

$6k \pm 1$ harmonics in Z_{S1} and $Z_{TX,\ 6k\pm1}$ can be calculated from current division rule

$$i_{S,h} = i_{Load,h} \times \frac{Z_{TX,h}}{Z_{S,h} + Z_{TX,h}} \tag{2.1.2}$$

$$i_{TX,h} = i_{Load,h} \times \frac{Z_{S,h}}{Z_{S,h} + Z_{TX,h}}. \tag{2.1.3}$$

The goal of the shunt phase-shift transformer is mitigated harmonic components in source current and trap as much harmonic component as possible within transformer branch

$$i_{S,h} \simeq 0 \tag{2.1.4}$$

$$i_{TX,h} \simeq i_{Load,h}. \tag{2.1.5}$$

If the leakage impedance is zero, then all the $6k \pm 1$ harmonics flow to the transformer branch and the source does not see these components. However, it is impossible to have a practical transformer with zero leakage impedance, and therefore relatively large source impedance has to be inserted. The illustration assumes that the transformer leakage impedance is zero and the source impedance is a finite value. If the leakage impedance is not negligible, an additional line impedance has to be placed to meet the working condition

$$\frac{Z_{TX,h}}{Z_{S,h}} \ll 1 \tag{2.1.6}$$

The typically rated voltage for shipboard genset is 440 V or 690 V and the rated power output is in the mega-watt scale. The actual leakage impedance can be estimated from the base value and per unit (p.u) value. Referred to 2 MW generator with 690 V line to line voltage, the base value can be calculated as

$$Z_{base,GEN} = \frac{(690\ \text{V})^2}{2\ \text{MW}} = 0.2381\ \Omega \tag{2.1.7}$$

$$\text{L}_{base,GEN} = 631\ \text{uH} \tag{2.1.8}$$

where $Z_{base,GEN}$ and $L_{base,GEN}$ are base impedance and inductance respectively. Assuming that the source impedance of the generator is 0.1 per unit (p.u), the actual source inductance L_s is provided as

$$L_S = L_{base,GEN} \times 0.1 = 63.158 \text{ uH} \tag{2.1.9}$$

In the same way, the transformer leakage inductance L_{leak} can be calculated from the transformer impedance base value $Z_{base,TX}$ and p.u. For 4 MW system with 2 sets of 2 MW gensets, the required transformer rating is at least 1.0 MVA. Considering 10 % margin, the calculation is based on 1.1 MVA transformer.

$$Z_{base,TX} = \frac{(690 \text{ V})^2}{1.1\text{MW}} = 0.4328 \ \Omega \tag{2.1.10}$$

Assuming that the winding resistance of the transformer is negligible, the leakage inductance L_{leak} is derived from $Z_{base,TX}$. The typical per unit value for leakage transformer is 0.03

$$X_{leak} \approx Z_{leak} = Z_{base,TX} \times 0.03 = 0.012984 \ \Omega \tag{2.1.11}$$

$$L_{leak} = \frac{Z_{leak}}{2\pi f} = 34.44 \text{ uH} \tag{2.1.12}$$

By converting the actual leakage inductance to per unit value with $Z_{base,Gen}$, the leakage inductance of the transformer is 0.054 p.u.

$$L_{leak} = L_{base,Gen} \times 0.054 = 0.054 \text{ p.u} \tag{2.1.13}$$

The magnetizing inductance can also be calculated in the same way. The typical p.u is ranged from 100 to 1000 p.u, and 200 is selected for the calculation

$$X_{mag} \approx Z_{mag} = Z_{base,TX} \times 200 = 86.56\Omega \tag{2.1.14}$$

$$L_{mag} = \frac{Z_{mag}}{2\pi f} = 227 \text{ mH} \tag{2.1.15}$$

Again, the magnetizing inductance can be represented with the generator base value $Z_{base,gen}$

$$L_{mag} = L_{base,GEN} \times 363 = 363 \text{ p.u} \tag{2.1.16}$$

Given L_S and L_{leak}, the inductance (impedance) ratio is only 0.54. In other words, the shunt phase-shift transformer traps only 65% of 5th and 7th harmonic current and the remaining 35% of these components propagate to the source and lower the power quality. Therefore, additional source inductance has to be inserted in the source side.

The simulation was performed to see the impact of source inductance on THD at different load conditions. The source, transformer, and load currents waveforms at 25%, 50%, and 100% load are provided in Fig. 2-3, Fig. 2-4, and Fig. 2-5 respectively. The waveforms show that without the insertion of additional inductance ($L_S = 0.1L_{Base}$), TDD (THD at 100% load) of the source current is above 17% and it can not meet the harmonic regulation.

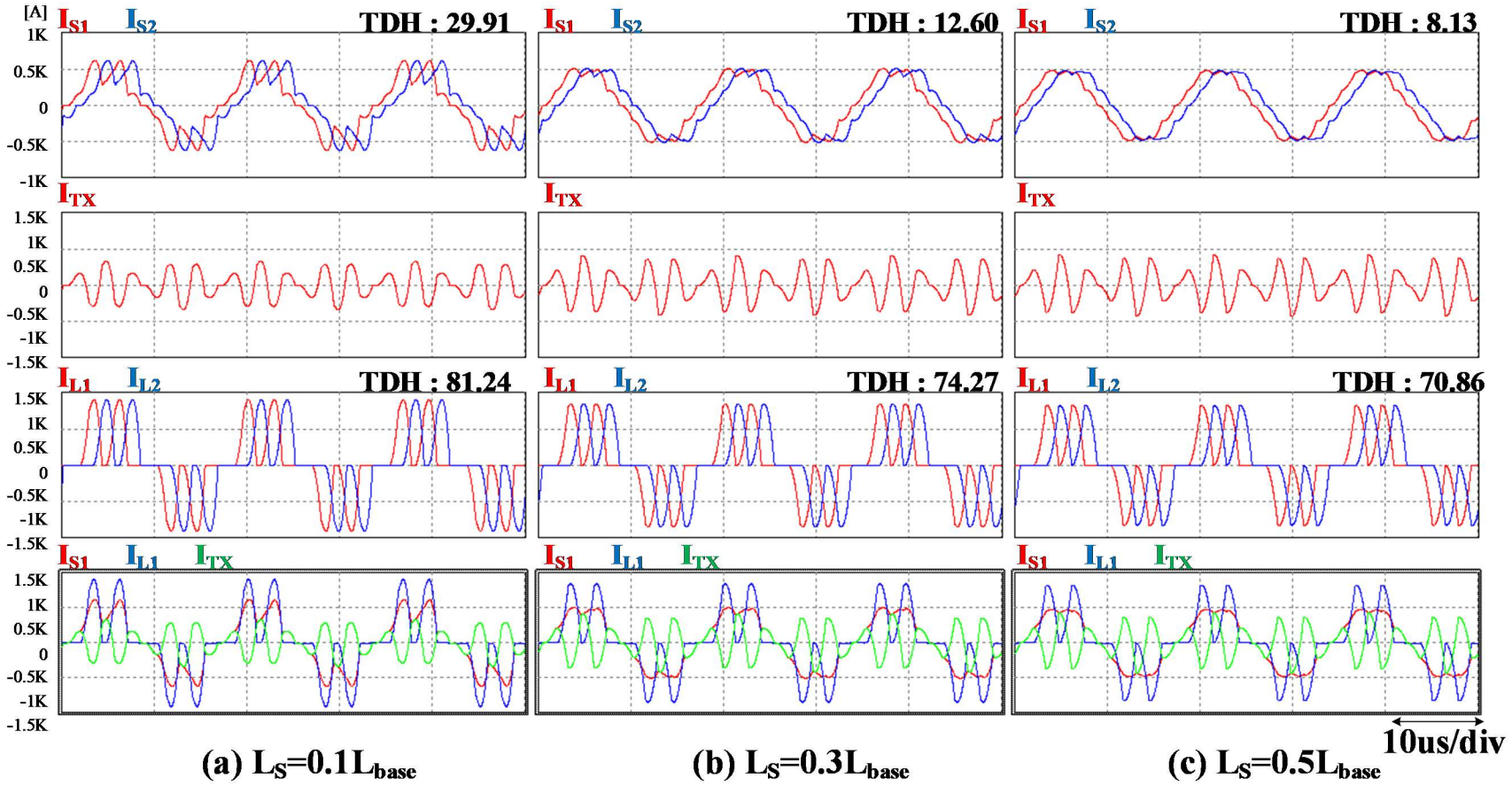

Fig. 2-3. Waveforms of the shunt phase-shift transformer rectifier at 25% load (a)L_s=0.1L_{base} (b)L_s=0.1L_{base} (c)L_s=0.1L_{base}

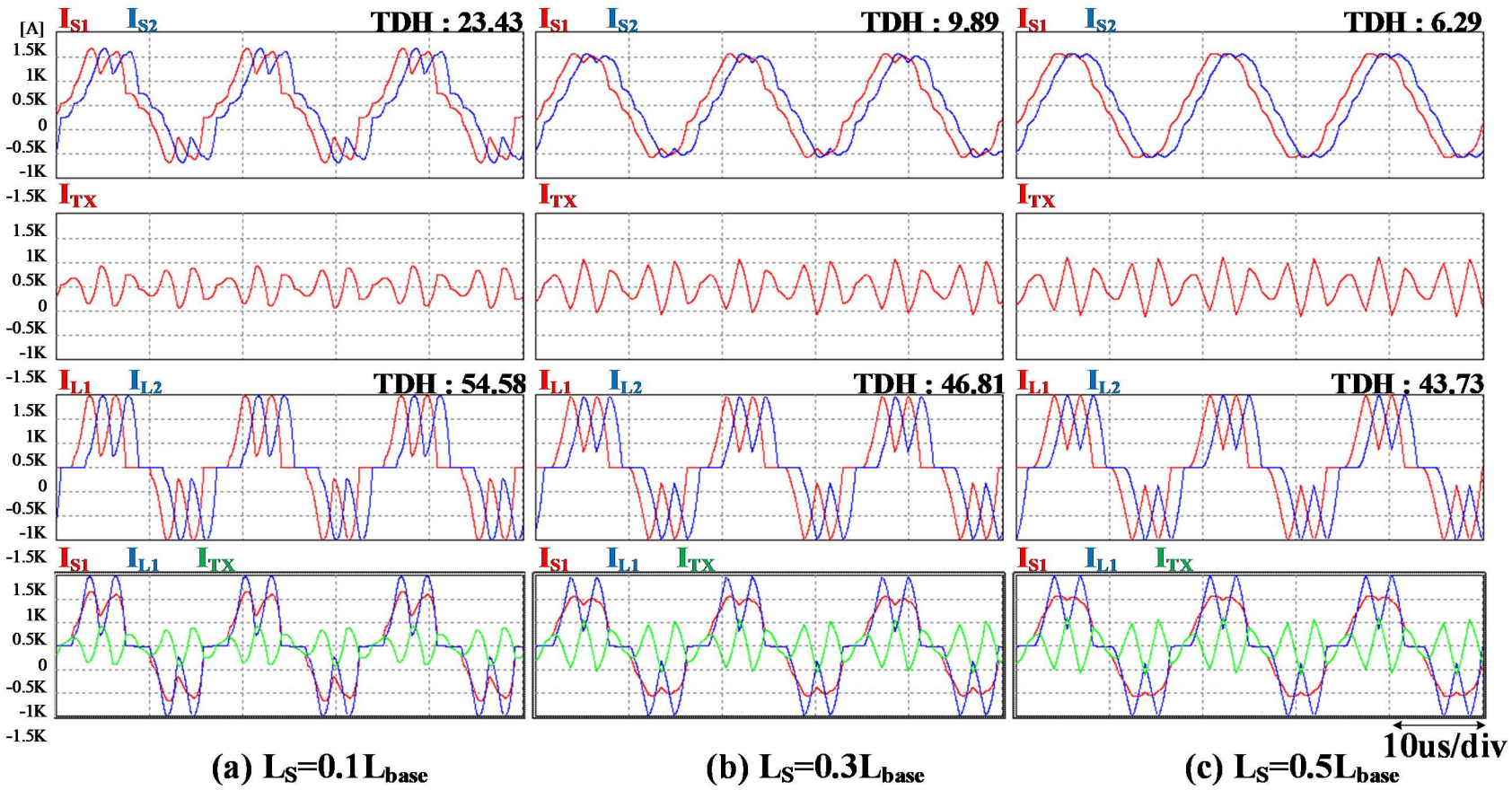

Fig. 2-4. Waveforms of shunt phase-shift transformer rectifier at 50% load (a)L_s=0.1L_{base} (b)L_s=0.1L_{base} (c)L_s=0.1L_{base}

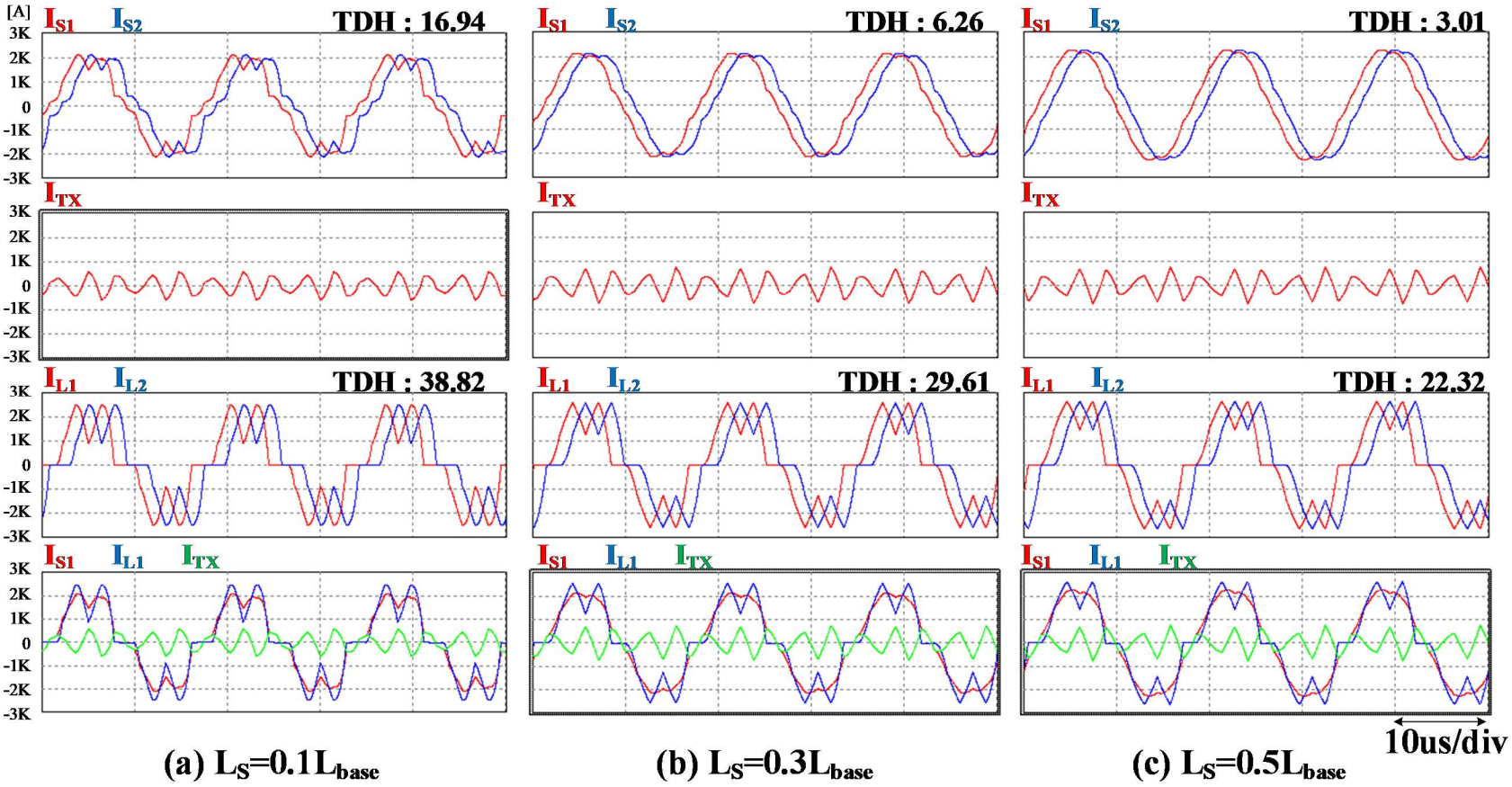

Fig. 2-5. Waveforms of shunt phase-shift transformer rectifier at 10% load (a)L_s=0.1L_{base} (b)L_s=0.1L_{base} (c)L_s=0.1L_{base}

The simulation results are recapped in Fig. 2-6.

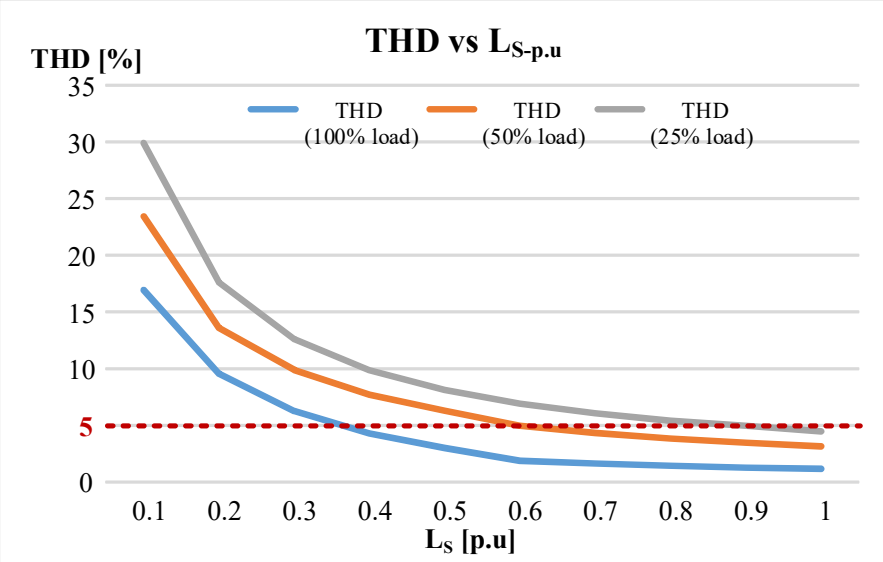

Fig. 2-6. THD with respect to L_S (p.u)

The shipboard power system requires below 5% THD at maximum load (TDD). If the source inductance becomes 0.4 p.u, THD at maximum load becomes 4.31 % and it becomes acceptable for a practical system. Considering that the typical source impedance of the generator is 0.1 p.u, additional bulky line reactor is required to meet below 5% TDD requirement

2.2 Mathematical analysis of shunt type phase-shift transformer rectification system

2.2.1 Load current derivation

The load currents i_{L1} and i_{L2} can be presented as the summation of the fundamental component from source current and harmonic components from the non-linear voltage source. The analytical expressions are

$$i_{L1} = I_{L1,1}\sin(\omega t + \theta_{L1}) + \sum_{h=6n\pm1} I_{L1,h}\sin(h(\omega t + \theta_{L1})) \tag{2.2.1}$$

$$i_{L2} = I_{L2,1}\sin(\omega t + \theta_{L2}) + \sum_{h=6n\pm1} I_{L2,h}\sin(h(\omega t + \theta_{L2})). \tag{2.2.2}$$

The magnitude and phase angle of the fundamental component in the Y-side (Δ-side) load current is $I_{L1,1}$ ($I_{L2,1}$)and θ_{L1} (θ_{L2}). In the same way, the magnitude and phase angle of the harmonic components Y-side (Δ-side) load currents are $I_{L1,h}$ ($I_{L2,h}$) and $\theta_{L1,h}$ ($\theta_{L2,h}$) respectively.

As the two load currents share the same non-linear load, the magnitude of fundamental and harmonic components have to be identical

$$I_{L1,1} = I_{L2,1} \tag{2.2.3}$$

$$I_{L1,h} = I_{L2,h}. \tag{2.2.4}$$

The shunt transformer keeps 30° phase angle difference between i_{L1} and i_{L2}

$$\theta_{L2} = \theta_{L1} - 30° \tag{2.2.5}$$

By substituting (2.1.9), (2.1.10), and (2.1.11) to (2.1.8), i_{L2} can be expressed as Y-side variables

$$i_{L2} = I_{L1,1}\sin(\omega t + (\theta_{L1} - 30°)) + \sum_{h=6k\pm1} I_{L1,h}\sin(h(\omega t + (\theta_{L1} - 30°))). \tag{2.2.6}$$

The analytical derivation shows that the magnitude of Y-side and Δ-side load currents are the same all the components in Δ-side lags Y-side components by $h \times 30°$.

2.2.2 Mathematical derivation of the source current

In the previous section, the relationship between Y-side and Δ-side load currents and transformer currents were derived. This is because the phase angle difference between load and transformer currents is solely determined by the shunt phase-shift transformer. However, this is not the case for the source currents. The expressions for source currents are provided as

$$i_{S1} = I_{S1,1}\sin(\omega t + \theta_{S1}) + \sum_{h=6n\pm1} I_{S1,h}\sin(h(\omega t + \theta_{S1})) \tag{2.2.7}$$

$$i_{S2} = I_{S2,1}\sin(\omega t + \theta_{S2}) + \sum_{h=6n\pm1} I_{S2,h}\sin(h(\omega t + \theta_{S2})). \tag{2.2.8}$$

2.2.3 Transformer current derivation

The derivation of the transformer currents is similar to the load current derivation. i_{TX1} and i_{TX2} shown in Fig.2-1 have the same magnitude and the directions are defined as going into node A and node B respectively.

$$i_{TX1} = I_{TX,1}\sin(\omega t + \theta_{TX1}) + \sum_{h=6k\pm1} I_{TX1,h}\sin(h(\omega t + \theta_{TX1})) \tag{2.2.9}$$

$$i_{TX2} = I_{TX,2}\sin(\omega t + \theta_{TX2}) + \sum_{h=6k\pm1} I_{TX2,h}\sin(h(\omega t + \theta_{TX2})). \tag{2.2.10}$$

The magnitude and phase angle of the fundamental component in Y-side (Δ-side) transformer currents is $I_{TX1,1}$ ($I_{TX2,1}$)and θ_{L1} (θ_{L2}). Given that the shunt transformer is configured as Y-Δ connection with 1:√3, the magnitude of I_{TX2} referred to the Y-side will not be changed. However, additional phase shift θ_{Ph_Shift} will be applied depending on the sequence of the harmonic components. For example, +30° will be added for positive sequence components and −30° will be applied for negative sequence components.

$$i_{TX2,Y} = I_{TX,2}\sin(\omega t + \theta_{TX2} + \theta_{Ph\_Shift}) + \sum_{h=6k\pm1} I_{TX2,h}\sin(h(\omega t + \theta_{TX2}) + \theta_{Ph\_Shift}). \tag{2.2.11}$$

$i_{TX2,Y}$ is coming out of node A and it cancels out i_{TX1}

$$\begin{aligned} i_{TX1} + i_{TX2,Y} &= 0 \\ i_{TX2,Y} &= -i_{TX1}. \end{aligned} \tag{2.2.12}$$

In other words, the magnitude of $i_{TX2,Y}$ is equal to i_{TX1} in the opposite direction

$$\begin{aligned} I_{TX1,1} &= -I_{TX2,1} \\ I_{TX1,h} &= -I_{TX2,h}. \end{aligned} \tag{2.2.13}$$

As the polarity of $i_{TX2,Y}$ is already been considered in the negative sign (−), the two currents have the same phase angle

$$\begin{aligned} \theta_{TX1} &= \theta_{TX2} + 30° \\ h \times \theta_{TX1} &= h \times \theta_{TX2} + \theta_{Ph\_Shift}. \end{aligned} \tag{2.2.14}$$

The final equation for $i_{TX2,Y}$ is provided as

$$i_{TX2,Y} = -I_{TX,1}\sin(\omega t + \theta_{TX1}) - \sum_{h=6k\pm1} I_{TX1,h}\sin(h(\omega t + \theta_{TX1}) + \theta_{Ph\_shift}). \tag{2.2.15}$$

Although the basic equations representing currents in the transformer branch are derived in (2.2.9) and (2.2.10), the equations can not show the relationship between transformer current, source current, and load current. This missing part can be derived by Kirchhoff's Current Law (KCL) at node A and node B. At node A, the summation of source current and transformer current have to be the same as the load current.

$$i_{S1} + i_{TX1} = i_{L1} \tag{2.2.16}$$

In the same way, at node B, the summation of source and transformer current is equal to the load current

$$i_{S2} + i_{TX2} = i_{L2}. \tag{2.2.17}$$

If Δ-side node equation is referred to Y-side, the node equation is

$$i_{S2,Y} - i_{TX1} = i_{L2,Y}. \tag{2.2.18}$$

The differential of (2.2.16) and (2.2.18) gives i_{TX1} as a function of source and load currents

$$\begin{aligned} i_{TX1} &= \frac{1}{2}\left\{(i_{L1} - i_{L2,Y}) - (i_{S1} - i_{S2,Y})\right\} \\ &= i_{TX1\_Load} - i_{TX1\_Source} \end{aligned} \tag{2.2.19}$$

Where i_{TX1_Load} is the half of differential load current in Y side and i_{TX1_Source} is the half of differential source current in Y side. In the same way, i_{TX2} is derived as

$$\begin{aligned} i_{TX2} &= \frac{1}{2}\left\{\left(i_{L2} - i_{L1,\Delta}\right) - \left(i_{S2} - i_{S1,\Delta}\right)\right\} \\ &= i_{TX2\_Load} - i_{TX2\_Source}. \end{aligned} \tag{2.2.20}$$

(2.2.19) and (2.2.20) show the origin of the transformer current and they are the key to understand the harmonic cancellation principle of the shunt type phase-shift transformer rectifier.

2.3 Quantitative analysis of shunt phase-shift transformer rectifier

An analytic analysis provides key equations to help understand the behavior of the shunt type front-end. In addition to analytical analysis, a quantitative analysis is performed to fully investigate the harmonic cancellation mechanism. As the origin of the transformer current is the differential of source current and load currents, quantitative analysis of these current is essential. It is very difficult to precisely represent all the harmonic components in the non-linear current. A square-wave analysis is an alternative way for the quantitative analysis and it is sufficient for figuring out the harmonic cancellation principle. From the square wave analysis, the load currents are presented as

$$i_{L1} = \frac{2\sqrt{3}}{\pi}\{I_{L1,1}\sin(\omega t + \theta_{L1}) + \sum_{h=6n\pm1} I_{L1,h}\sin(h(\omega t + \theta_{L1}))\} \tag{2.3.1}$$

$$i_{L2} = \frac{2\sqrt{3}}{\pi}\{I_{L2,1}\sin(\omega t + \theta_{L2}) + \sum_{h=6n\pm1} I_{L2,h}\sin(h(\omega t + \theta_{L2}))\}. \tag{2.3.2}$$

The differential of load current term i_{TX1_Load} is the difference between Y-side load current i_{L1} and Δ-side load current referred to Y-side $i_{L2,Y}$. The impact of referring Δ-side current to Y-side was investigated in section 2.2.4 and the same principle applies to the load current. To begin with, list all the component that has to be converted and replace $\theta_{L2,l}$ with $\theta_{L1,l} - 30°$. Then, the phase shift produced by Y-Δ transformer has to be considered. For positive sequence components such as fundamental, 5th and 11th harmonics, +30° is applied. For negative sequence components, such as 7th, 13th harmonics, – 30° is applied. As the magnitudes of both side currents are the same, $I_{L2,h}$ can be replaced by $I_{L1,h}$. Table 2-1 shows how the individual component in i_{L2} changes to $i_{L2,Y}$. Due to the transformer turns ratio (1:$\sqrt{3}$), the magnitude does not change when i_{L2} is referred to Y-side.

$$I_{L1,h} = I_{L2,h} \tag{2.3.3}$$

$$I_{L2,h} = I_{L2,h,Y} \tag{2.3.4}$$

Table 2-2 provides the comparison between i_{L1} and $i_{L2,Y}$ and the load differential current. The differential of fundamental, 11th and 13th components (h= 12n ± 1) becomes zero. However, 5th and 7th components (h= 6k ± 1) exist in the differential current. In other words, the shunt phase shift transformer selectively traps h= 6k ± 1 harmonics eventually improve the power quality in ac mains by eliminating these components and the source currents are presented as

$$i_{TX1\_Load} = \frac{1}{2}(i_{L1} - i_{L2,Y}) = \frac{2\sqrt{3}}{\pi} i_{L1,1} \sum_{h=6k\pm1} \frac{1}{h} \sin(h(\omega t + \theta_{L1})). \tag{2.3.5}$$

$$i_{TX2\_Load} = \frac{1}{2}(i_{L2} - i_{L1,\Delta}) = \frac{2\sqrt{3}}{\pi} i_{L2,1} \sum_{h=6k\pm1} \frac{1}{h} \sin(h(\omega t + \theta_{L2})). \tag{2.3.6}$$

Table 2-1. The phase angle of Δ-side load current i_{L2} and Δ-side load current referred to Y-side $i_{L2,Y}$

Component	The original delta side Current i_{L2}	$\pm 30°$ Phase shift from TX, $I_{L1,1} = I_{L2,1}$, $I_{L1,h} = I_{L2,h}$	Delta side current referred to Wye side $i_{L2,Y}$
1st	$I_{L2,1}\sin(\omega t + (\theta_{L1} - 30°))$	$I_{L1,1}\sin(\omega t + (\theta_{L1} - 30°) + 30°)$	$I_{L1,1}\sin(\omega t + \theta_{L1})$
5th	$I_{L2,5}\sin(5(\omega t + (\theta_{L1} - 30)°))$	$I_{L1,5}\sin(5(\omega t + (\theta_{L1} - 30)°) - 30°)$	$I_{L1,5}\sin(5(\omega t + \theta_{L1}) - 180°)$
7th	$I_{L2,7}\sin(7(\omega t + (\theta_{L1} - 30)°))$	$I_{L1,7}\sin(7(\omega t + (\theta_{L1} - 30)°) + 30°)$	$I_{L1,7}\sin(7(\omega t + \theta_{L1}) - 180°)$
11th	$I_{L2,11}\sin(11(\omega t + (\theta_{L1} - 30)°))$	$I_{L1,11}\sin(11(\omega t + (\theta_{L1} - 30)°) - 30°)$	$I_{L1,11}\sin(11(\omega t + \theta_{L1}) - 360°)$
13th	$I_{L2,13}\sin(13(\omega t + (\theta_{L1} - 30)°))$	$I_{L1,13}\sin(13(\omega t + (\theta_{L1} - 30)°) + 30°)$	$I_{L1,13}\sin(13(\omega t + \theta_{L1}) - 360°)$
⋮	⋮	⋮	⋮

Table 2-2. The comparison between i_{L1} and $i_{L2,Y}$

Component	The original wye side current i_{L1}	Delta side current referred to wye side $i_{L2,Y}$	$\frac{1}{2}(i_{L1,h} - i_{L2,h,Y})$
1st	$I_{L1,1}\sin(\omega t + \theta_{L1})$	$I_{L1,1}\sin(\omega t + \theta_{L1})$	0
5th	$I_{L1,5}\sin(5(\omega t + \theta_{L1}))$	$I_{L1,5}\sin(5(\omega t + \theta_{L1}) - 180°)$	$I_{L1,5}\sin(5(\omega t + \theta_{L1}))$
7th	$I_{L1,7}\sin(7(\omega t + \theta_{L1}))$	$I_{L1,7}\sin(7(\omega t + \theta_{L1}) - 180°)$	$I_{L1,7}\sin(7(\omega t + \theta_{L1}))$
11th	$I_{L1,11}\sin(11(\omega t + \theta_{L1}))$	$I_{L1,11}\sin(11(\omega t + \theta_{L1}) - 360°)$	0
13th	$I_{L1,13}\sin(13(\omega t + \theta_{L1}))$	$I_{L1,13}\sin(13(\omega t + \theta_{L1}) - 360°)$	0
⋮	⋮	⋮	⋮

Figs. 2-7 shows the phasor diagrams of Y-side load current $i_{L1,h}$, Δ-side load current $i_{L2,h}$, and Δ-side load current referred to Y-side $i_{L2,h,Y}$ under the balanced condition. As shown in Fig. 2-7 (b), and (c), 5th and 7th ($h = 6k \pm 1$) harmonics in $i_{L1,h}$ and $i_{L2,hY}$ are 180° phase-shifted with the same magnitude and these harmonics are trapped in the Δ-Y transformer. In contrary, fundamental, 11th and 13th ($h = 12n \pm 1$) harmonics in $i_{L1,h}$ and $i_{L2,h,Y}$ shown in Figs. 5(a), 5(d) and 5(e) have the same magnitude with 0° phase shift, the differential of these components are zero. Accordingly, these components are not trapped in the shunt Y-Δ transformer.

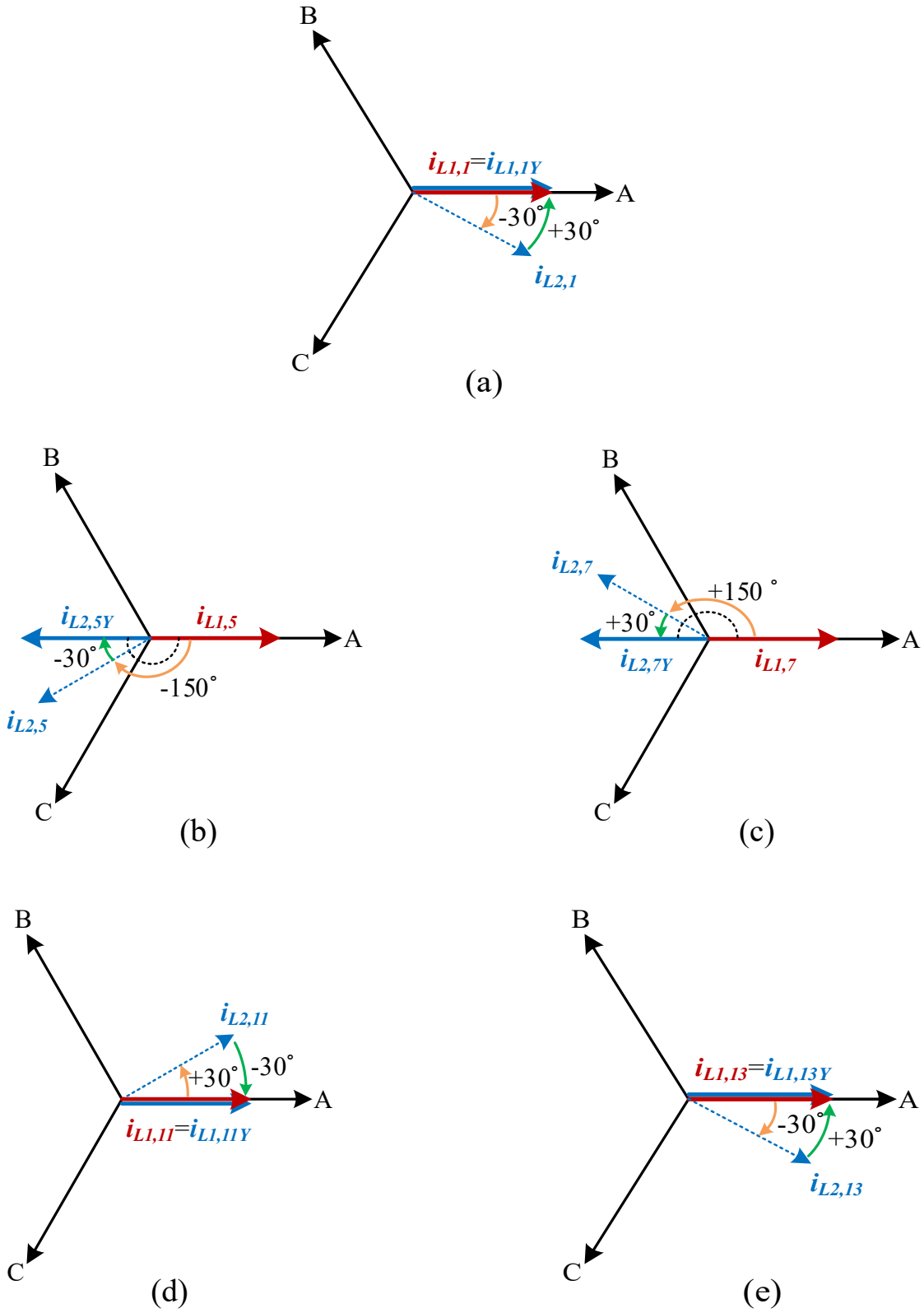

Fig. 2-7. Phasor diagram of $i_{L1,h}$, $i_{L2,h}$, and $i_{L2,h,Y}$ (a) fundamental component, (b) 5th harmonic, (c) 7th harmonic, (d) 11th harmonic, (e) 13th harmonic

The same principle applies to the source current quantitative analysis assuming that $h = 6k \pm 1$ harmonics are completely eliminated by shunt phase-shift transformer. Accordingly, i_{S1} and i_{S2} do not contain $h = 6k \pm 1$ harmonic component and consist of fundamental and $h = 12n \pm 1$ harmonics

$$i_{S1} = I_{S1,1}\sin(\omega t + \theta_{S1}) + \sum_{h=12n\pm1} I_{L1,h}\sin(h(\omega t + \theta_{L1})) \tag{2.3.7}$$

$$i_{S2} = I_{S2,1}\sin(\omega t + \theta_{S2}) + \sum_{h=12n\pm1} I_{L2,h}\sin(h(\omega t + \theta_{L2})). \tag{2.3.8}$$

Again, the differential of source current term is the difference between Y-side source current i_{S1} and Δ-side source current referred to Y-side $i_{S2,Y}$. It should be noted that the phase angle of fundamental components is determined by the phase angle difference of two gensets. Therefore, the phase angle of i_{S1} and i_{S2} are θ_{S1} and θ_{S2} respectively and they are independent of each other. Table 2-3 summarize the conversion and $i_{S2,Y}$ is presented as

$$i_{S2,Y} = \frac{2\sqrt{3}}{\pi}\{I_{S2,1}\sin(\omega t + \theta_{S2} + 30°) + \frac{1}{11}\sin(11(\omega t + \theta_{L1})) + \frac{1}{13}\sin(13(\omega t + \theta_{L1}))\cdots\}. \tag{2.3.9}$$

Table 2-3. The phase angle of Δ-side source current i_{S2} and Δ-side source current referred to Y-side $i_{S2,Y}$

Component	The original delta side Current i_{S2}	±30° Phase shift from TX, $I_{L1,h} = I_{L2,h}$	Delta side current referred to Wye side $i_{L2,Y}$
1st	$I_{S2,1}\sin(\omega t + \theta_{S2})$	$I_{S2,1}\sin(\omega t + \theta_{S2} + 30°)$	$I_{S2,1}\sin(\omega t + \theta_{S1})$
5th	0	0	0
7th	0	0	0
11th	$I_{L2,11}\sin(11(\omega t + \theta_{L2}))$	$I_{L1,11}\sin(11(\omega t + (\theta_{L1} - 30)°) - 30°)$	$I_{L1,11}\sin(11(\omega t + \theta_{L1}) - 360°)$
13th	$I_{L2,13}\sin(13(\omega t + \theta_{L2}))$	$I_{L1,13}\sin(13(\omega t + (\theta_{L1} - 30)°) + 30°)$	$I_{L1,13}\sin(13(\omega t + \theta_{L1}) - 360°)$
⋮	⋮	⋮	⋮

Table 2-4. The comparison between i_{S1} and $i_{S2,Y}$

Component	The original wye side current i_{S1}	Delta side current referred to wye side $i_{S2,Y}$	$\frac{1}{2}(i_{L1,h} - i_{L2,h,Y})$
1st	$I_{S1,1}\sin(\omega t + \theta_{S1})$	$I_{S2,1}\sin(\omega t + \theta_{S2} + 30°)$	$\frac{1}{2}\{I_{S1,1}\sin(\omega t + \theta_{S1}) - I_{S2,1}\sin(\omega t + \theta_{S2} + 30°)\}$
5th	0	0	0
7th	0	0	0
11th	$I_{L1,11}\sin(11(\omega t + \theta_{L1}))$	$I_{L1,11}\sin(11(\omega t + \theta_{L1}) - 360°)$	0
13th	$I_{L1,13}\sin(13(\omega t + \theta_{L1}))$	$I_{L1,13}\sin(13(\omega t + \theta_{L1}) - 360°)$	0
⋮	⋮	⋮	⋮

From Table 2-4, the source differential current i_{TX1_Source} only includes the fundamental component. In other words, i_{TX1_Source} is engaged in the fundamental component exchange and does not impact on the harmonic cancellation performance.

$$i_{TX1\_Source} = \frac{1}{2}\{I_{S1,1}\sin(\omega t + \theta_{S1}) - I_{S2,1}\sin(\omega t + \theta_{S2} + 30°)\} \tag{2.3.10}$$

$$i_{TX2\_Source} = \frac{1}{2}\{I_{S2,1}\sin(\omega t + \theta_{S2}) - I_{S1,1}\sin(\omega t + \theta_{S1} - 30°)\} \tag{2.3.11}$$

Under the ideal condition, where the magnitudes of $i_{S1,1}$ and $i_{S2,1}$ are identical and phase angle difference $\Delta\theta_S$ is 30°, i_{TX1_Source} becomes zero

$$i_{TX1\_Source} = \frac{1}{2}\{I_{S1,1}\sin(\omega t + \theta_{S1}) - I_{S1,1}\sin(\omega t + \theta_{S1} - 30° + 30°)\} = 0. \tag{2.3.12}$$

In practical operating conditions, the phase angle difference between two gensets can deviate from 30° ($\Delta\theta_S \neq -30°$ and $I_{S1,1} \neq I_{S2,1}$). Under these circumstances, i_{TX1_Source} is no longer zero and contains the fundamental component.

From the quantitative analysis, the origin of the transformer differential current was validated and discovered that only the load differential current contributes to the harmonic cancellation and the differential source current is only engaged in the fundamental component exchange when the phase angle of two gensets away from 30°. In section 2.4, the impact of the non-ideal phase shift angle on the behavior of shunt phase-shift front-end will be discussed.

2.4 The impact of non-ideal phase shift angle on the source current

The source current i_{S1} ($i_{S2,Y}$) is equal to the difference between the load current i_{L1} ($i_{L2,Y}$) and transformer current i_{TX1} ($i_{TX2,Y}$)

$$i_{S1} = i_{L1} - i_{TX1} \tag{2.4.1}$$

$$i_{S2,Y} = i_{L1} + i_{TX1} \tag{2.4.2}$$

The fundamental components of i_{S1} ($i_{S2,Y}$), i_{L1} ($i_{L2,Y}$), and ($i_{TX2,Y}$) have to comply with the node equation

$$i_{S1,1} = i_{L1,1} - i_{TX1,1} \tag{2.4.3}$$

$$i_{S2,1,Y} = i_{L1,1} + i_{TX1,1} \tag{2.4.4}$$

When (2.4.3) and (2.44) add up together, the summation of $i_{S1,1}$ and $i_{S2,1,Y}$ is always equal to $2i_{L1,1}$

$$i_{S1,1} + i_{S2,1,Y} = 2i_{L1,1}. \tag{2.4.5}$$

Fig. 2-8 illustrates the phasor diagram of $i_{S1,1}$, $i_{S2,1,Y}$, and , $i_{L1,1}$. If $i_{S1,1}$ and $i_{S2,1,Y}$ are in phase, the magnitude of $i_{S1,1}$ and $i_{S2,1,Y}$ are the same as $0.5i_{S2,1}$ as described in Fig.2-8 (a). In other words, when $i_{S2,1}$ lags $i_{S1,1}$ by 30°, the source currents are balanced. Other than 30° phase-shifted condition, source currents become unbalanced. Fig.2-8 (b), $i_{S1,1}$ leads $i_{S2,1,Y}$ by α° ($i_{S2,1}$ lags $i_{S1,1}$ by (30+α)°) and the magnitude of $i_{S1,1}$ becomes larger than that of $i_{S2,1,Y}$. Fig.2-8 (c) illustrates when $i_{S1,1}$ lags $i_{S2,1,Y}$ by α° ($i_{S2,1}$ lags $i_{S1,1}$ by (30-α)°).

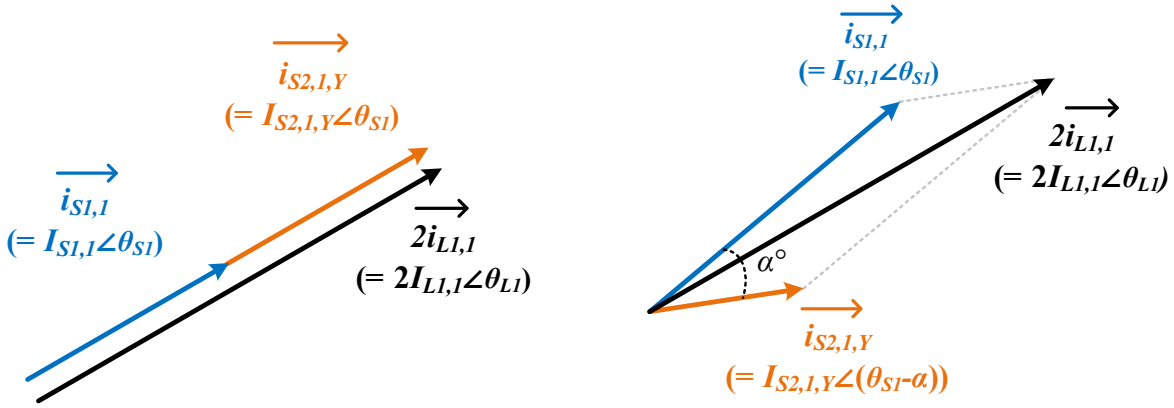

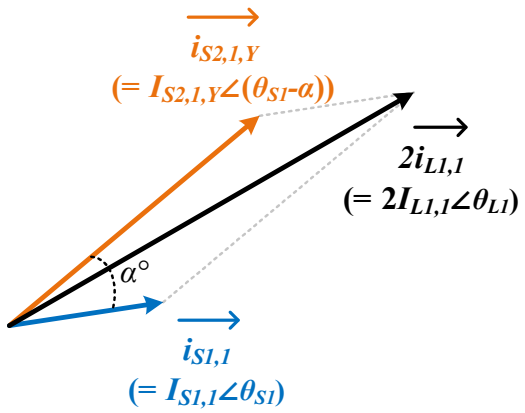

(c)

Fig. 2-8. Fundamental phasor diagram of iS1,1, iS2,1,Y, and iL1,1
(a) $\Delta\theta_S = 30°$, (b) $\Delta\theta_S = -(30+\alpha)°$ ($\alpha < 0$), (c) $\Delta\theta_S = -(30+\alpha)$ ($\alpha > 0$)

The relationship between $i_{S1,1}$, $i_{S2,1,Y}$, and , $i_{L1,1.}$ are found from phasor algebra

$$I_{S1,1}\sin(\theta_{S1}-\theta_{L1})-I_{S2,1,Y}\sin(\theta_{L1}-\theta_{S1}+\alpha)=0 \tag{2.4.6}$$

$$I_{S1,1}\cos(\theta_{S1}-\theta_{L1})+I_{S2,1,Y}\cos(\theta_{L1}-\theta_{S1}+\alpha)=2I_{L1,1}. \tag{2.4.7}$$

In (2.2.38), $i_{S2,1,Y}$ is presented as

$$I_{S2,1,Y}=\frac{I_{S1,1}\sin(\theta_{S1}-\theta_{L1})}{\sin(\theta_{L1}-\theta_{S1}+\alpha)}. \tag{2.4.8}$$

By substituting (2.2.40) to (2.2.39), the analytical expression for $i_{S1,1}$ is established as

$$I_{S1,1}=\frac{2I_{L1,1}}{\cos(\theta_{S1}-\theta_{L1})-\sin(\theta_{S1}-\theta_{L1})\cot(\theta_{S1}-\theta_{L1}-\alpha)}. \tag{2.4.9}$$

Given that the phase angle difference θ_{S1}-θ_{L1} is very small, the magnitude of $i_{S1,1}$ is proportional to the fundamental component of load current and it is a function of phase angle difference $\Delta\theta_S$. $I_{S2,1,}$ can be derived in the same procedure. Fig.2-9 shows the trend of $I_{S1,1}$ and $I_{S2,1,Y}$ with respect to the phase angle difference of gensets (voltage sources). Under the ideal condition where $\Delta\theta_S$ is –30°, the magnitude and phase angle of i_{S1}, $i_{S2,Y}$, and i_{L1} are identical

$$I_{S1,1}=I_{S2,1,Y}=I_{L1,1} \tag{2.4.10}$$

$$\theta_{S1} = \theta_{S2,Y} = \theta_{L1} \tag{2.4.11}$$

The unbalance in source current shows up when $\Delta\theta_S$ deviates from –30°. The magnitude of $i_{S1,1}$ becomes larger than $i_{S2,1,Y}$ when $\Delta\theta_S < -30°$. On the contrary, when $\Delta\theta_S > -30°$, The magnitude of $i_{S2,1}$ is larger than $i_{S1,1}$. It can be concluded that the non-ideal phase shift angle results in source current unbalance and it gets severe as $\Delta\theta_S$ deviates more from –30°.

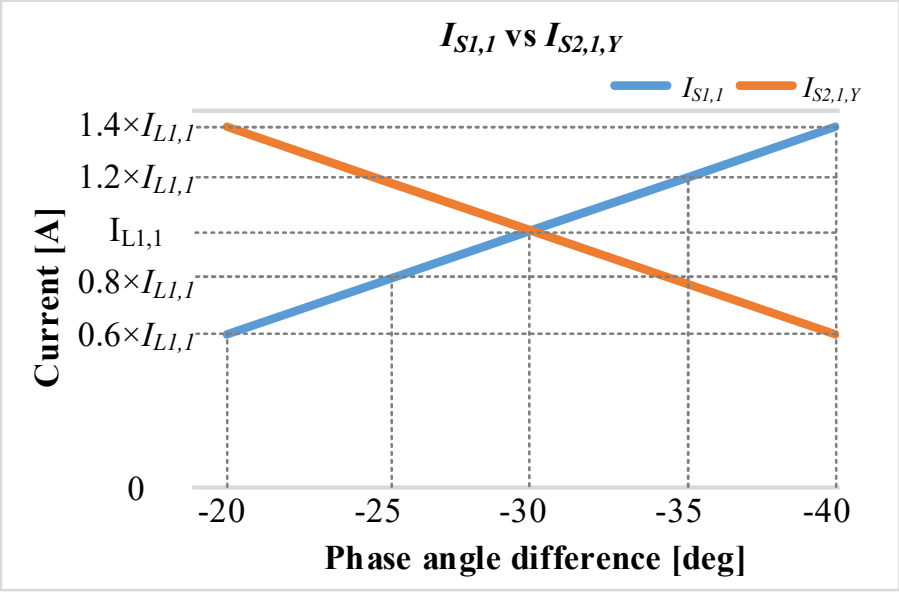

Fig. 2-9 The amplitude of source currents in different phase-shift angles

2.5 Simulation and experimental validation

Simulation and experimental tests were performed to validate the analytical analysis. The simulation setup is provided in Table 2-5.

Table 2-5. Simulation condition

Symbol	Parameters	Value
V_{S1}	Genset1 output voltage	440 V
V_{S2}	Genset1 output voltage	440 V
θ_{S1}	Genset1 phase angle	0°
θ_{S2}	Genset1 phase angle	-(30 + α)°
α	Phase angle deviation	|α| < 10°
R_{load}	Load resistor	20 Ω
C_{dc}	dc-link capacitance	4.4 *m*F
L_{leak}	Transformer leakage inductance	0.15 *m*H
L_S	ac line inductor	6.6 *m*H

The prototype hardware shown in Fig 2-10 was built for the validation purpose. To emulate the shipboard power system, two generators with configurable phase angles are required. However, due to the bulkiness and safety issues, two gensets are replaced by two 3 phase voltage source inverters (VSIs) and the line to line voltage had to be scaled down to 70 V to accommodate lab test environment. Two VSIs have separate ground to eliminate 3rd harmonic circulation and both VSIs are driven by DSP control board (TMS230F28377D). Accordingly, the phase angle of individual VSI can be adjusted in real-time. 3 sets of 1.5kVA, 208V to 120 V single-phase transformer (Square D 9070T 1500D3) were configured in wye and delta connection to implement shunt phase-shift transformer rectifier. Even though the experimental setup is not the same as the simulation condition, the harmonic cancellation principle and all the analytical analyses are still valid. The experimental setup is sufficient for analyzing the behavior of the shunt phase-shift transformer rectifier under the different phase-angle conditions.

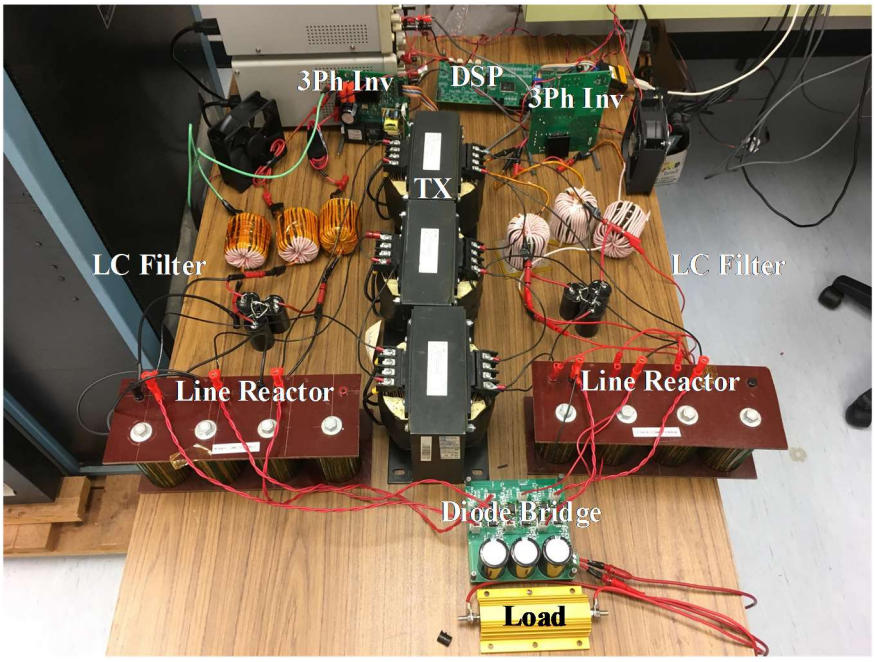

Fig. 2-10. Prototype hardware for Experimental setup

The time-domain waveforms are provided in Fig. 2-11. Among all operating conditions, the load currents i_{L1} and i_{L2} have the same magnitude and i_{L2} lags i_{L1} by 30°, which agrees with the analytical derivation shown in (2.2.3), (2.2.4) and (2.2.5). Fig.2-11 (b) shows the waveforms when the phase angle difference $\Delta\theta_S$ is –30° (ideal operating condition). The magnitude of i_{S1}, i_{S2} are the same and the transformer current i_{TX1} does not contain fundamental component ($i_{TX\_Source} = 0$).

However, the unbalance shows up in different phase angle conditions. When $\Delta\theta_S = -20°$, the magnitude of i_{S2} is larger than that of i_{S1} as shown in Fig.2-11 (a). On the other hand, the magnitude of i_{S1} is larger than that of i_{S2} when $\Delta\theta_S = -40°$ as shown in Fig. 2-11(c). In Figs.2-11 (a) and (c), i_{TX1} includes the fundamental component and the RMS value of i_{TX1} is increased by 7%.

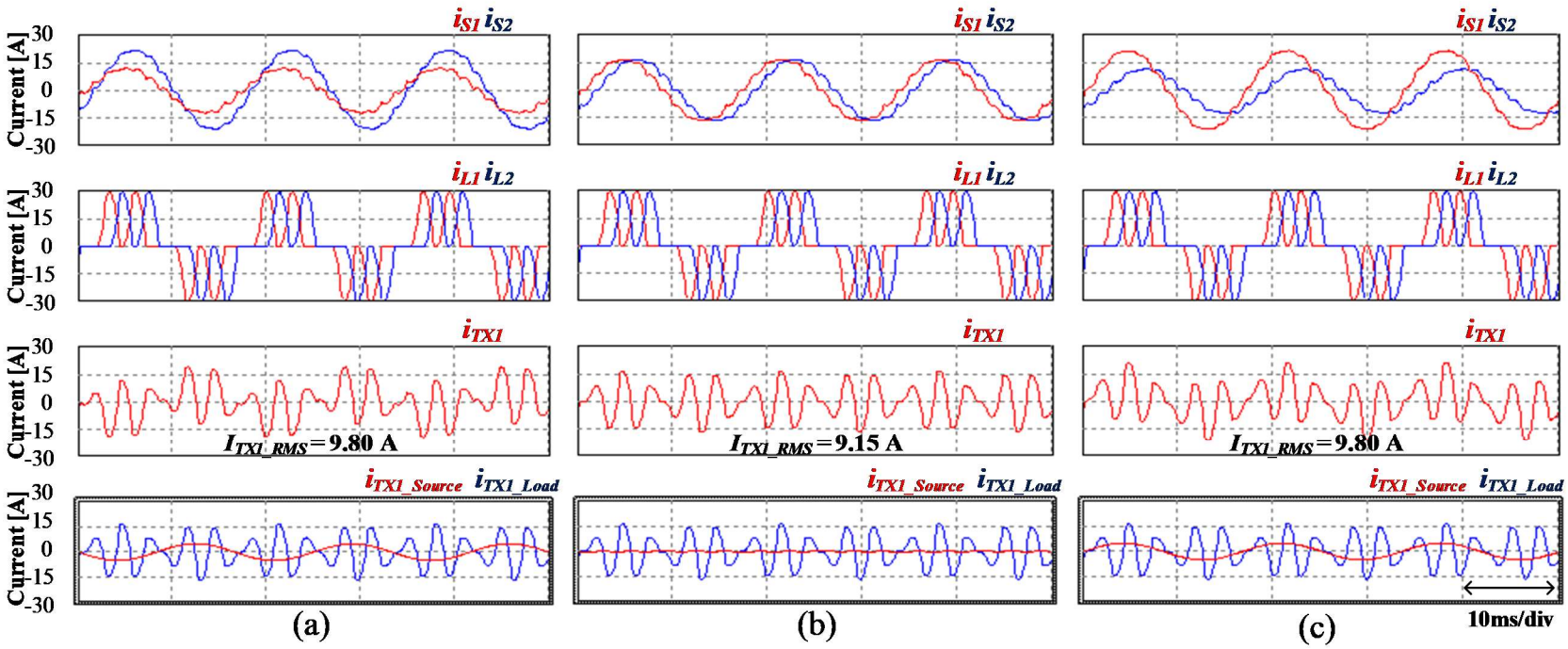

Fig. 2-11 Time domain simulation waveforms of source i_S, load i_L, and transformer current i_{TX} under different phase angle difference (a) $\Delta\theta_S = -20°$($\alpha = +10°$), (b) $\Delta\theta_S = -30°$($\alpha = 0°$), (c) $\Delta\theta_S = -40°$($\alpha = -10°$)

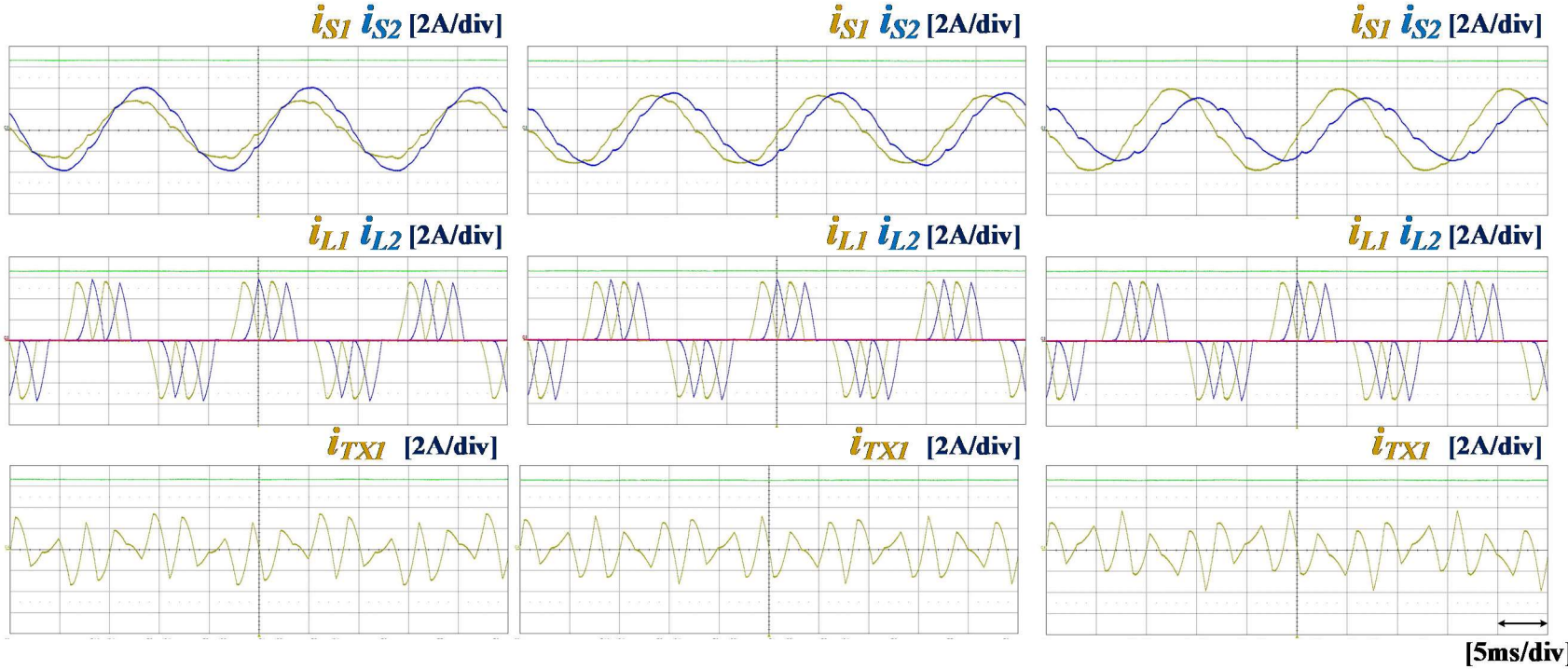

Fig. 2-12 Time domain simulation waveforms of source i_S, load i_L, and transformer current i_{TX} under different phase angle difference (a) $\Delta\theta_S$= –20°(α = +10°), (b) $\Delta\theta_S$= –30°(α = 0°), (c) $\Delta\theta_S$= –40°(α = –10°)

In addition to the time domain waveforms, fundamental and harmonic components of interests are extracted from frequency spectra and plotted. As shown in Fig.2-13, the fundamental component in i_{S1} and i_{S2} are dependent on the phase angle difference and the results agree with the analytical analysis. As a result of source currents unbalance, the transformer current includes fundamental component under the non-ideal phase shift conditions. However, the load current i_{L1} and i_{L2} are not dependent on the phase angle difference. The trend also verifies that the phase angle difference impacts the magnitude of the source current and it leads to an increase in the magnitude of the transformer current.

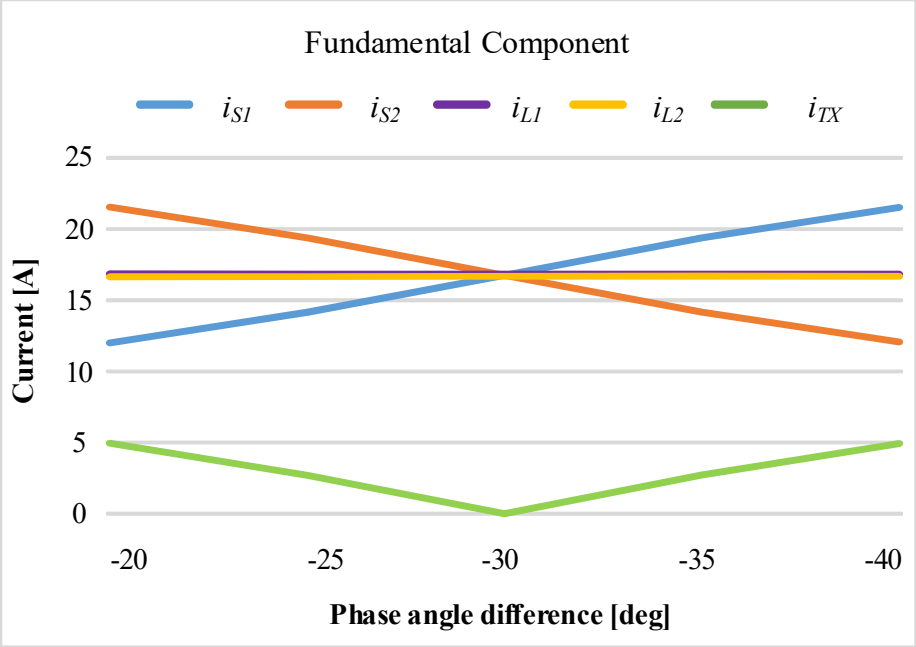

Fig. 2-13. The magnitude of the fundamental component in the source, load, and transformer current

The magnitude of 5th and 7th harmonic components are plotted in Fig. 2-14 and Fig. 2-15 respectively. The amount of harmonic components in the transformer current determines the harmonic cancellation performance of the front-end. The more harmonics in the transformer. the cleaner source current. Regardless of the phase angle difference, i_{TX} contains the same amount of

5th and 7th harmonic components. This implies that the harmonic cancellation performance is not affected by the phase angle difference. As a consequence, the amount of harmonic contents in source currents are identical in all conditions. The simulation results match with (2.2.25) and (2.2.26By comparing the source and transformer currents, more than 97% of harmonic contents are trapped by the transformer branch.

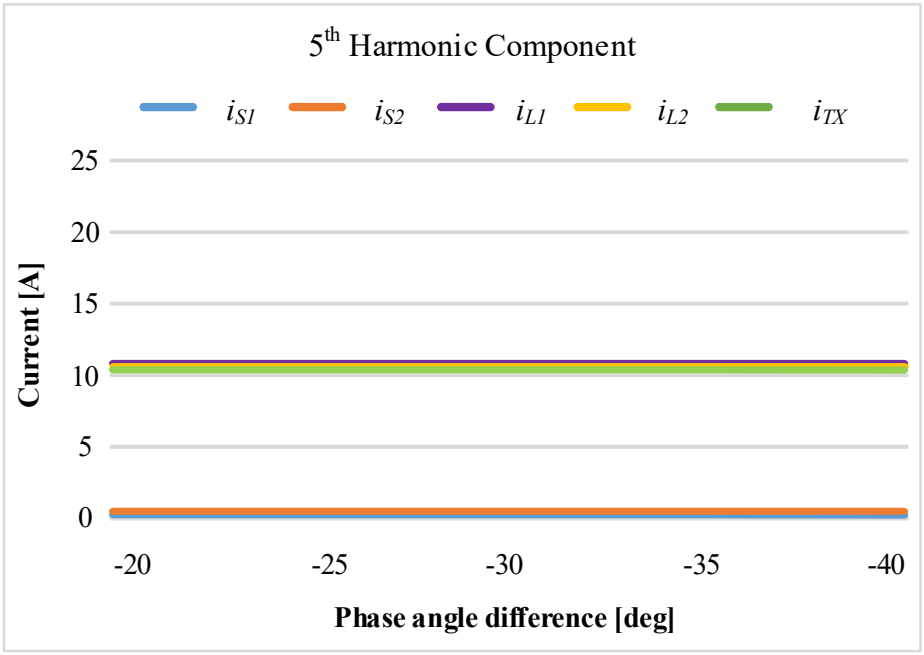

Fig. 2-14. The magnitude of 5th harmonic component in the source, load, and transformer current

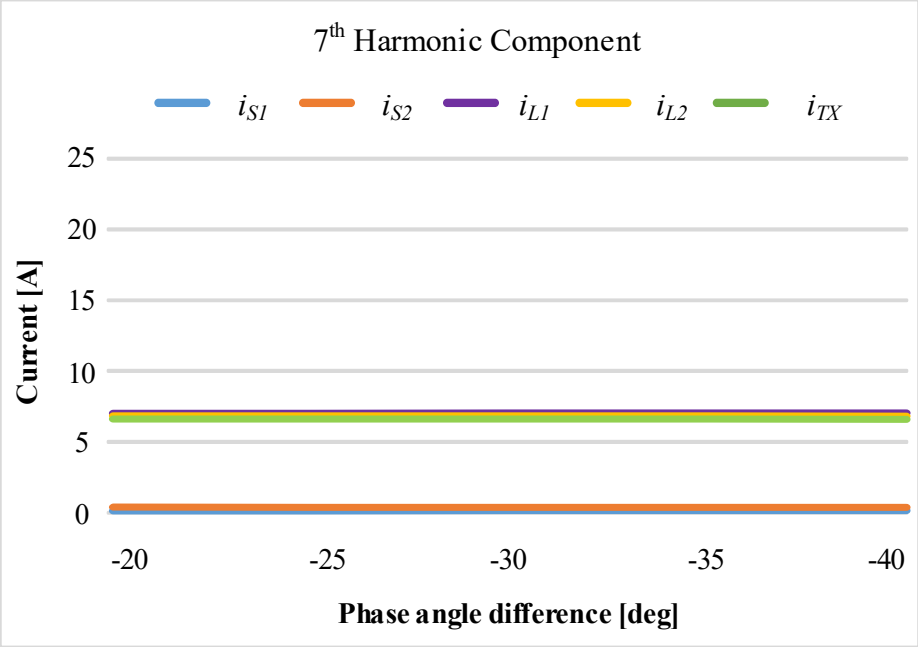

Fig. 2-15. The magnitude of 7th harmonic component in the source, load, and transformer current

2.6 Summary

In this chapter, the operation of the shunt phase-shift transformer rectifier was mathematically analyzed. The non-ideal phase shift angle induces an unbalanced phase current and the transformer RMS current. Interestingly, the harmonic cancellation performance was not affected by the phase angle difference but it is determined by impedance ratio between source and transformer leakage Z_{TX}/Z_S. The analysis of shunt type phase-shift transformer front-end under the non-ideal phase shift condition provides the origin of source current unbalances in practical operating conditions. The phase angle difference of two gensets may have $\pm 10°$ deviation from the ideal operating condition which brings uneven distribution of source currents and increased current stress on one side of genset and passive components.

Chapter 3

Hybrid front-end for multi-generator power system

In Chapter 2, the analytical analysis of the shunt phase-shift transformer was provided and it effectively eliminated 5^{th} and 7^{th} harmonics from the non-linear load. Compared to the traditional 12-pulse rectifier, it showed equivalent performance while more than 75% transformer size reduction. The drawback of shunt type front-end is the necessity of a bulky line reactor in the source side which will significantly increase the weight and volume of the system. Also, the harmonic cancellation mechanism is limited to $h = 6k \pm 1$ ($k = 1, 3, 5, \cdots$) harmonics and therefore 11^{th} and 13^{th} harmonics still remain on ac mains.

In modern shipboard power system design, the harmonic mitigation solution for 11^{th} and 13^{th} harmonics are also recommended in order to keep THD*v* below 5% [30] and 18 pulse rectifier is more preferable to 12 pulse rectifier due to better harmonic cancellation performance. Table 3-1 shows the typical THDv in different front-end topologies.

Table 3-1. Total Harmonic Distortion (THD) Voltage Limit Comparison between Different Drives [30]

Attributes	6-pulse	6-pulse with Filter	12-pulse	18-pulse	Active Front- End
Typical THDv at the drive input terminal	@30-40 %	@5-8 %	@5-12 %	@5-8 %	@3-4 %

In multi-pulse converters, the higher-order harmonics can be eliminated by increasing the transformer pairs but it leads to an increase in the overall system cost and volume. In the same way, the shunt-type phase-shift transformer can eliminate the higher-order harmonics by installing additional shunt phase-shift transformers between the gensets but again, the additional transformer increases the overall cost and volume of the system.

In this chapter, a hybrid shunt front-end is proposed and validated with simulation and experimental results.

The concept of the proposed hybrid front-end is similar to the idea that combines 12-pulse rectifier and 3-phase shunt active power filter (APF) shown in [10]. The proposed front-end consists of a shunt phase-shift transformer, which corresponds to the 12-pulse rectifier and a 3-phase shunt active power filter (APF). The transformer eliminates 5th and 7th harmonics and an additional APF will eliminate the remaining 11th and 13th harmonics. In this approach, the front-end can effectively eliminate harmonics up to 13th harmonics without the additional bulky transformer.

3.1 Theoretical background for the hybrid front-end

The circuit diagram of the hybrid front-end is provided in Fig. 3-1. It is the same as the circuit diagram of the shunt phase-shift transformer except for the additional shunt active power filter (APF). APF can be installed either Y or Δ side.

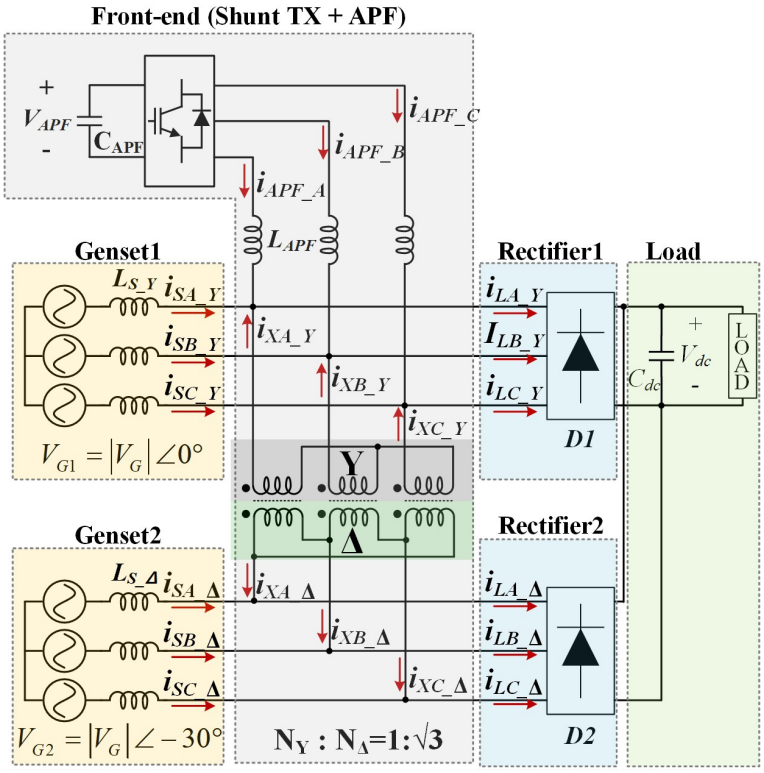

Fig. 3-1. Circuit diagram of 2 geset-based system with hybrid front-end

The load current contains h^{th} ($h = 6n \pm 1$) harmonics originated from the non-linear load. The load current (A-phase) in Y-side is presented as

$$i_{LA\_Y} = i_{LA\_Y,1}\sin(\omega t + \theta) + \sum_{h=6n\pm1} i_{LA\_Y,h}\sin(h(\omega t + \theta)) \tag{3.1.1}$$

where $i_{LA\_Y,1}$ and $i_{LA\_Y,h}$ is the magnitude of fundamental and harmonic current in Y-side. Δ-side current lags i_{LA_Y} by 30° and presented as

$$i_{LA\_\Delta} = i_{LA\_\Delta,1}\sin(\omega t + \theta - 30°) + \sum_{h=6n\pm1} i_{LA\_\Delta,h}\sin(h(\omega t + \theta - 30°)). \tag{3.1.2}$$

+30° phase shift is applied for a positive sequence and -30° phase shift is applied for the negative sequence components. The delta side load current referred to Y-side is

$$i_{LA\_\Delta,Y} = i_{LA\_\Delta,1}\sin(\omega t + \theta) + \sum_{h=6n\pm1} (-1)^n i_{LA\_\Delta,h}\sin(h(\omega t + \theta)). \tag{3.1.3}$$

Referred ti (2.3.9) and (2.3.10), the transformer current i_{XA_Y} is presented as

$$\begin{aligned} i_{XA\_Y} &= \frac{1}{2}(i_{LA\_Y} - i_{LA\_\Delta,Y}) \\ &= \sum_{h=6k\pm1} i_{LA\_Y,h}\sin(h(\omega t + \theta)). \end{aligned} \tag{3.1.4}$$

The source current i_{S_Y} contains fundamental and $12n \pm 1$ ($n = 1, 2, 3, \cdots$) harmonic component

$$i_{SA\_Y} = i_{SA\_Y,1}\sin(\omega t + \theta) + \sum_{h=12n\pm1} i_{SA\_Y,h}\sin(h(\omega t + \theta)) \tag{3.1.5}$$

where $i_{SA\_Y,1}$ and $i_{SA\_Y,h}$ are the amplitude of 60 Hz and harmonic component. Similarly, i_{S_Δ} can be presented as

$$i_{SA\_Y} = i_{SA\_Y,1}\sin(\omega t + \theta) + \sum_{h=12n\pm1} i_{SA\_Y,h}\sin(h(\omega t + \theta)) \tag{3.1.6}$$

The harmonic cancellation principle of the shunt phase-shift transformer shows that it can not eliminate $12n \pm 1$ ($n = 1, 2, 3, \cdots$) harmonics and these components flow to the ac mains and lead to harmonic distortion in ac mains.

Although the most significant harmonic components (5th and 7th) are eliminated by the shunt phase-shift transformer, 11th and 13th components still exist in ac mains and the amount of these components is not negligible. These remaining components are actively canceled by APF. Fig.3-2 describes the single-phase harmonic conduction path for the proposed front-end up to 13th harmonic component.

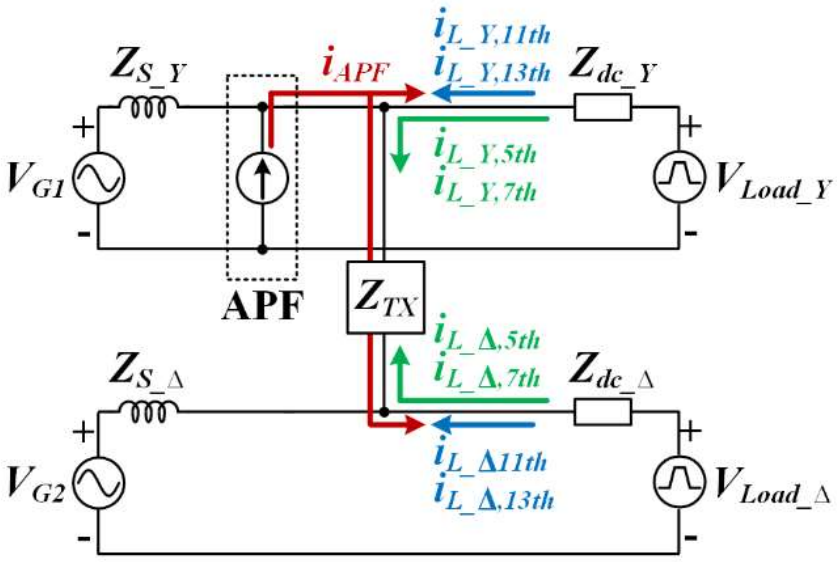

Fig. 3-2 Single-phase equivalent circuit diagram and harmonic conduction path

Due to the nature of the phase-shift transformer, it provides the harmonic conduction path for 17th, 19th and all the higher-order h^{th} ($h = 6k \pm 1$) harmonics but these harmonics are ignored in Fig. 3-2 for the simple representation. The single-phase equivalent circuit diagram and the modeling of non-linear load are the same as Fig. 2-2 except for the ideal current source, which represents the shunt active power filter in Y-side.

The active power filter is controlled to injects 11th and 13th harmonics in Y-side. Referred to (2.3.5), the differential of load current for 11th and 13th harmonics are zero and these harmonics are not flowing to the transformer branch. However, as the 11th and 13th harmonic in Y-side are

gone, then the differential of 11^{th} and 13^{th} harmonics in load currents are not zero and starts to flow to Z_{TX} and actively canceled by APF.

Overall, the shunt phase-shift transformer eliminates 5^{th}, 7^{th}, 17^{th}, 19^{th} and APF eliminates 11^{th} and 13^{th}. In theory, the most significant harmonic component is pushed to 23^{rd}. Table 3-2 shows the characteristics of front-end in different configurations.

Table 3-2. The characteristics of the front-end

Topology	# of TX pair	# of APF	Typical harmonic current component	Cost
6 pulse converter	0	0	5, 7, 11, 13, 17, 19,23,25	Low
Shunt TX front-end	1	0	11, 13, 23, 25	Low
Hybrid shunt front-end	1	1	23,25	Medium
12 pulse converter	2	0	11, 13, 23, 25	Medium
24 pulse converter	4	0	23, 25	High

3.2 Current controller design

The purpose of a shunt APF is to selectively eliminate 11^{th} and 13^{th} harmonics in ac mains. In this chapter, several control techniques will be covered and the most appropriate control technique for selective harmonic cancellation will be selected for the hybrid front-end

3.2.1 *pq* control theory

The instantaneous reactive power theory, also known as p-q theory, was shown in [31] and has been widely used in active power filter applications. Instead of control voltage and current, the control objective of the *pq* theory is active and reactive power flow of the system. The derivation of p-q theory starts from Clarke transformation

$$\begin{bmatrix} v_o \\ v_\alpha \\ v_\beta \end{bmatrix} = \sqrt{\frac{2}{3}} \begin{bmatrix} \frac{1}{\sqrt{2}} & \frac{1}{\sqrt{2}} & \frac{1}{\sqrt{2}} \\ 1 & -\frac{1}{2} & -\frac{1}{2} \\ 0 & \frac{\sqrt{3}}{2} & \frac{\sqrt{3}}{2} \end{bmatrix} \begin{bmatrix} v_a \\ v_b \\ v_c \end{bmatrix} \tag{3.2.1}$$

$$\begin{bmatrix} i_o \\ i_\alpha \\ i_\beta \end{bmatrix} = \sqrt{\frac{2}{3}} \begin{bmatrix} \frac{1}{\sqrt{2}} & \frac{1}{\sqrt{2}} & \frac{1}{\sqrt{2}} \\ 1 & -\frac{1}{2} & -\frac{1}{2} \\ 0 & \frac{\sqrt{3}}{2} & \frac{\sqrt{3}}{2} \end{bmatrix} \begin{bmatrix} i_a \\ i_b \\ i_c \end{bmatrix} \tag{3.2.2}$$

where v_a, v_b, v_c are phase voltage of ABC coordinate system. The result of the transformation is the two-phase reference frame. v_α, v_β and v_0 are phase voltage of *αβ0* coordinate system. i_a, i_b, i_c are the phase currents of *ABC* coordinate system. The result of transformation is two-phase reference frame. i_α, i_β and i_0 are phase current of αβ0 coordinate system. From (3.2.1) and (3.2.2), the instantaneous power is defined as

$$\begin{bmatrix} p \\ q \end{bmatrix} = \begin{bmatrix} v_\alpha & v_\beta \\ v_\beta & -v_\alpha \end{bmatrix} \begin{bmatrix} i_\alpha \\ i_\beta \end{bmatrix}. \tag{3.2.3}$$

p represents the instantaneous real power and q represents the instantaneous imaginary power. Then, the instantaneous active and reactive current are rewritten as a function of v_α, v_β, and p, q [32]

$$\begin{bmatrix} i_\alpha \\ i_\beta \end{bmatrix} = \frac{1}{{v_\alpha}^2 + {v_\beta}^2} \begin{bmatrix} v_\alpha & v_\beta \\ v_\beta & -v_\alpha \end{bmatrix} \begin{bmatrix} p \\ 0 \end{bmatrix} + \frac{1}{{v_\alpha}^2 + {v_\beta}^2} \begin{bmatrix} v_\alpha & v_\beta \\ v_\beta & -v_\alpha \end{bmatrix} \begin{bmatrix} 0 \\ q \end{bmatrix} \tag{3.2.4}$$

The importance of (3.2.4) is that it is a key equation for generating current reference in alpha, beta axis i_α^*, i_β^* in the control loop.

The *p-q* theory can be easily understood with the example. Assuming that the phase current contains harmonic contents while the phase voltages contain fundamental component only

$$\begin{aligned} v_a(t) &= \sqrt{2}V\sin(\omega t) \\ v_b(t) &= \sqrt{2}V\sin(\omega t - 120°) \\ v_c(t) &= \sqrt{2}V\sin(\omega t + 120°) \end{aligned} \tag{3.2.5}$$

$$\begin{aligned} i_a(t) &= \sqrt{2}I_1\sin(\omega t+\phi) - \sqrt{2}I_5\sin(5\omega t+\phi) + \sqrt{2}I_7\sin(7\omega t+\phi)\ldots \\ i_b(t) &= \sqrt{2}I_1\sin(\omega t-120°+\phi) - \sqrt{2}I_5\sin(5\omega t-120°+\phi) + \sqrt{2}I_7\sin(7\omega t-120°+\phi) \\ i_c(t) &= \sqrt{2}I_1\sin(\omega t+120°+\phi) - \sqrt{2}I_5\sin(5\omega t+120°+\phi) + \sqrt{2}I_7\sin(7\omega t+120°+\phi). \end{aligned} \tag{3.2.6}$$

The instantaneous active and reactive power are

$$\begin{aligned} p &= 3VI_1\cos(\phi) + 3\times[VI_5\cos(4\omega t+\phi) + VI_7\cos(6\omega t+\phi)] \\ &= \bar{p} + \tilde{p} \\ q &= 3VI_1\sin(\phi) + 3\times[VI_5\sin(4\omega t+\phi) + VI_7\sin(6\omega t+\phi)] \\ &= \bar{q} + \tilde{q} \end{aligned} \tag{3.2.7}$$

The dc component of p and q are given as $\bar{p}$ and $\bar{q}$. The oscillating instantaneous active and reactive power are defined as $\tilde{p}$ and $\tilde{q}$. If $\tilde{p}$ and $\tilde{q}$ are fully compensated, the system will not contain harmonic components. Also, reactive power compensation can be easily achieved by setting $\bar{q}$ = 0.The control block diagram of instantaneous power control is provided in Fig. 3-3.

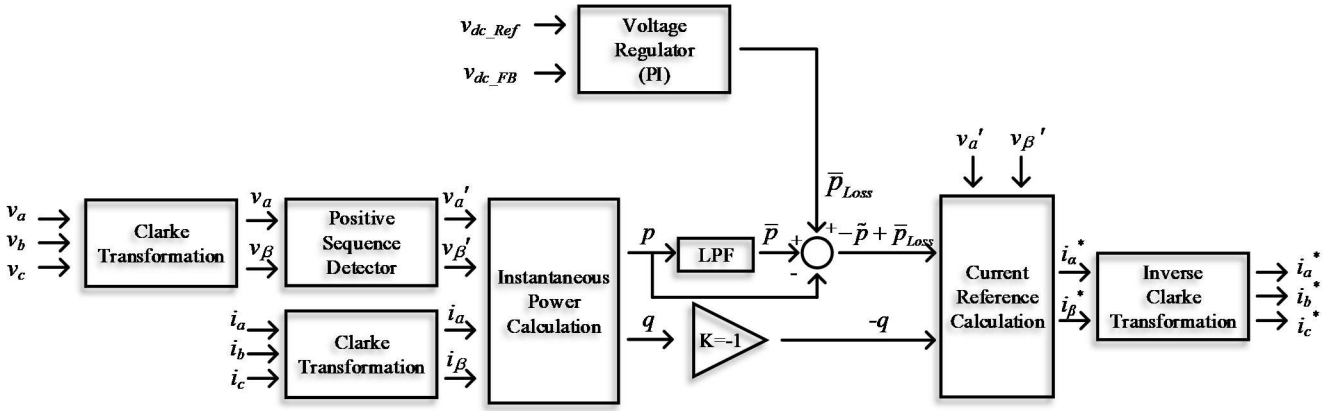

Fig. 3-3. Control block diagram of instantaneous active and reactive power control

The *p-q* theory assumes that 3-phase voltages are balanced and only contain the fundamental component. However, in practical implementation, the non-linear load distorts both current and voltage that the initial assumption is not valid. Therefore, a positive sequence detector has to be inserted to extract the fundamental component of the phase voltage [33]. It will simply filter out components other than positive fundamental. The block diagram of a positive sequence detector is shown in Fig. 3-4.

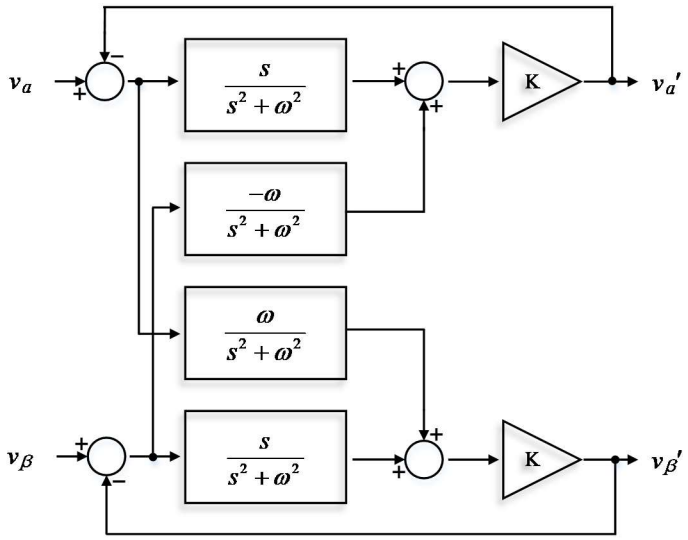

Fig. 3-4 Block diagram of the positive sequence detector

The instantaneous active and reactive power control is a very intuitive way to eliminate harmonic distortion and reactive power flow control. However, it requires the instantaneous calculation of *p*, *q,* which will increase the computation in the controller. Also, additional voltage sensors are required for *p* and *q* reference generation. The implementation is complicated due to the necessity of a positive sequence detector. Without reactive power flow regulation, the *p-q* theory is pricey for the selective harmonic cancellation.

3.2.2 Hysteresis control

Hysteresis current control is the simplest way to regulate current within the hysteresis band. However, the traditional hysteresis control method cannot achieve fixed-frequency switching and may result in EMI and harmonic filter design issues. Therefore, it is not suitable for an active power filter applications where EMI and harmonic resonance are concerns [34]. Instead, a fixed-frequency hysteresis control method is an alternative option for selective harmonic cancellation [34-37]. The improved hysteresis control schemes require phase-locked loop or feedforward control to keep the constant frequency. The fixed-frequency hysteresis control extended to 3 phase system and showed a good performance [38, 39].

Recently, parabolic current control was proposed [40]. It can be categorized as fixed-frequency hysteresis current control but does not require additional PLL or feedforward path in the control loop [40]. The operation of the parabolic current control technique is provided in Fig.3-5

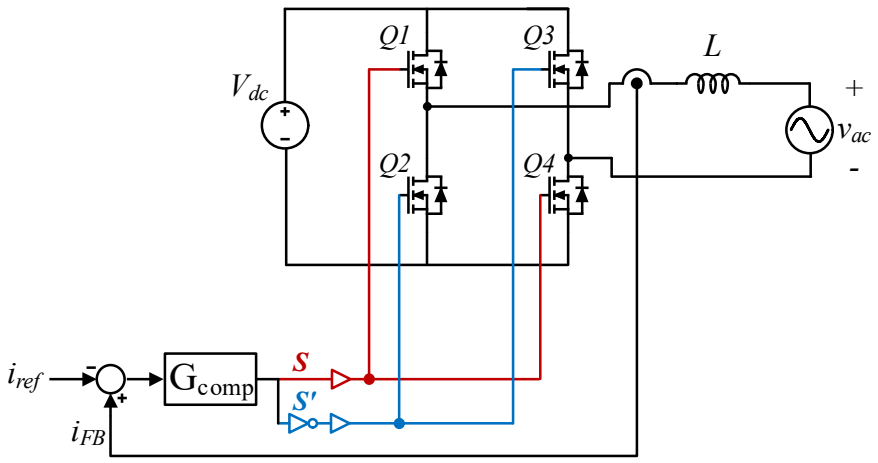

(a)

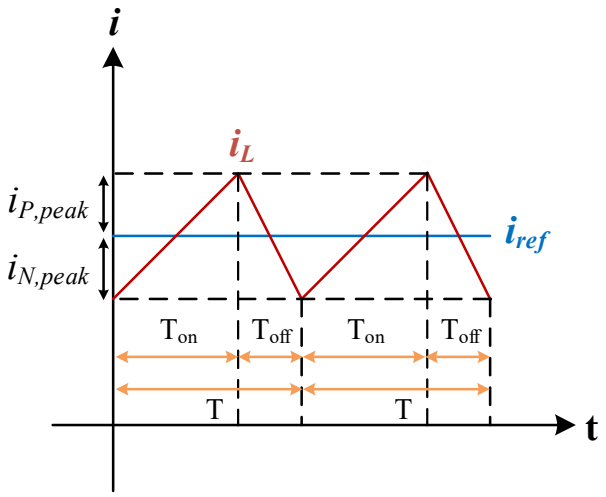

(b)

Fig. 3-5. Parabolic current control (a) circuit diagram (b) inductor current waveform

The peak value of inductor current error during one switching cycle can be calculated from the basic inductor voltage equation during duty on period and duty off period [40]

$$L\frac{d\Delta i}{dt} = V_{dc} - v_{ac} - L\frac{di_{ref}}{dt} = L\frac{\Delta i_{p-p}}{T_{on}} \tag{3.2.8}$$

$$-L\frac{d\Delta i}{dt} = -V_{dc} - v_{ac} - L\frac{di_{ref}}{dt} = -L\frac{\Delta i_{p-p}}{T_{off}}. \tag{3.2.9}$$

By substituting (3.2.9) to (3.2.8), positive peak error and negative peak error are provided as

$$\begin{aligned} \Delta i_{P,peak} &= \frac{\Delta i_{P-P}}{2} = \frac{V_{dc}T}{2L}\left[\frac{T_{on}}{T} - \left(\frac{T_{on}}{T}\right)^2\right] \\ \Delta i_{N,peak} &= \frac{\Delta i_{P-P}}{2} = \frac{V_{dc}T}{2L}\left[\frac{T_{off}}{T} - \left(\frac{T_{off}}{T}\right)^2\right] \end{aligned} \tag{3.2.10}$$

where $\Delta i_{P,\text{peak}}$ is the peak positive error and $\Delta i_{N,\text{peak}}$ is the peak negative error. If the current error is controlled within $\Delta i_{P,\text{peak}}$ and $\Delta i_{N,\text{peak}}$, the inductor current follows the reference current with fixed-switching frequency. Fig.3-6 shows the simulation waveform of parabolic current control.

The inductor current error is always within the parabolic carrier $F_{\_pa\_n}$ and $F_{\_pa\_p}$ with fixed-switching frequency and achieved good transient performance.

However, parabolic current control has two major drawbacks. First of all, it requires precise circuit parameters to calculate the peak current error. If the inductor saturation is not negligible, fixed-frequency switching cannot be achieved. Fig.3-7 provides the waveforms with 10 % inductor saturation. The loci of inductor current error is not periodic and therefore, the switching frequency is no longer fixed. Given that the permeability of the inductor core is dependent on the current magnitude, parabolic current control may not guarantee the fixed switching frequency operation and it may interact with LC network in point of common coupling (PCC). Second, it is very challenging to implement the parabolic current control in a 3-phase 3-wire system due to the fluctuation in neutral voltage.

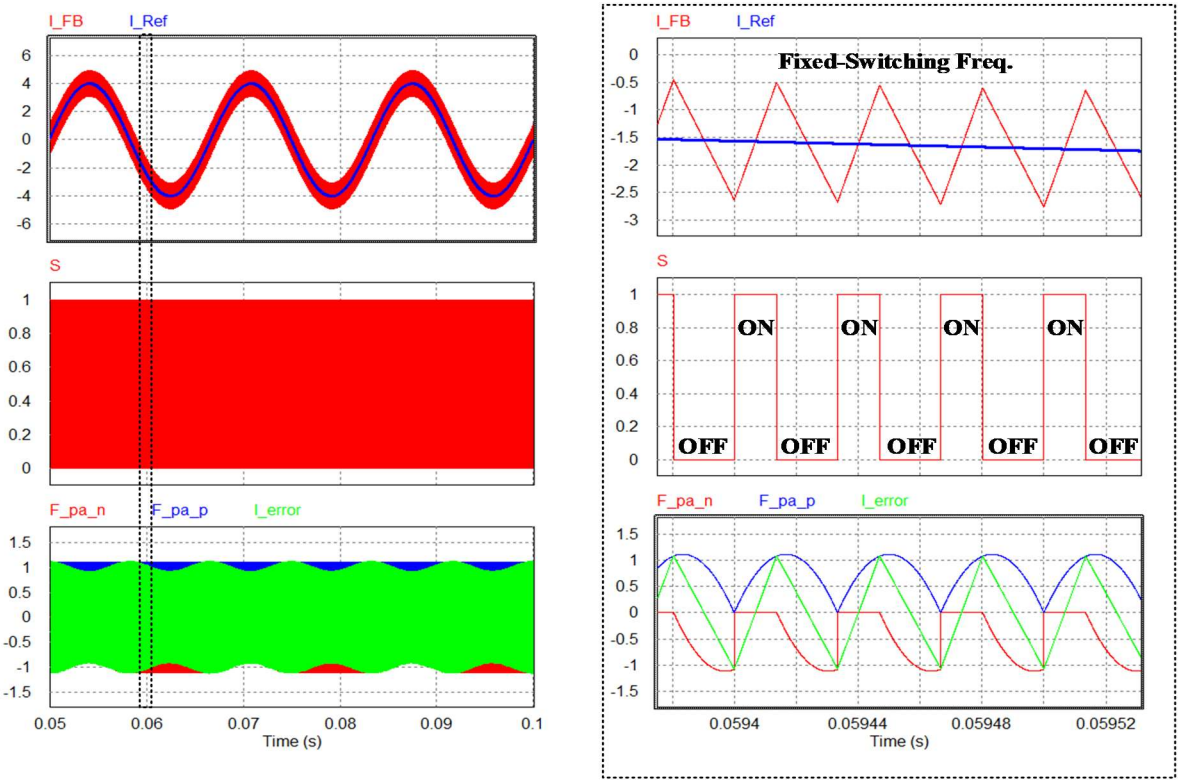

Fig. 3-6. Simulation waveform of parabolic current control without inductor saturation

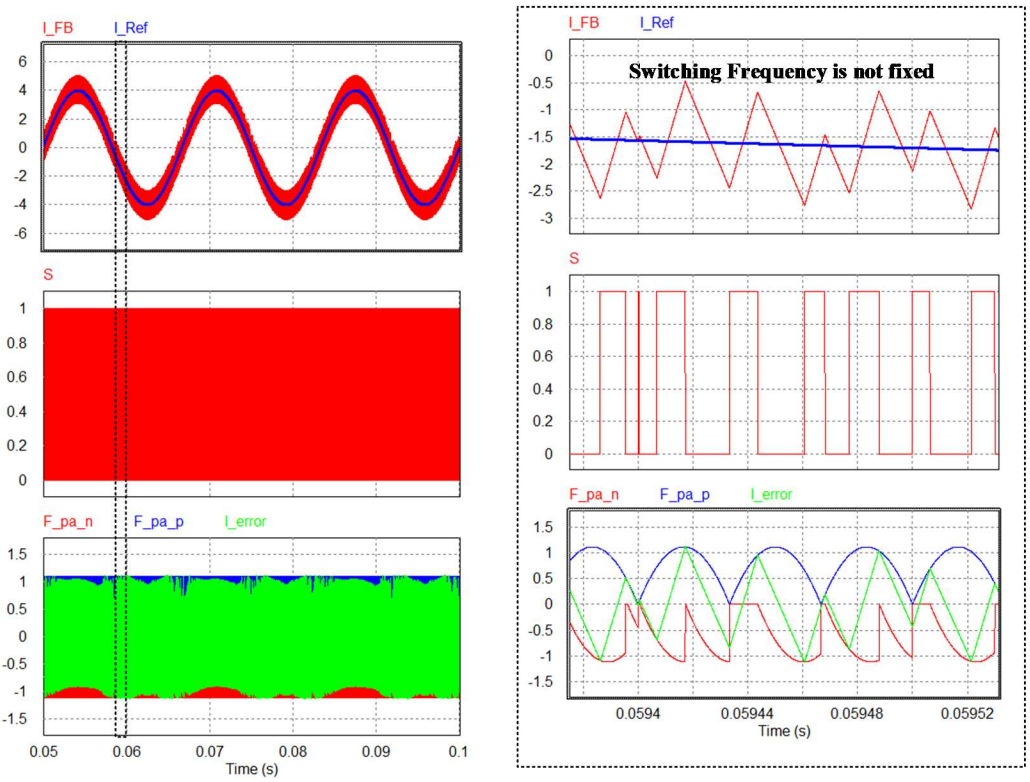

Fig. 3-7. Simulation waveform of parabolic current control with 10% inductor saturation

3.2.3 Proportional resonant current control

Proportional resonant (PR) controllers have been commonly used in active power filter applications [33, 41-44]. The implementation of PR compensator for selective harmonic cancellation was provided in [33, 41, 43, 45-47] and showed a good harmonic cancellation performance. The implementation of PR compensator can be either a stationary reference frame or a synchronous reference frame. In a synchronous reference frame, a compensator with the second-order resonant term is defined as a sinusoidal signal integrator [41]. In the stationary reference frame, a similar concept is defined as a generalized integrator [33].

In this proposed front-end, PR compensator in a synchronous reference frame is employed. In the synchronous reference frame, the number of required bandpass filter can be reduced by half

compared to the stationary reference frame. Fig.3-8 shows how the 6*k*-1(positive sequence) and 6*k*+1 (negative sequence) components are merged into 6*k* harmonics.

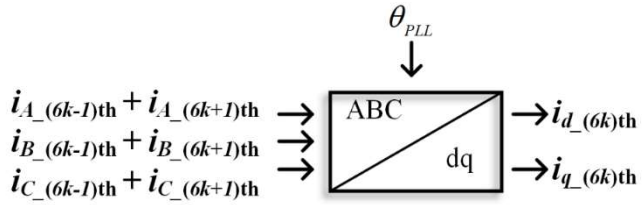

Fig. 3-8. dq transformation of 6*k*±1 harmonics

Fig. 3-9 shows the control block diagram of the active power filter for selective harmonic elimination. Theoretically, the transformer eliminates 6*k*±1 (*k*=1, 2, 3, ⋯) harmonics and therefore, it traps 5th, 7th, 17th, and 19th harmonics and the active power filter compensates for 11th and 13th harmonics. The proposed front-end does not provide compensation for 23rd and 25th harmonics but the amount of harmonic contents higher than 17th and 19th are negligible and do not significantly affect the system.

The harmonic reference generator is shown in Fig. 3-10. It extracts harmonic components from the load current by using the bandpass filter (BPF). As the target harmonic component is 720 Hz (12th harmonic) in the synchronous reference frame, the natural frequency of BPF ω_n is set to 720 Hz, which corresponds to 660 Hz(11th) and 780 Hz (13th) harmonics in abc coordinate system. The extracted harmonics serve as the harmonic current reference for G_{comp}. Additionally, the output of voltage regulator (PI) is added q-axis current reference i_q^* to regulate the dc bus voltage of the active power filter. It should be noted that the bandwidth of the voltage regulator has to be much lower than the bandwidth of the current regulator to avoid the interaction.

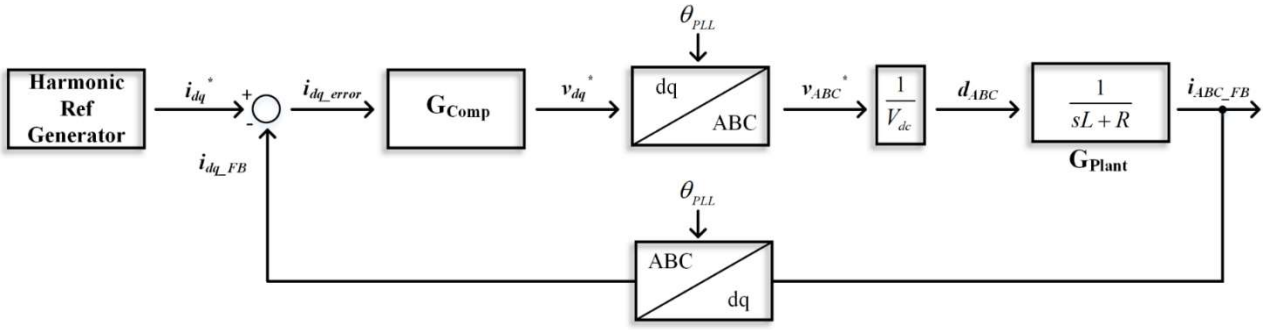

Fig. 3-9. Block diagram of the active power filter

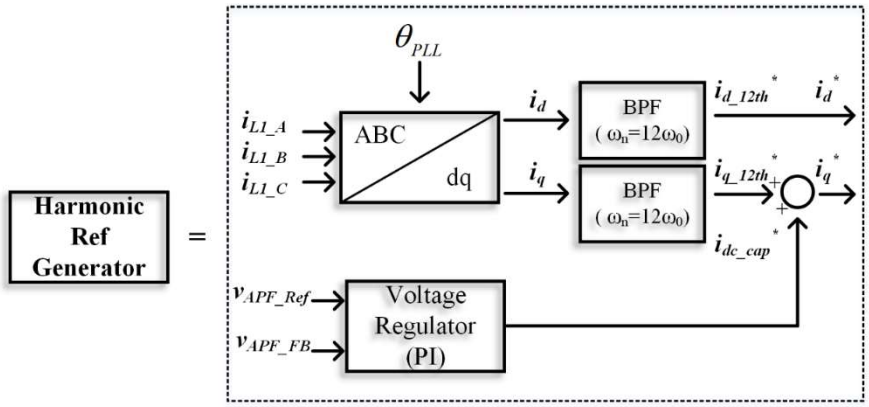

Fig. 3-10. Harmonic reference generator block diagram

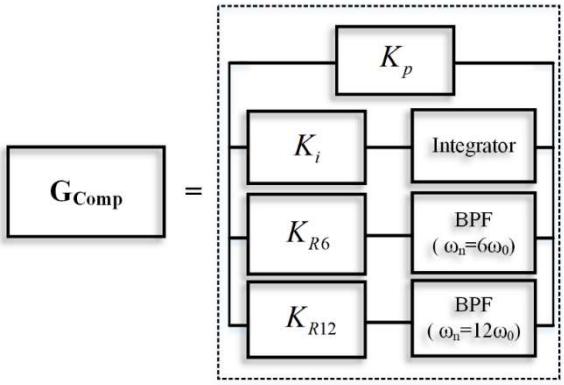

Fig. 3-11. Compensator (PI+R) block diagram

The bandpass filter (BPF) shown in the block diagram is presented as

$$G_{BPF\_Ideal} = \frac{2s}{s^2 + (h \times \omega_0)^2} \tag{3.2.11}$$

where h and ω_0 are harmonic order and the fundamental frequency respectively and utilized for grid-connected inverter control [48, 49]. The frequency response of an ideal bandpass filter is provided in Fig. 3-12. Ideally, BPF has to have infinite gain and 180 ° phase drop at the resonant frequency. In a digital implementation, it may results in numerical issue near the resonant frequency and eventually impact the system stability.

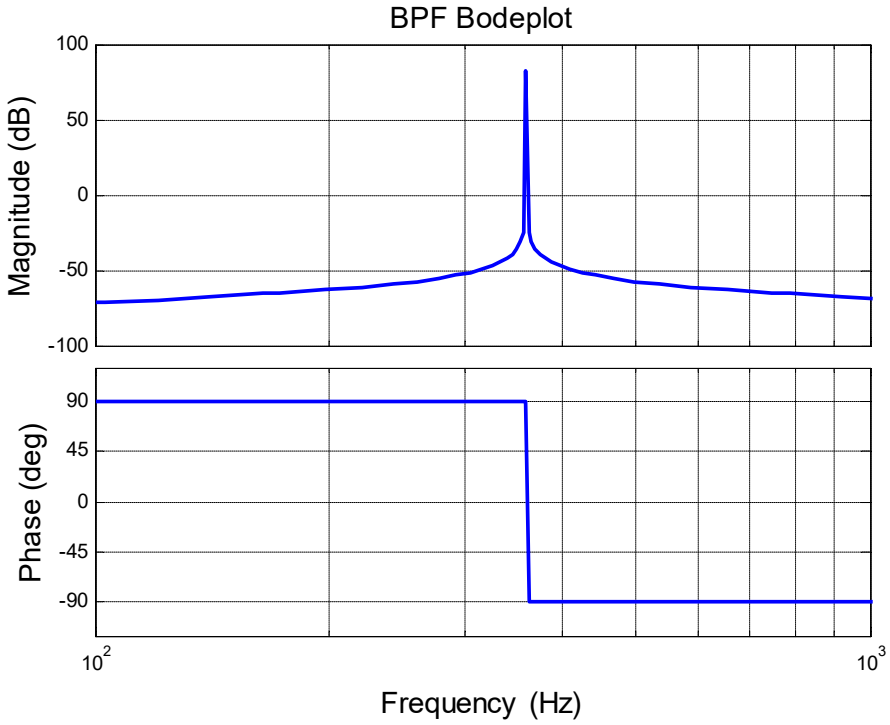

Fig. 3-12. The frequency response of the ideal BPF

Therefore practical BPF was proposed in [42, 50-52] and presented as

$$G_{BPF} = \frac{2\omega_c s}{s^2 + 2\omega_c s + (h \times \omega_0)^2}. \tag{3.2.12}$$

In (3.2.12), the gain at the resonant frequency is 1 and the infinite gain issue is eliminated. The bandwidth f_c (= ω_c /2π) determines Q factors. By introducing Q factor, the rate of change of the phase angle can be adjusted. The frequency response of practical BPF is provided in Fig.3-13.

The Proportional Resonant (PR) compensator with practical BPF is given as

$$G_{PR} = K_p + K_R \frac{2\omega_c s}{s^2 + 2\omega_c s + (h \times \omega_0)^2}. \tag{3.2.13}$$

At the resonant frequency, the gain is $K_P + K_R$. The bode plot of G_{PR} with 300 Hz resonant frequency with respect to f_c is shown in Fig. 3-14. Regardless of f_c, the peak magnitudes are the same. The smaller f_c is desired to selectively boost the gain at resonant frequency without affecting the magnitude and phase other than $h \times \omega_0$. However, if f_c becomes too small, the magnitude and phase change so rapid that it leads to numerical issues in dsp. In this paper, f_c is set to 5 Hz to avoid the aforementioned risks.

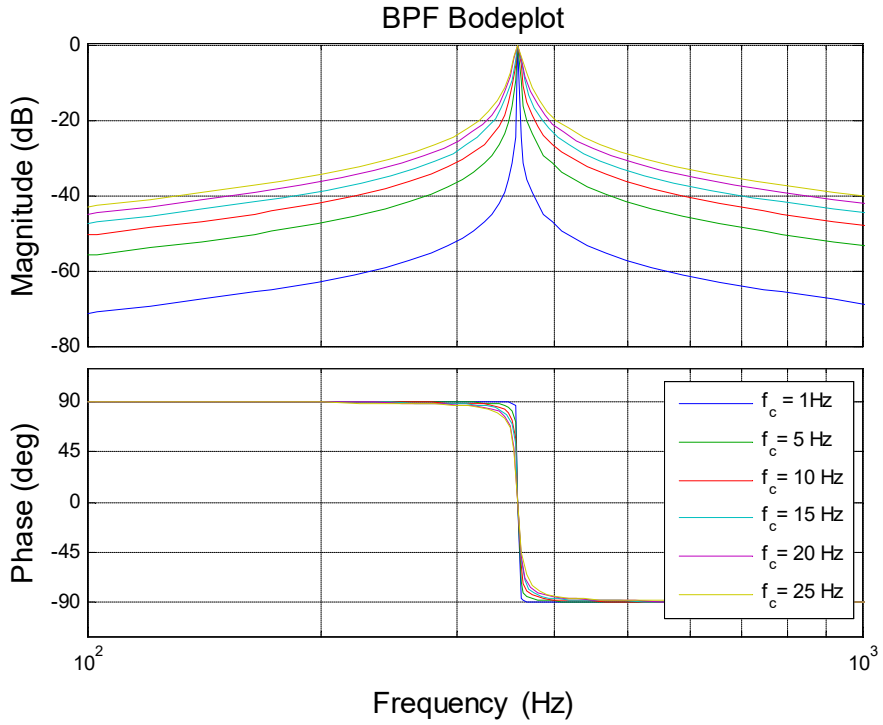

Fig. 3-13. The frequency response of realistic BPF in different bandwidths (Q factors)

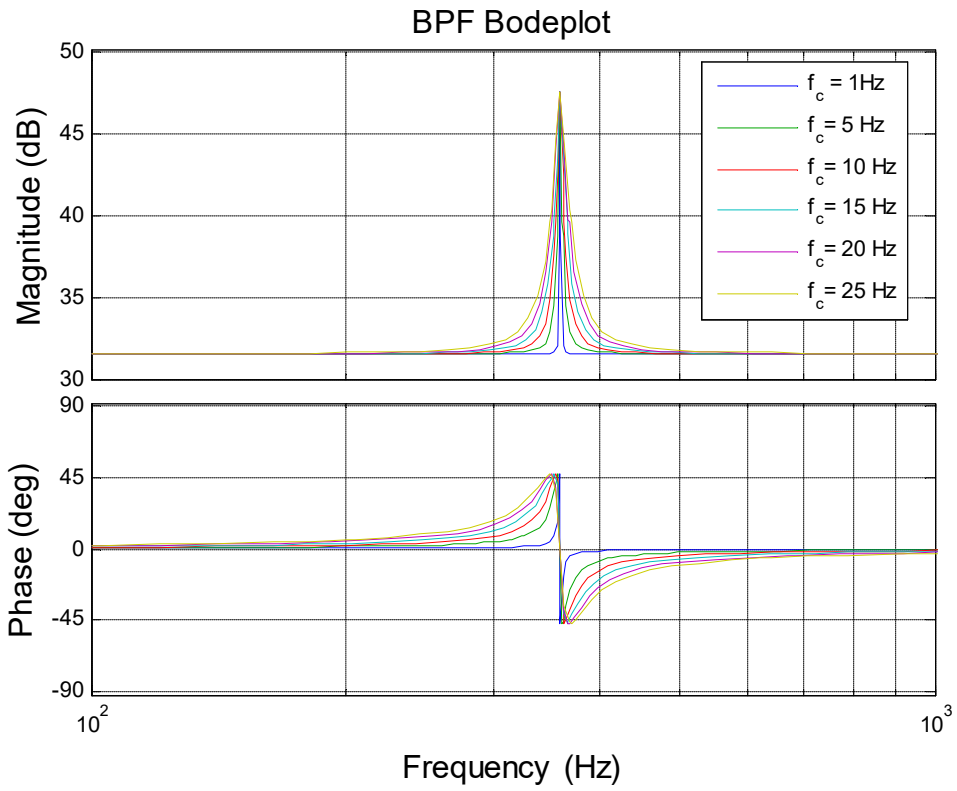

Fig. 3-14. The frequency response PR compensator in different bandwidths

The design of PI+R compensator (G_{comp}) is based on a well-known pole-zero cancellation method. It is assumed that BPF does not affect the frequency response of the overall system other than the resonant frequency to simplify the compensator design process. However, the resonant filters impact the overall loop and slightly change the pole location and may not achieve complete pole-zero cancellation. However, the impact of BPF with small bandwidth f_c is restricted to the resonant frequency and therefore, the effect BPF on pole location is ignored in this design. First of all, with the given inductance L and resistance R and the desired cross over frequency f_{cc}, the proportional gain and integral gain are calculated as

$$K_p = 2\pi f_{cc} \times L \tag{3.2.14}$$

$$K_i = 2\pi f_{cc} \times R \tag{3.2.15}$$

Then pole of PI compensator cancels the zero of the plant so that the forward path gain $G_{PI}\times G_{PWM}\times G_{plant}$ becomes 1st order system

$$G_{PI}\times G_{PWM}\times G_{Plant}=\frac{K_p}{sL}. \tag{3.2.16}$$

The PI compensator has a sufficient gain at low frequency. However, it is not suitable for a sinusoidal reference tracking. The magnitude of the loop gain of the designed compensator ($f_c = 3$ kHz) at 360 Hz and 720 Hz are 18.2dB and 12.5 dB respectively and the compensator will have a significant steady-state error at these frequencies. The resonant filters with gains are inserted to boost the gain at 6th and 12th harmonic components. The resonant gain K_{R6} and K_{R12} are selected to achieve above 40 dB at resonant frequencies. The bode plots of PI, PI+R, and PI+R including the digital delay are provided in Fig. 3-15. To minimize the effect of sampling and PWM update delay, a double sampling technique is utilized and the digital delay T_{delay} is 16.67 us.

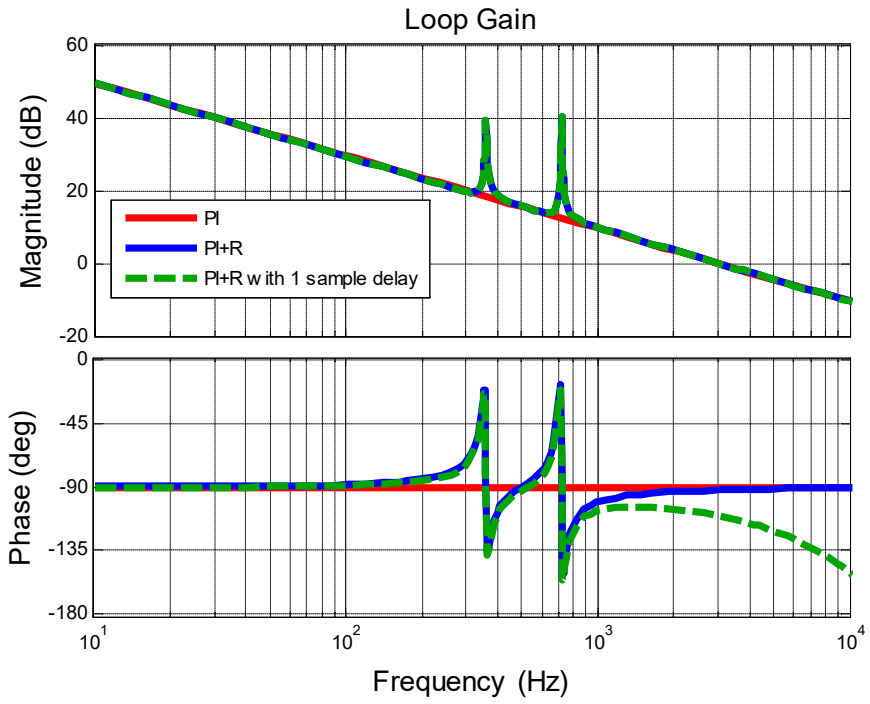

Fig. 3-15. The loop gain of PI, PI+R, and PI+R with digital delay

Overall, PI and PI+R have similar frequency response except for resonant frequencies. It verifies that the resonant filters do not significantly impact the pole-zero cancellation. In both 360 Hz and 720 Hz, the loop gain achieved 40 dB gain as designed. The control parameters are summarized in Table 3-3.

Table 3-3. Control parameters

Symbol	Parameters	Value
L	APF inductance	0.7 mH
R	APF resistance	0.01 Ω
f_{CC}	Cross over frequency	3 kHz
f_{SW}	Switching frequency	32 kHz
f_{Samp}	Sampling frequency	64 kHz
K_P	Proportional gain	14.14
K_I	Integral gain	188.5
K_{R6}	Resonant gain (360 Hz)	200
K_{R12}	Resonant gain (720 Hz)	450

The phase margin of the control loop including the digital delay is 69.8° and the system is stable.

3.3 The verification of the proposed front-end

PSIM simulation and experimental tests are conducted to validate the proposed front-end. The control parameters are identical to Table 3-3 and the test setup parameters are provided in Table 3-2.

Table 3-4. Simulation and hardware specification

Symbol	Parameters	Value
V_{G1}	Genset1 line to line voltage	70 V
V_{G2}	Genset2 line to line voltage	70 V
R_{Load}	Resistive load	4 Ω
C_{dc}	Load capacitance	4.4 mF
L_{leak}	Leakage inductance	0.147 mH
L_{mag}	Magnetizing Inductance	207 mH
L_S	Source inductance	1.5mH
C_{APF}	dc link capacitance (APF)	4.4 mF
V_{dc_APF}	dc-link voltage (APF)	120 V

Typically, multi-megawatt gensets in a shipboard power system are rated for 440 V or 690 V. Due to the limited test environment, the two gensets in the power system were replaced by two inverters and the output power is scaled down to 1.0 kW. Also, the line to line voltage of the prototype system is scaled down to 70 V. Fig. 3-16 (a) shows the source, transformer, and load currents with the passive front-end (shunt phase-shift transformer rectifier). As shown in Chapter 2, the passive front-end effectively eliminate $6k \pm 1$ (k = 1, 3, 5, ···) harmonics. Both Y-side and Δ-side source currents i_{SA_Y}, i_{SA_Δ} have much better THD compared to the load currents i_{LA_Y}, i_{LA_Δ}. Fig. 3-16 (b) shows the source, transformer, and load currents with the hybrid front-end (shunt phase-shift transformer + 3-phase active power filter). The shunt active power filter further eliminates 11th and 13th harmonics on both i_{SA_Y}, i_{SA_Δ}. THD of i_{SA_Y}, i_{SA_Δ} are reduced from 5.93% to 4.5% and 4.48% respectively. The frequency spectra of i_{LA_Y}, i_{LA_Δ} are presented in Fig. 3-17. It is clearly shown that 11th (660 Hz) and 13th (780 Hz) harmonics are reduced by more than 85 % on Y-side. Also, Δ-side harmonics are reduced by 70 %. Theoretically, the harmonic cancellation performance of both sides has to be the same with the ideal phase-shift transformer, which has zero leakage inductance L_{leak} and infinite magnetizing inductance L_{mag}. However, due to the non-zero leakage inductance L_{leak} and finite magnetizing inductance L_{mag} of the transformer, the amount of injected 11th and 13th harmonics to Δ-side is decreased and slightly degrade the harmonic cancellation performance on Δ-side.

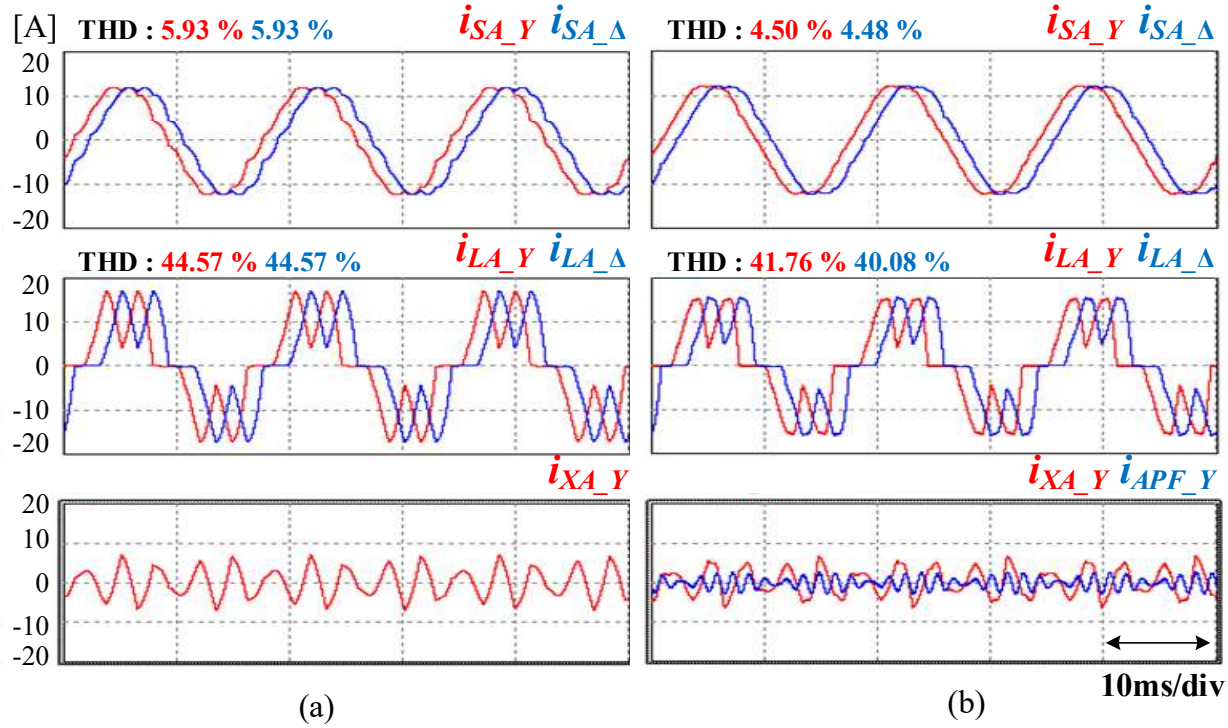

Fig. 3-16. Time-domain waveforms (a) passive front-end simulation (b) hybrid front-end simulation waveform

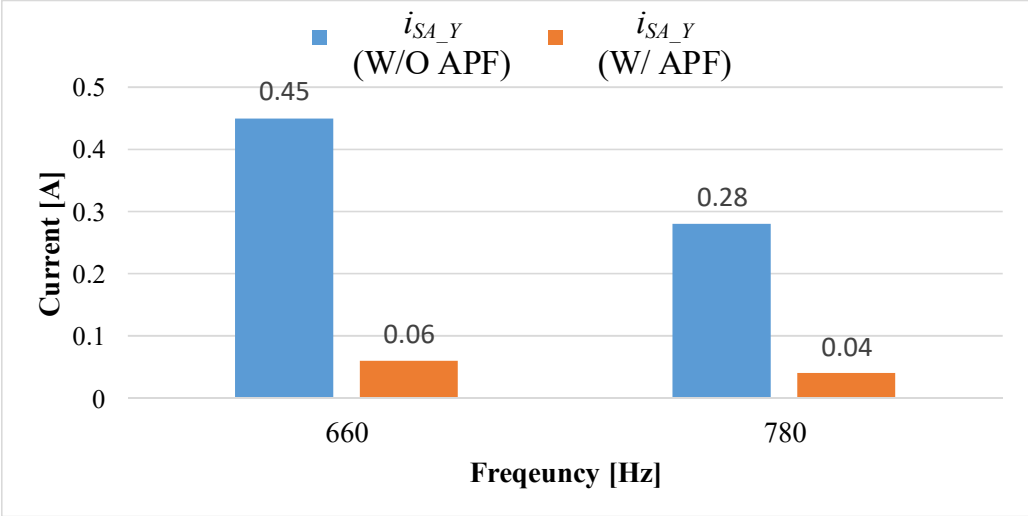

(a)

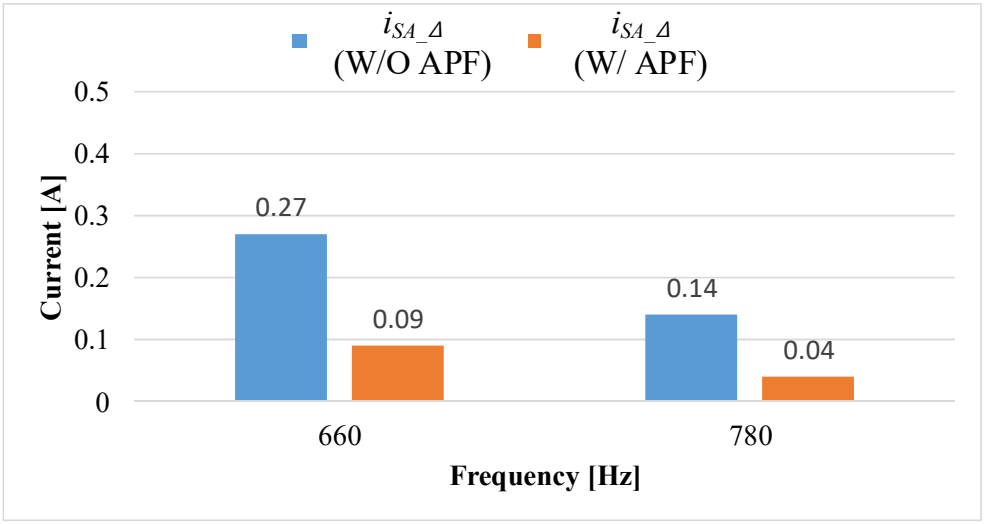

(b)

Fig. 3-17. The frequency spectra of 11th and 13th harmonic component (a) Y-side source current with and without active harmonic cancellation (b) Δ-side source current with and without active harmonic cancellation

In Fig. 3-18, the experimental waveforms of prototype hardware are provided. The experimental setup follows the same specification provided in Table II. SiC MOSFET (SCT3022KL) based 3-phase active front-end and the 2 VSIs in ac mains are controlled by TMS320F28377D. The active harmonic cancellation is turned on at 40 *ms* and it starts to inject 11th and 13th harmonics to the point of common coupling.

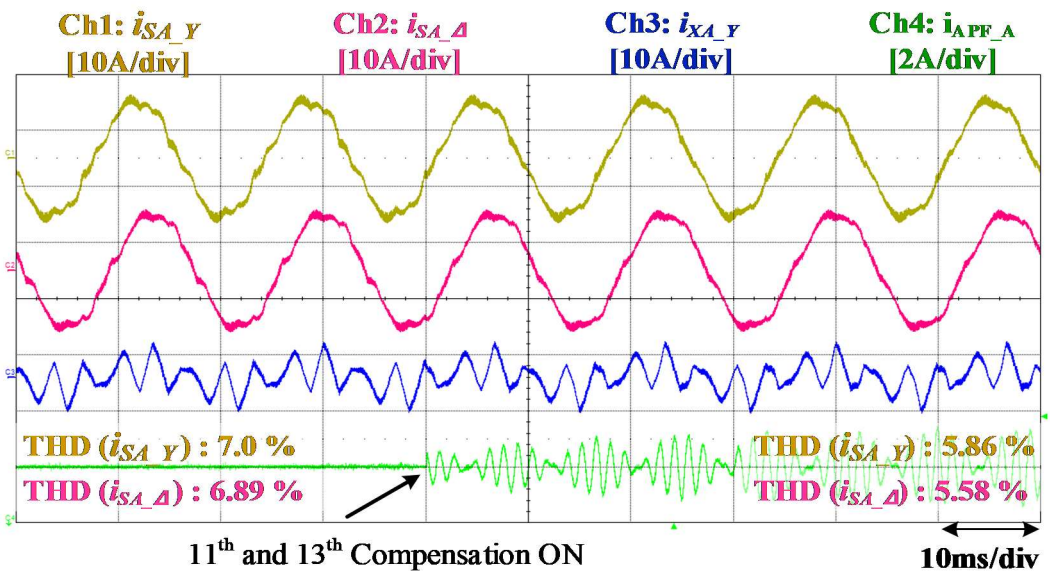

Fig. 3-18. Experimental test waveform with and without 11th and 13th harmonic compensation

THD of Y-side source current i_{SA_Y} is reduced from 7.0 % to 5.86 %. Also, THD of Δ-side source current is reduced from 6.89% to 5.58 %. The frequency spectra of 11th and 13th harmonics are provided in Fig. 3-19. The active harmonic compensation achieves 80% and 65% harmonic reduction for i_{SA_Y} and i_{SA_Δ} respectively.

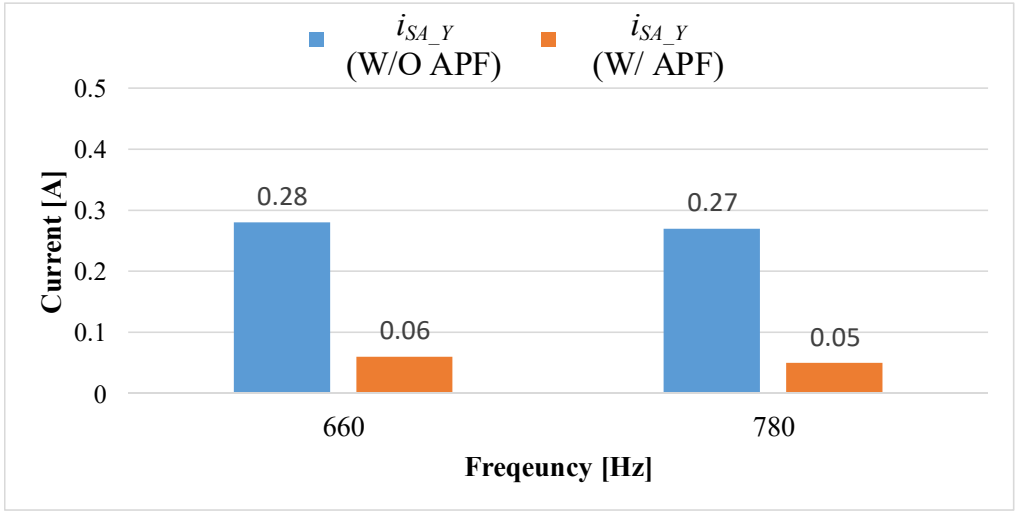

(a)

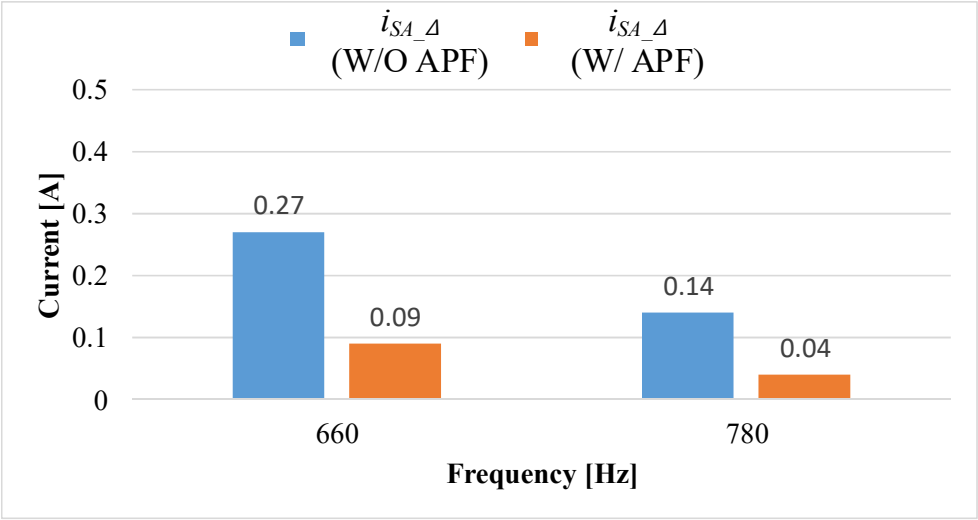

(b)

Fig. 3-19. The frequency spectra of 11th and 13th harmonic component (a) Y-side source current with and without active harmonic cancellation (b) Δ-side source current with and without active harmonic cancellation

3.4 Summary

In this chapter, a hybrid front-end, which consists of the shunt phase-shift transformer and active power filter is proposed. The most significant harmonic contents, 5th, and 7th harmonics are eliminated by the passive front-end and the second most significant harmonics, 11th and 13th harmonics are canceled by active power filter. As the active power filter only deals with the 11th and 13th harmonics, the power rating for the active power filter is less than 10% of genset output. In theory, the most significant harmonics seen from ac mains is pushed to 1380 Hz and the harmonic distortion in ac mains is significantly improved.

Among various control methods, PI+R compensator is utilized for selective harmonic cancellation and dc-link voltage control. The bode plot of designed compensator shows enough gain at low frequency, and 360 Hz and 720 Hz without stability issue.

PSIM simulation validates the effectiveness of the proposed front-end. The simulation results show that more than 70% of 11th and 13th harmonics in both Y-side and Δ-side source

currents are canceled by active power filter. The experimental waveforms from the prototype hardware show that more than 65 % reduction in 11^{th} and 13^{th} harmonics in both ac mains.

Overall, the performance of the proposed front-end is comparable to 24 pulse converter with much reduced low-frequency magnetics. Although proposed front-end requires dsp and active component, it is attractive to shipboard power system where the overall size and weight of the front-end are critical.

Chapter 4

Back to back active power filter for multi-genset system

In this chapter, a back to back active power filter is proposed. The theoretical background will be provided and the performance of the proposed front-end is validated by simulation and experimental test results.

4.1 Theoretical background for back to back active power filter

The concept of back to back active power filter is straight forward. The back to back APF replaces the shunt phase-shift transformer in multi-genset power system and actively compensates for the harmonic contents. The single line diagram of shunt phase-shift transformer and back to back active power filter are provide in Fig.4-1.

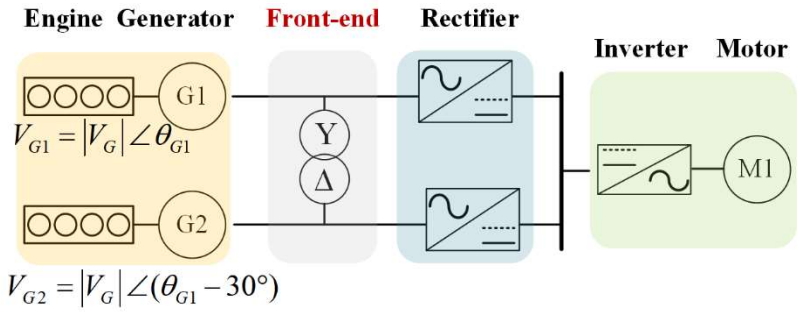

(a)

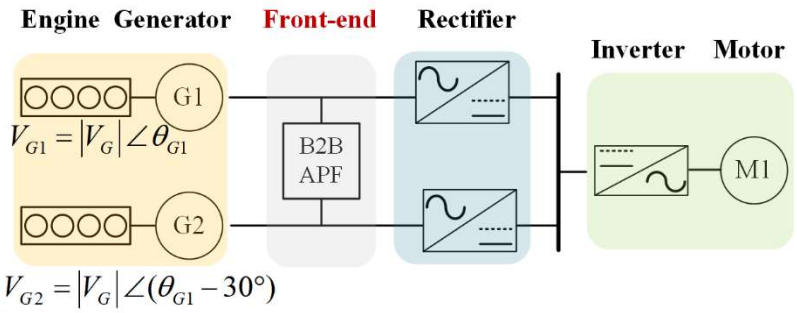

(b)

Fig. 4-1 The single line diagram of (a)shunt phase-shift transformer (b) back to back active power filter

Similar to the shunt phase-shift transformer, it only involves in the harmonics and accordingly the rating of APF is a fraction of the generator output. Fig.4-2 and Fig.4-3 show the 3-phase circuit diagram of back to back APF and a single-phase equivalent circuit diagram respectively. In this configuration, 3-phase voltage sources V_{S1} and V_{S2} supply the fundamental current (60 Hz) and the remaining harmonic components are supplied by back to back APF

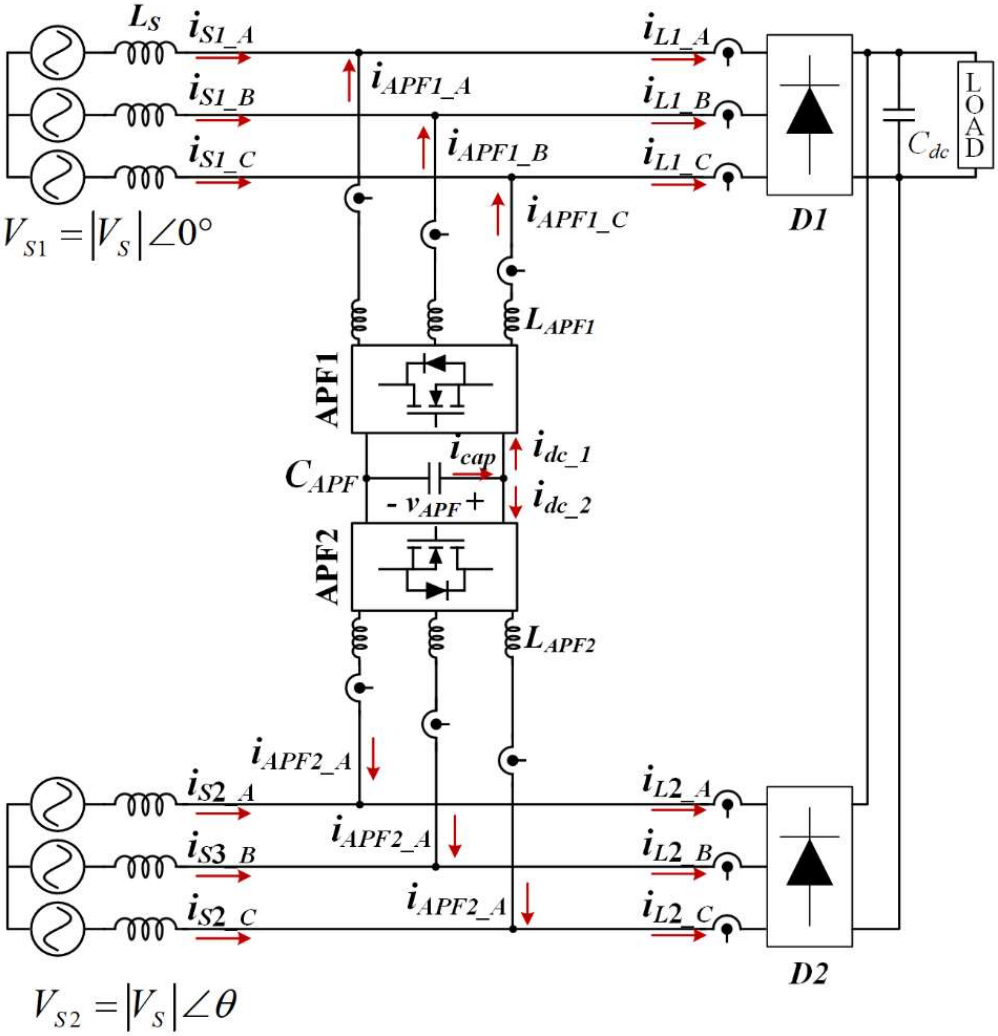

Fig. 4-2. Circuit diagram of 2 genset-based system with back to back front-end

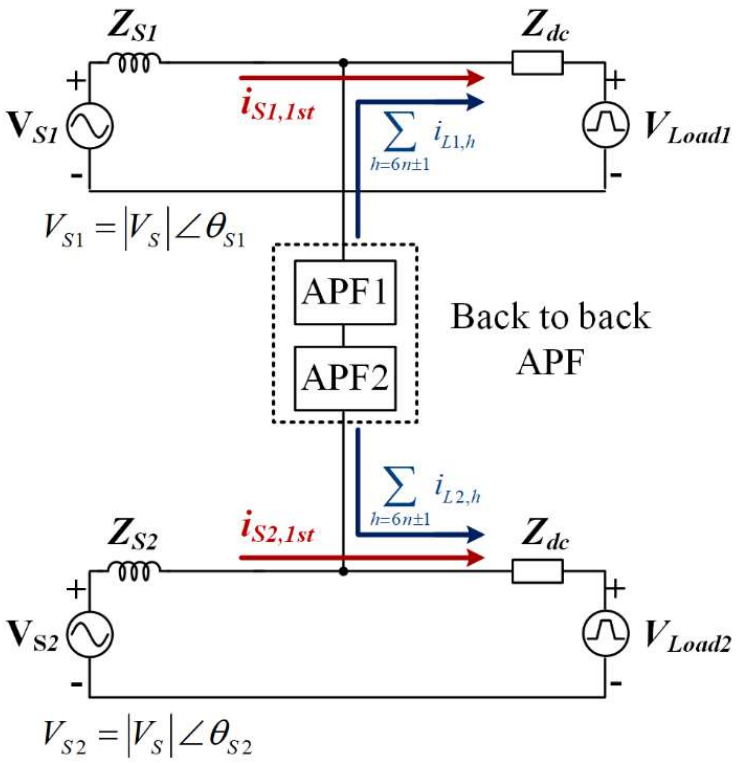

Fig. 4-3. Single line diagram of 2 genset-based system with back to back front-end

The back to back APF is similar to 2 independent APFs configuration. 3 phase circuit diagram of back to back APF and 2 independent APFs are provided in Figs. 4-4 (a) and (b).

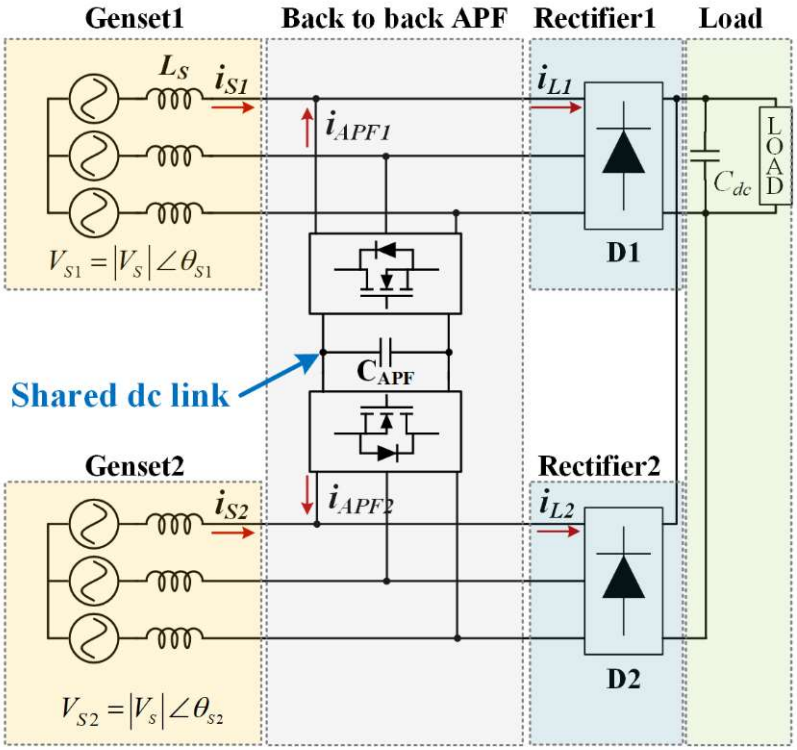

(a)

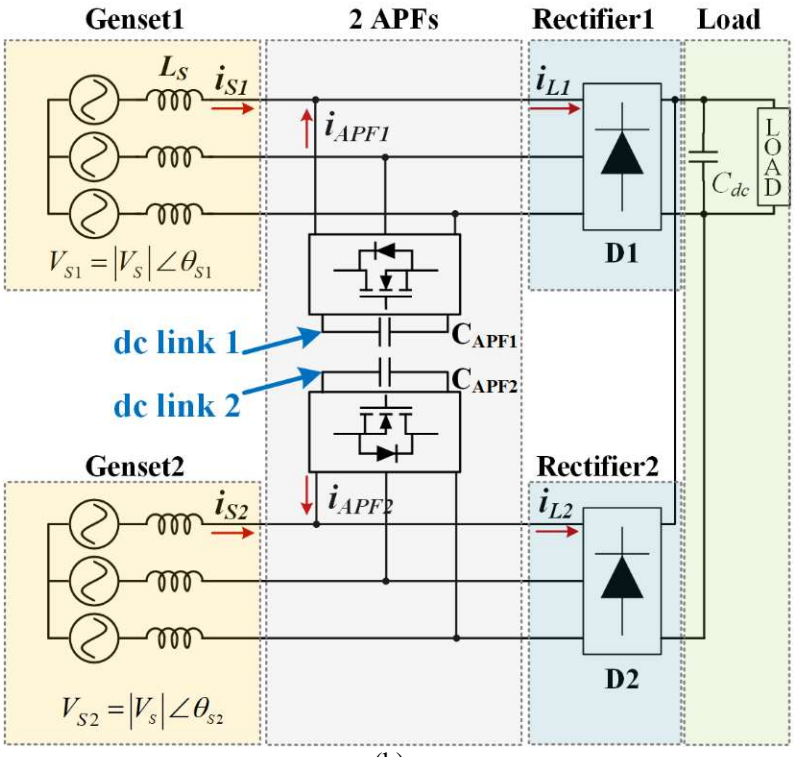

(b)

Fig. 4-4. Circuit diagram of 2 genset-based system with (a) back to back APF (b) 2 independent APFs

The main difference can be found from the shared dc bus. As shown in Fig.4-3 (a), two 3-phase full-bridge inverters share the dc-link bus and only a single capacitor is required. Accordingly, the number of required voltage loop is reduced by half. The prominent advantage of back to back APF with phase angle configurable genset is the voltage ripple reduction in the shared dc link. It will be significantly reduced and eventually the required capacitor size is reduced. Overall, the proposed front-end is advantageous in terms of physical size, cost, and lifespan by reducing the voltage ripple.

4.2 dc-link capacitor current analysis

The basic capacitor current and voltage equations are provided as

$$i_{cap} = C_{APF} \frac{dv_{APF}}{dt} \tag{4.2.1}$$

$$\Delta v_{APF} = \frac{1}{C_{APF}} \int i_{cap} dt \tag{4.2.2}$$

where i_{cap}, C_{APF}, and v_{APF} are capacitor current, APF dc-link capacitor, and APF dc-link voltage respectively. Although the average of the voltage ripple in steady-state reaches zero, the instantaneous voltage is directly affected by the capacitor current. The voltage ripple Δv_{APF} can be decreased by either increasing the size of the capacitor or reducing the capacitor current ripple. In general, the large capacitor is not desired because it will increase the overall cost and volume of the system.

By nature of the capacitor current, it will not have dc component in steady-state and it only contains harmonics. The capacitor current and dc-link current of upper and lower APF is found from Kirchhoff's Current Law (KCL)

$$i_{cap} = i_{dc1} + i_{dc2} \tag{4.2.3}$$

where i_{dc1} and i_{dc2} are the dc-link current of APF1 and APF2 respectively and the dc-link currents of APFs are provided as

$$i_{dc1} = \mathbf{i}_{\mathbf{APF1\_ABC}} \bullet \mathbf{d}_{\mathbf{APF1\_ABC}} \tag{4.2.4}$$

$$= [i_{APF1\_A} \;\; \mathrm{i}_{APF1\_B} \;\; \mathrm{i}_{\_APF1\_C}] \bullet [d_{APF1\_A} \;\; \mathrm{d}_{APF1\_B} \;\; \mathrm{d}_{\_APF1\_C}]^{\mathrm{T}}$$

$$i_{dc2} = \mathbf{i}_{\mathbf{APF2\_ABC}} \bullet \mathbf{d}_{\mathbf{APF2\_ABC}} \tag{4.2.5}$$

$$= [i_{APF2\_A} \;\; \mathrm{i}_{APF2\_B} \;\; \mathrm{i}_{\_APF2\_C}] \bullet [d_{APF2\_A} \;\; \mathrm{d}_{APF2\_B} \;\; \mathrm{d}_{\_APF2\_C}]^{\mathrm{T}}$$

$\boldsymbol{i_{APF1\_ABC}}$ **(**$\boldsymbol{i_{APF2\_ABC}}$**)** and $\boldsymbol{d_{APF1\_ABC}}$ (**d**$_{APF2\_ABC}$) are the vector-matrix that represents A, B, C phase current and duty cycle of APF1 (APF2). The phase-A current of i_{APF1_A} and i_{APF2_A} under the steady-state condition can be expressed as the summation of harmonics

$$\begin{aligned} i_{APF1\_A} &= I_5 \sin 5\omega t + I_7 \sin 7\omega t + I_{11} \sin 11\omega t + \cdots \\ &= I_h \sum_{h=6k\pm1}^{\infty} \sin(h\omega t) \end{aligned} \tag{4.2.6}$$

$$\begin{aligned} i_{APF2\_A} &= I_5 \sin 5(\omega t - \theta) + I_7 \sin 7(\omega t - \theta) + I_{11} \sin 11(\omega t - \theta) + \cdots \\ &= I_h \sum_{h=6k\pm1}^{\infty} \sin(h(\omega t - \theta)) \end{aligned} \tag{4.2.7}$$

The phase angle difference θ is determined by the phase angle difference between V_{S1} and V_{S2}. Among all harmonic frequency components, 5th and 7th are the most significant components in the i_{APF1} and i_{APF2}. The A-phase duty cycle of d_{APF1_A} and d_{APF2_A} are presented as

$$\begin{aligned} d_{APF1\_A} &= D_1 \sin \omega t + D_5 \sin 5\omega t + D_7 \sin 7\omega t + D_{11} \sin 11\omega t + \cdots \\ &= D_1 \sin \omega t + D_h \sum_{h=6k\pm1}^{\infty} \sin(h\omega t) \end{aligned} \tag{4.2.8}$$

$$\begin{aligned} d_{APF2\_A} &= D_1 \sin(\omega t - \theta) + D_5 \sin 5(\omega t - \theta) + D_7 \sin 7(\omega t - \theta) + D_{11} \sin 11(\omega t - \theta) + \cdots \\ &= D_1 \sin(\omega t - \theta) + D_h \sum_{h=6k\pm1}^{\infty} \sin(h(\omega t - \theta)) \end{aligned} \tag{4.2.9}$$

The most significant component in d_{APF1_A} and d_{APF2_A} is the fundamental component for 60 Hz disturbance rejection at the point of common coupling. The dc-link current induced by A phase current and duty is

$$\begin{aligned} i_{dc1\_A} &= i_{APF1\_A} \cdot d_{APF1\_A} \\ &= I_h \sum_{h=6k\pm1}^{\infty} \sin(h\omega t) \cdot (D_1 \sin \omega t + D_h \sum_{h=6k\pm1}^{\infty} \sin(h\omega t)). \end{aligned} \tag{4.2.10}$$

The multiplication of i_{APF1_A} and d_{APF1_A} has a long list of frequency component and it is difficult to extract meaningful information. For analytical derivation purposes, the most significant terms are considered to simplify the equations. Firstly. The dc-link current originated from the multiplication of fundamental duty cycle and 5th and 7th harmonics are considered

$$\begin{aligned} i_{dc1\_A} &\simeq (I_5 \sin 5\omega t + I_7 \sin 7\omega t) \cdot (D_1 \sin \omega t) \\ &\simeq I_5 \sin 5\omega t \cdot D_1 \sin \omega t + I_7 \sin 7\omega t \cdot D_1 \sin \omega t \\ &\simeq -\frac{I_5 D_1}{2} \{\cos(6\omega t) - \cos(4\omega t)\} - \frac{I_7 D_1}{2} \{\cos(8\omega t) - \cos(6\omega t)\}. \end{aligned} \tag{4.2.11}$$

dc link current induced by B and C phase i_{dc1_B}, i_{dc1_C} are ±120° apart from i_{dc1_A} and presented a

$$\begin{aligned} i_{dc1\_B} &= i_{APF1\_B} \cdot d_{APF1\_B} \\ &= -\frac{I_5 D_1}{2} \{\cos(6\omega t - 4\pi)) - \cos(4\omega t - \frac{8\pi}{3})\} \\ &\quad -\frac{I_7 D_1}{2} \{\cos(8\omega t - \frac{16\pi}{3}) - \cos(6\omega t - \frac{4\pi}{3})\} \end{aligned} \tag{4.2.12}$$

$$\begin{aligned} i_{dc1\_C} &\simeq -\frac{I_5 D_1}{2} \{\cos(6\omega t + 4\pi)) - \cos(4\omega t + \frac{8\pi}{3})\} \\ &\quad -\frac{I_7 D_1}{2} \{\cos(8\omega t + \frac{16\pi}{3}) - \cos(6\omega t + \frac{4\pi}{3})\}. \end{aligned} \tag{4.2.13}$$

From (4,1,11), (4,1,12), and (4,1,13) i_{dc1} is presented as

$$i_{dc1} = i_{dc1\_A} + i_{dc1\_B} + i_{dc1\_C}. \tag{4.2.14}$$

The summation of 4th and 8th harmonics in (4,1,11), (4,1,12), and (4,1,13) cancel each other because these components are phase-shifted by 120°

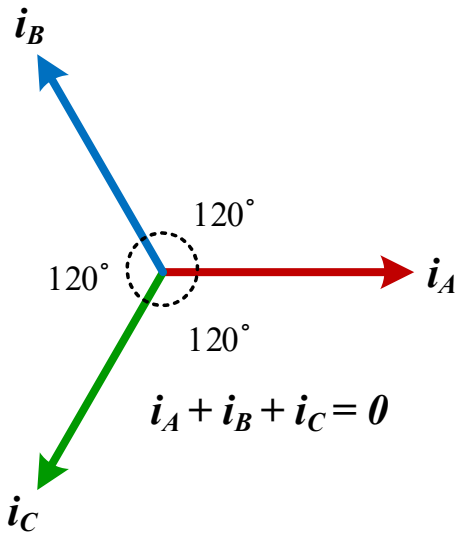

Fig. 4-5. Phasor diagram of a balanced 3 phase condition

Finally, i_{dc1} only contains 6th harmonic component

$$i_{dc1} \simeq -\frac{3(I_5 - I_7)D_1}{2}\cos(6\omega t). \tag{4.2.15}$$

Likewise, the dc-link current in lower side APF i_{dc2_ABC} is derived as

$$\begin{aligned} i_{dc2\_A} \simeq & -\frac{I_5 D_1}{2}\{\cos(6\omega t - 6\theta) - \cos(4\omega t - 4\theta)\} \\ & -\frac{I_7 D_1}{2}\{\cos(8\omega t - 8\theta) - \cos(6\omega t - 6\theta)\} \end{aligned} \tag{4.2.16}$$

$$\begin{aligned} i_{dc2\_B} \simeq & -\frac{I_5 D_1}{2}\{\cos(6\omega t - 4\pi - 6\theta) - \cos(4\omega t - \frac{4\pi}{3} - 4\theta)\} \\ & -\frac{I_7 D_1}{2}\{\cos(8\omega t - \frac{16\pi}{3} - 8\theta) - \cos(6\omega t - \frac{4\pi}{3} - 6\theta)\} \end{aligned} \tag{4.2.17}$$

$$\begin{aligned} i_{dc2\_C} \simeq & -\frac{I_5 D_1}{2}\{\cos(6\omega t + 4\pi - 6\theta) - \cos(4\omega t + \frac{4\pi}{3} - 4\theta)\} \\ & -\frac{I_7 D_1}{2}\{\cos(8\omega t + \frac{16\pi}{3} - 8\theta) - \cos(6\omega t + \frac{4\pi}{3} - 6\theta)\}. \end{aligned} \tag{4.2.18}$$

Again, i_{dc2} is approximated as

$$\begin{aligned} i_{dc2} &\simeq i_{dc2\_A} + i_{dc2\_B} + i_{dc2\_C} \\ &\simeq -\frac{3(I_5 - I_7)D_1}{2}\cos(6\omega t - 6\theta). \end{aligned} \tag{4.2.19}$$

Then the capacitor current is simplified as

$$i_{cap} \simeq -\frac{3(I_5 - I_7)D_1}{2}\cos(6\omega t) - \frac{3(I_5 - I_7)D_1}{2}\cos(6\omega t - 6\theta). \tag{4.2.20}$$

By taking into account all the current harmonics, (4.1.14) is extended to

$$i_{cap} = \sum_{h=6n} -\frac{3(I_{h-1} + I_{h+1})}{2} D_1[\cos(h\omega t) + \cos(h\omega t - h\theta)] \tag{4.2.21}$$

$$\begin{aligned} &= -\frac{3(I_5 + I_7)}{2} D_1[\cos(6\omega t) + \cos(6\omega t - 6\theta)] \\ &\quad -\frac{3(I_{11} + I_{13})}{2} D_1[\cos(12\omega t) + \cos(12\omega t - 12\theta)] \\ &\quad -\frac{3(I_{17} + I_{19})}{2} D_1[\cos(18\omega t) + \cos(18\omega t - 18\theta)] \\ &\quad -\frac{3(I_{23} + I_{24})}{2} D_1[\cos(24\omega t) + \cos(24\omega t - 24\theta)] \\ &\quad \vdots \end{aligned}$$

(4.1.21) shows that h=6n harmonics also can be eliminated by selecting a specific phase angle. The phase angle difference θ that brings 180° phase-shift between the h^{th} harmonic components can be derived as

$$\theta_{hth} = \pm\frac{180°}{h} \times (2n - 1). \tag{4.2.22}$$

6th, 12th, and 18th harmonics can be canceled out with the specific θ_{hth}. The derivation results are summarized in Table 4-1.

Table 4-1. The critical phase-shift angle for h^{th} harmonic elimination

	6^{th} harmonic cancellation	12^{th} harmonic cancellation	18^{th} harmonic cancellation	24^{th} harmonic cancellation
Phase angle	$\pm 30° \times (2n-1)$	$\pm 15° \times (2n-1)$	$\pm 10° \times (2n-1)$	$\pm 7.5° \times (2n-1)$

For example, the 6^{th} harmonic component in capacitor current $i_{cap,6th}$ can be eliminated by adjusting the phase angle difference θ to $30°$. Then the two cosine terms have $180°$ phase-shifted and cancel each other

$$i_{cap,6th} = -\frac{3(I_5 + I_7)}{2} D_1[\cos(6\omega t) + \cos(6\omega t - 180)] = 0. \quad (4.2.23)$$

In the same way, the 12^{th} harmonic component $i_{cap,6th}$ can be eliminated if the phase angle difference θ_{12th} is set to $15°$

$$i_{cap,12th} = -\frac{3(I_{11} + I_{13})}{2} D_1[\cos(12\omega t) + \cos(12\omega t - 180)] = 0 \quad (4.2.24)$$

In the proposed front-end, the phase shift angle is selected as $\theta = \pm 30°(2n-1)$. It cancels out the most significant harmonic content (6^{th} harmonic) and it also eliminates 18^{th} harmonic current. To validate the concept of capacitor ripple reduction by changing the phase shift angle, MATLAB simulation is performed and provided in Fig. 4-6.

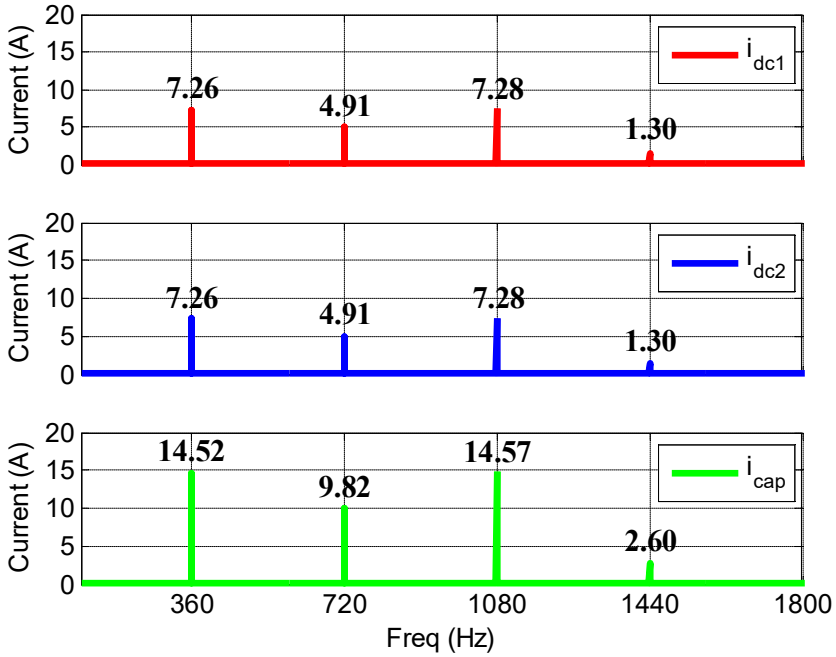
Current (A)
20
15
10
5
0
7.26
4.91
7.28
1.30
i dc1
Current (A)
7.26
4.91
7.28
1.30
i dc2
Current (A)
14.52
9.82
14.57
2.60
i cap
360
720
1080
1440
1800
Freq (Hz)

(a)

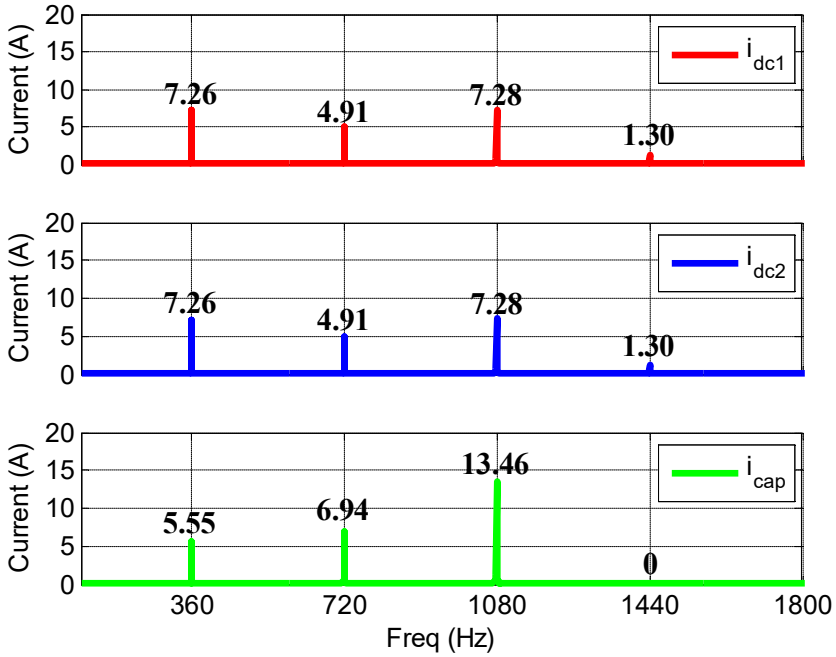
Current (A)
20
15
10
5
0
7.26
4.91
7.28
1.30
i dc1
Current (A)
7.26
4.91
7.28
1.30
i dc2
Current (A)
5.55
6.94
13.46
0
i cap
360
720
1080
1440
1800
Freq (Hz)

(b)

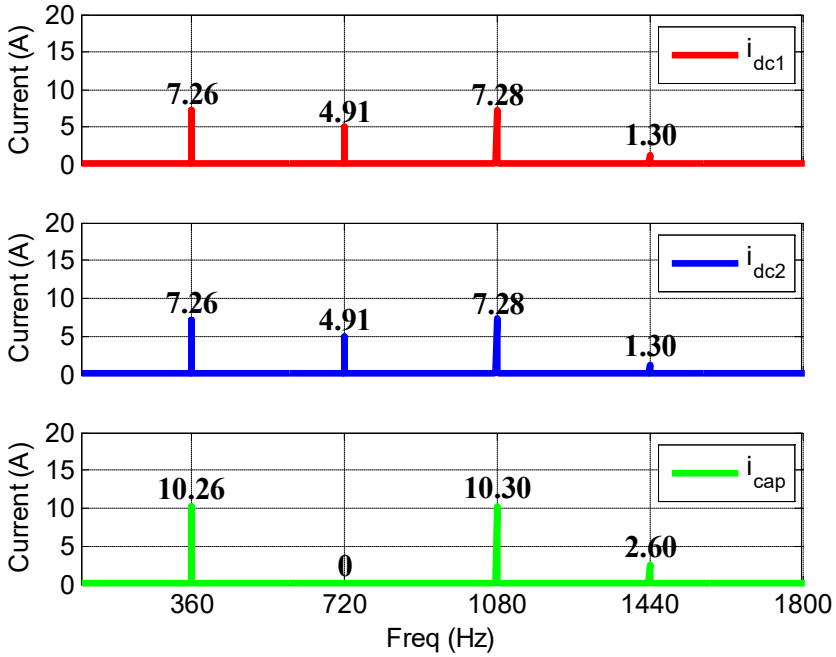

(c)

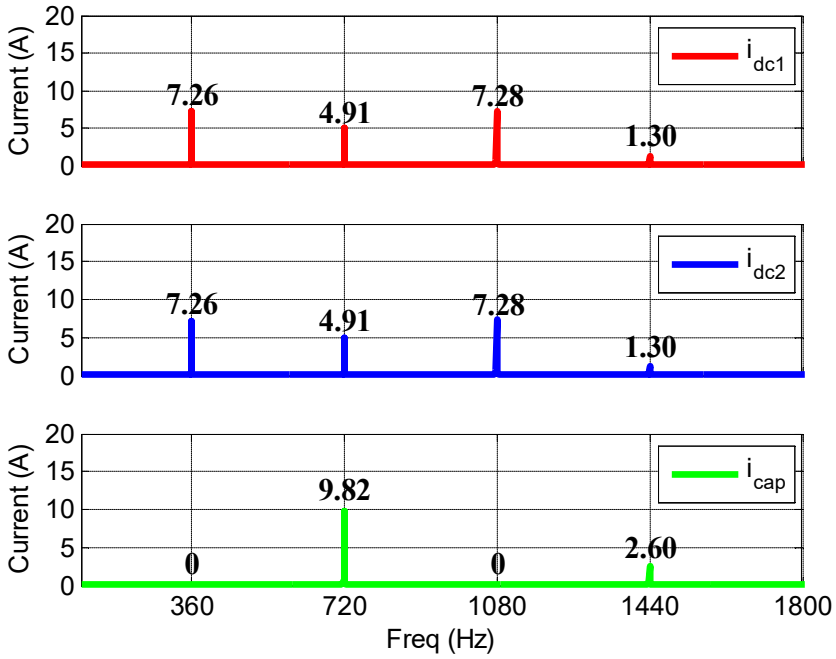

(d)

Fig. 4-6. The frequency sprctra of i_{dc1}, i_{dc2} and i_{cap} when (a) $\theta = \mathbf{0}°$ (b) $\theta = \mathbf{7.5}°$ (c) $\theta = \mathbf{15}°$ (d) $\theta = \mathbf{30}°$

Table 4-2 summarizes the magnitude of harmonic components from MATLAB simulation. When θ = 0°, all the harmonic components in i_{dc1} and i_{dc2} add up together and simply double these components in i_{cap}. In this configuration, the ripple current reduction is not achieved at all. When θ = 7.5° and θ = 10°, 24th and 12th harmonics are eliminated respectively. The most effective harmonic reduction is achieved when the two gensets have 30° phase shift angle and it will eliminate both 6th and 18th harmonics. The trends shown in Table 4-2 agree with the analytical derivation provided in (4.1.13).

Table 4-2. Capacitor current harmonic components in different phase shift angles

	$\lvert i_{cap,6th} \rvert$ [A]	$\lvert i_{cap,12th} \rvert$ [A]	$\lvert i_{cap,18th} \rvert$ [A]	$\lvert i_{cap,24th} \rvert$ [A]
$\theta = 0°$	14.52	9.82	14.57	2.6
$\theta = 7.5°$	5.55	6.94	13.46	**0**
$\theta = 10°$	10.26	**0**	10.30	2.6
$\theta = 30°$	**0**	9.82	**0**	2.6

4.3 Controller Design

The controller design for the back to back APF is similar to hybrid APF. In hybrid APF, the shunt transformer handles of $6k \pm 1$ (k = 1, 3, 5, ···) harmonics and therefore, only 11th and 13th are selectively eliminated by APF. In contrast, the harmonic compensation in back to back APF is not limited to 11th and 13th harmonics. The back to back APF has to eliminate all the frequency components other than fundamental and the harmonic cancellation performance is limited by control loop bandwidth. The overall control loop for APF1 is shown in Fig. 4-7. The harmonic reference generator, which provides the reference currents in dq-axis is described in Fig. 4-8.

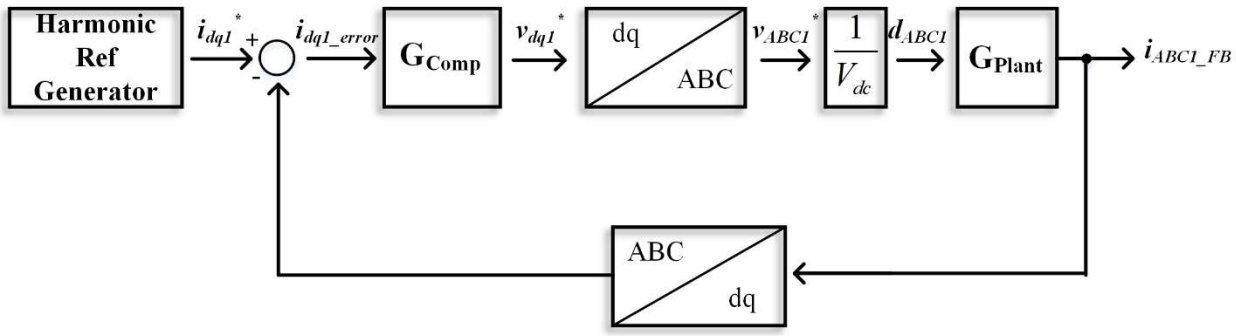

Fig. 4-7. Control block diagram of APF1

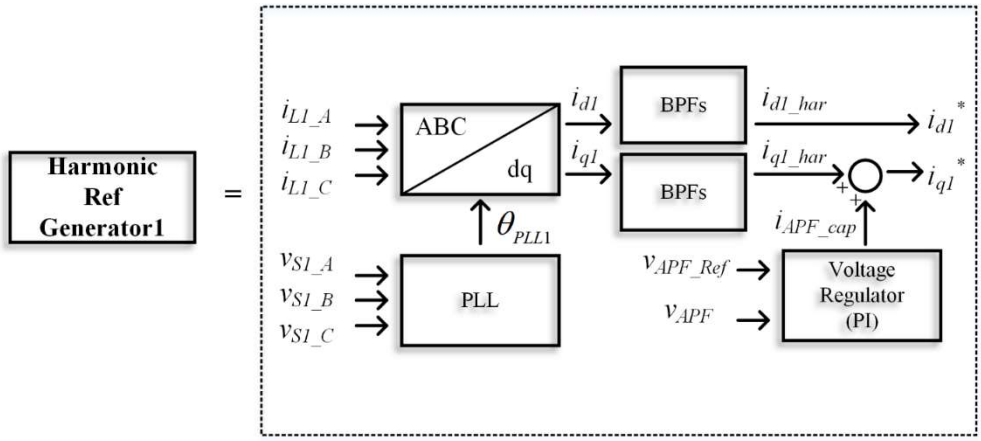

Fig. 4-8. Block diagram of harmonic reference generator

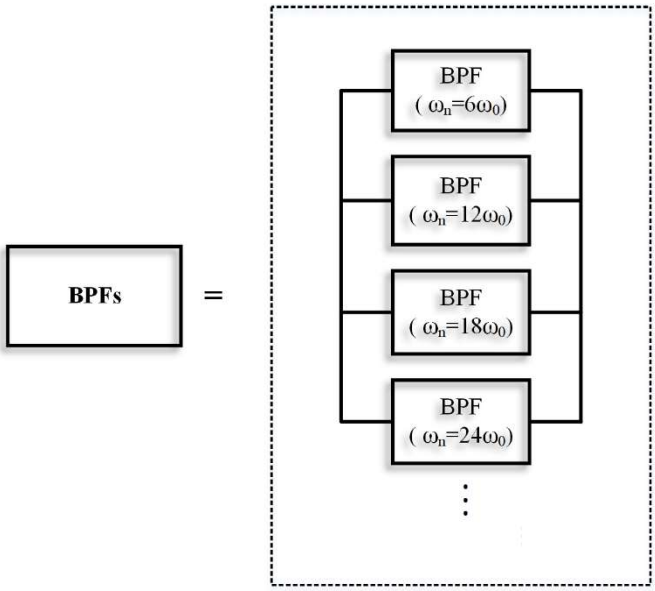

Fig. 4-9. Block diagram of bandpass filters (BPF)

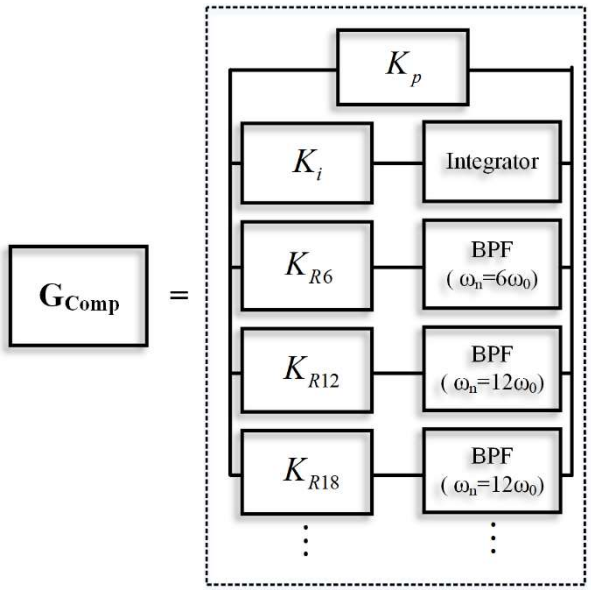

Fig. 4-10 Block diagram of PI+R compensator

Bandpass filter (BPF) blocks and PI+R compensator are presented in Fig. 4-9 and Fig. 4-10 respectively. The harmonic reference generator provides the current reference for APF1. The load currents i_{L1_ABC} are transformed into dq axis i_{dq1} and bandpass filters extract harmonics. As discussed in Chapter 3, the practical bandpass filters (3.2.12) are implemented in both simulation and experimental set up to avoid the instability issue from infinite gain. In addition to harmonic components, dc component from voltage compensator is added in the q-axis for dc-link capacitor voltage control. PI+R compensator has to provide sufficient gain at dc and all the $h = 6k \pm 1$ (k = 1, 3, 5, ···) harmonics.

The control loop for APF2 is the same as the control loop for APF1. As back to back APF shares the same dc bus, it only requires one dc-link voltage compensator. To avoid the redundancy and save resources, the dc-link voltage compensator is not included in the control loop of APF2. Other than the voltage compensation, the two control loops are identical.

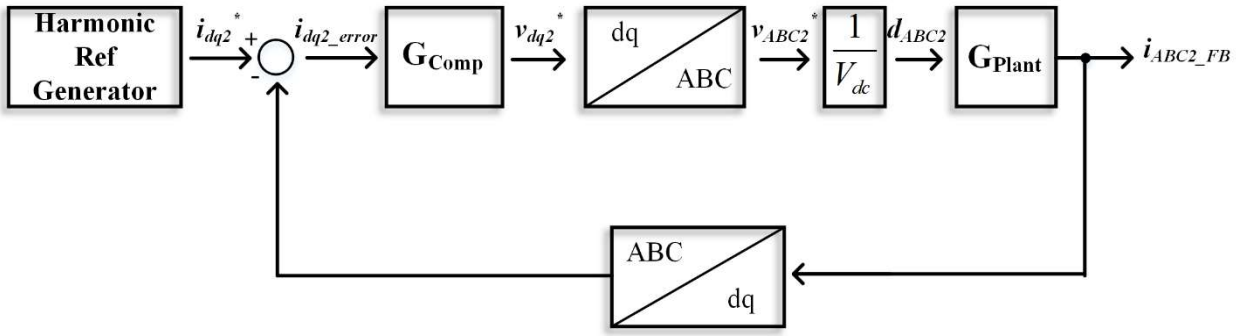

Fig. 4-11. Control block diagram of APF2

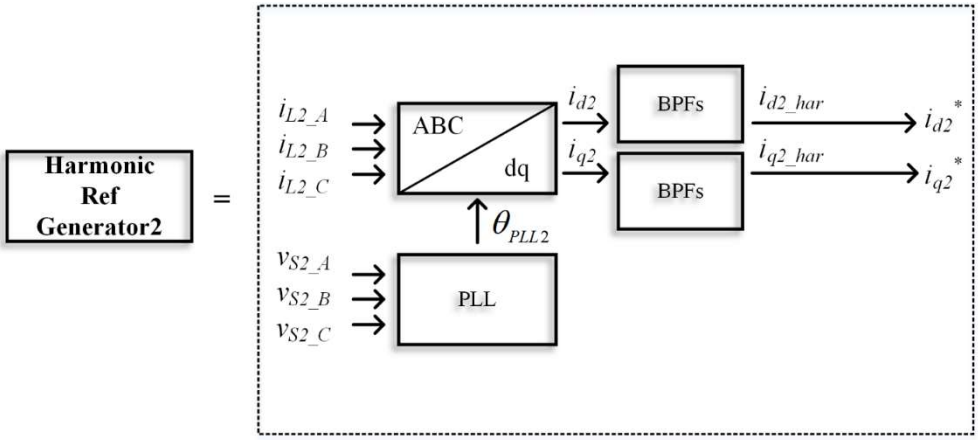

Fig. 4-12. Block diagram of harmonic reference generator

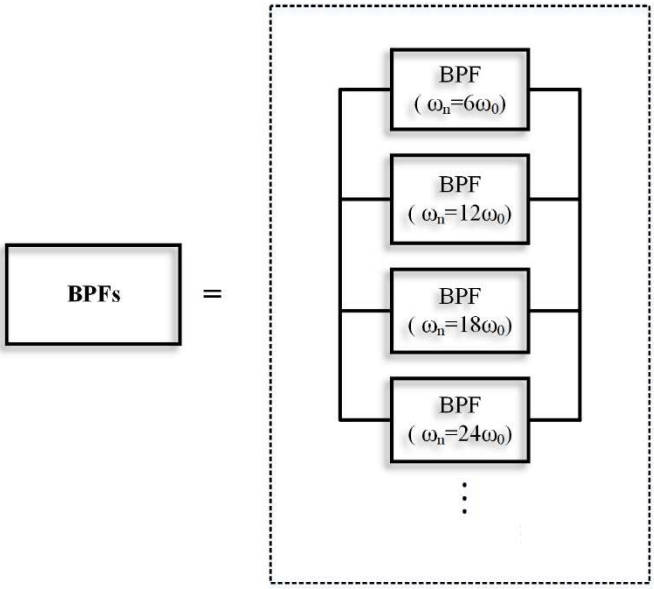

Fig. 4-13. Block diagram of bandpass filters (BPF)

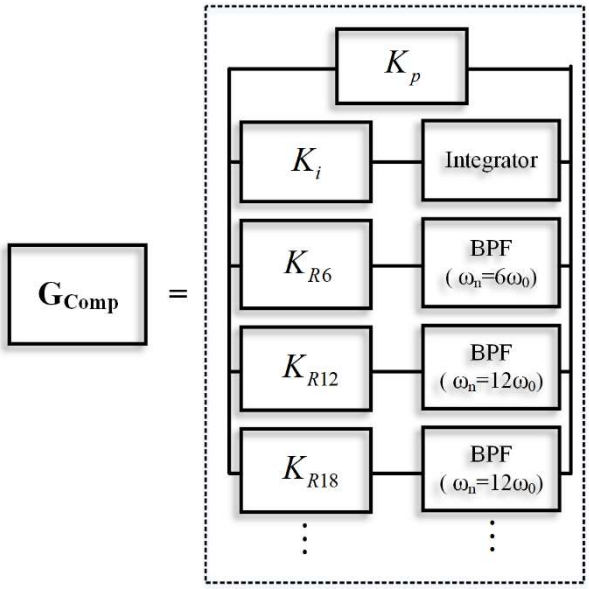

Fig. 4-14. Block diagram of PI+R compensator

The PI+R compensator design is the same as the compensator design for hybrid front-end. K_p and K_i are designed from the pole-zero cancellation method with the desired cross over frequency. Once PI compensator is designed and the desired gain at the frequency of interest is determined, the resonant gain can be calculated.

The loop gain is shown in Fig.4-15. It provides a sufficient gain at dc and more than 40 dB gain for harmonic components. The phase margin is 52.5 ° and the system is stable including the digital delay. Compared to the PI+R compensator in hybrid front-end, the phase margin is decreased by 17°. This is affected by two reasons. First of all, the sampling frequency has to be lowered in back to back APF because another 3 phase inverter control loop and harmonic detection algorithm requires dsp cycle budget. To accommodate additional computation, the sampling frequency has to be lowered and at 40 kHz sampling frequency, dsp budget cycle is below 70 %. Second, the additional bandpass filter affects the phase margin too. At the resonant frequency, the phase changes from + 90° to - 90° by a bandpass filter and the bandwidth f_c determines the rate of

change. It is better to have a smaller bandwidth to minimize the impact on the phase margin but again, it may lead a stability issue. Therefore, fc has to be carefully selected especially when the resonance frequency of the bandpass filter close to the cross over frequency. In this design, bandpass filters higher than 24th harmonics are not included due to stability issue. Also, these harmonics are so small that does not severely impact THD.

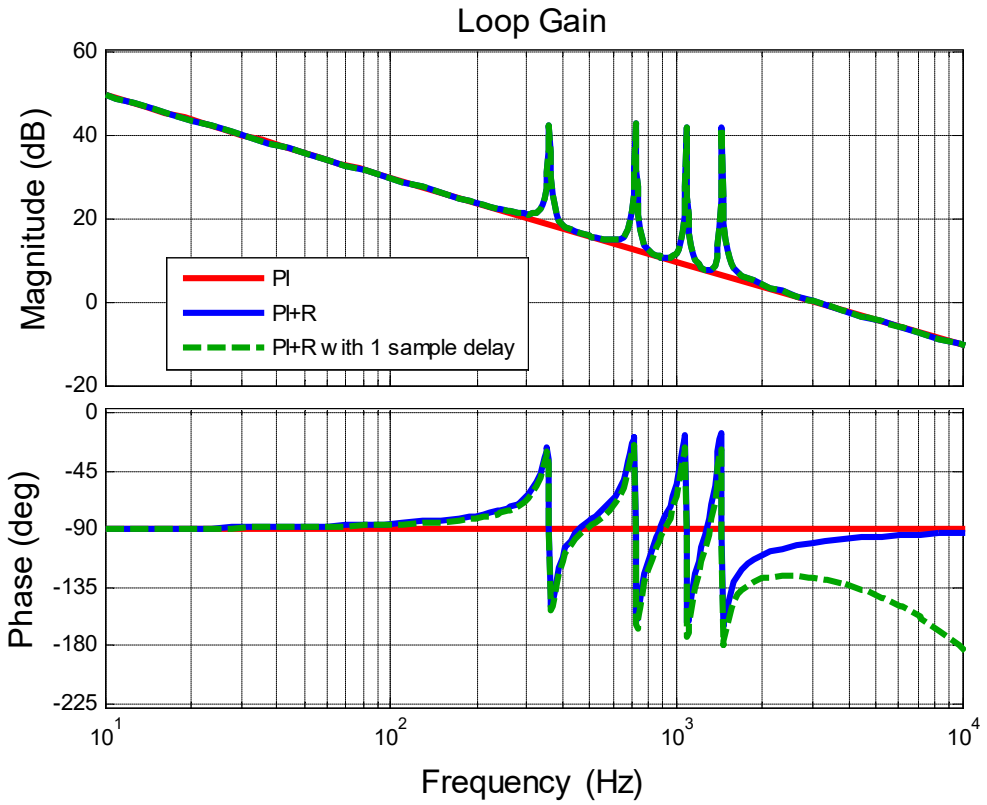

Fig. 4-15. The loop gain of PI, PI+R, and PI+R with digital delay

4.4 Simulation

PSIM simulation was performed to validate the concept of back to back APF. Also, the performance of back to back APF is compared with shunt passive and shunt hybrid front-end in

Fig.4-16. The control parameters are summarized in Table 4-3. All the resonant gains are designed to achieve 40 dB gain at the individual resonant frequency. Table 4-4 shows the simulation conditions.

Table 4-3. Control parameters

Symbol	Parameters	Value
L	APF inductance	0.7 mH
R	APF resistance	0.01 Ω
f_{CC}	Cross over frequency	3 kHz
f_{SW}	Switching frequency	20 kHz
f_{Samp}	Sampling frequency	40 kHz
K_P	Proportional gain	14.14
K_I	Integral gain	188.5
K_{R6}	Resonant filter gain at 300 Hz	200
K_{R12}	Resonant filter gain at 720 Hz	450
K_{R18}	Resonant filter gain at 1080 Hz	600
K_{R24}	Resonant filter gain at 1440 Hz	800

Table 4-4. Simulation specification

Symbol	Parameters	Value
V_{S1}	The line to line voltage of genset1	100 V
V_{S2}	The line to line voltage of genset2	100 V
θ_{S1}	The phase angle of source current 1	0°
θ_{S1}	The phase angle of source current2	0°, 15°, 30°
R_{load}	Load resistance	4
C_{dc}	dc-link capacitance	4.4 mF
L_S	Source inductance	1.5 mH
L_{leak}	Transformer leakage inductance	0.15 mH
L_{APF}	APF inductance	1.5 mF
C_{APF}	APF dc-link capacitance	300 uF
V_{APF}	APF dc-link voltage	150

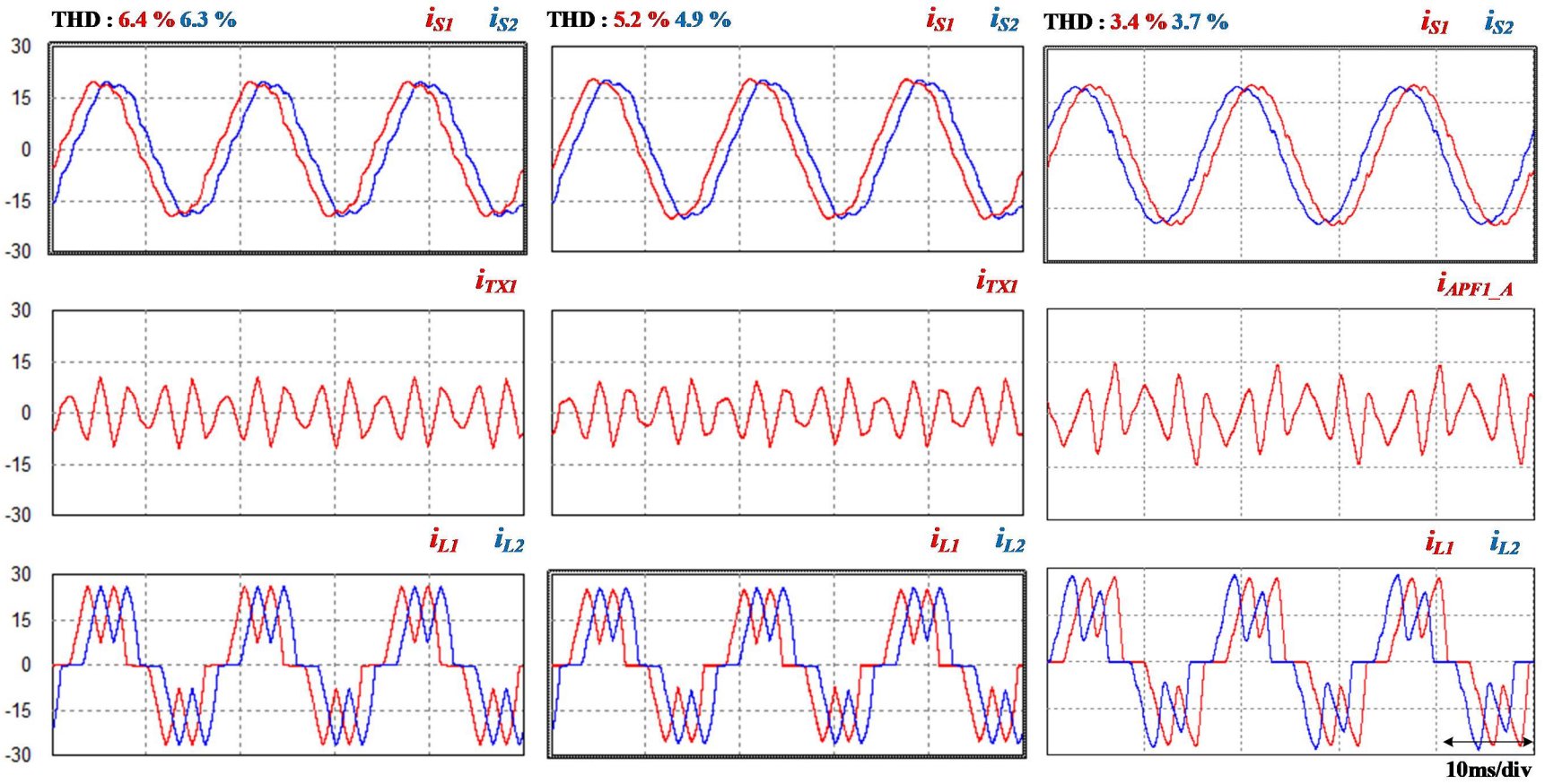

Fig. 4-16. Time-domain waveform of source, APF, load currents (a) passive shunt front-end (b) hybrid shunt front-end (c) Back to back active front-end

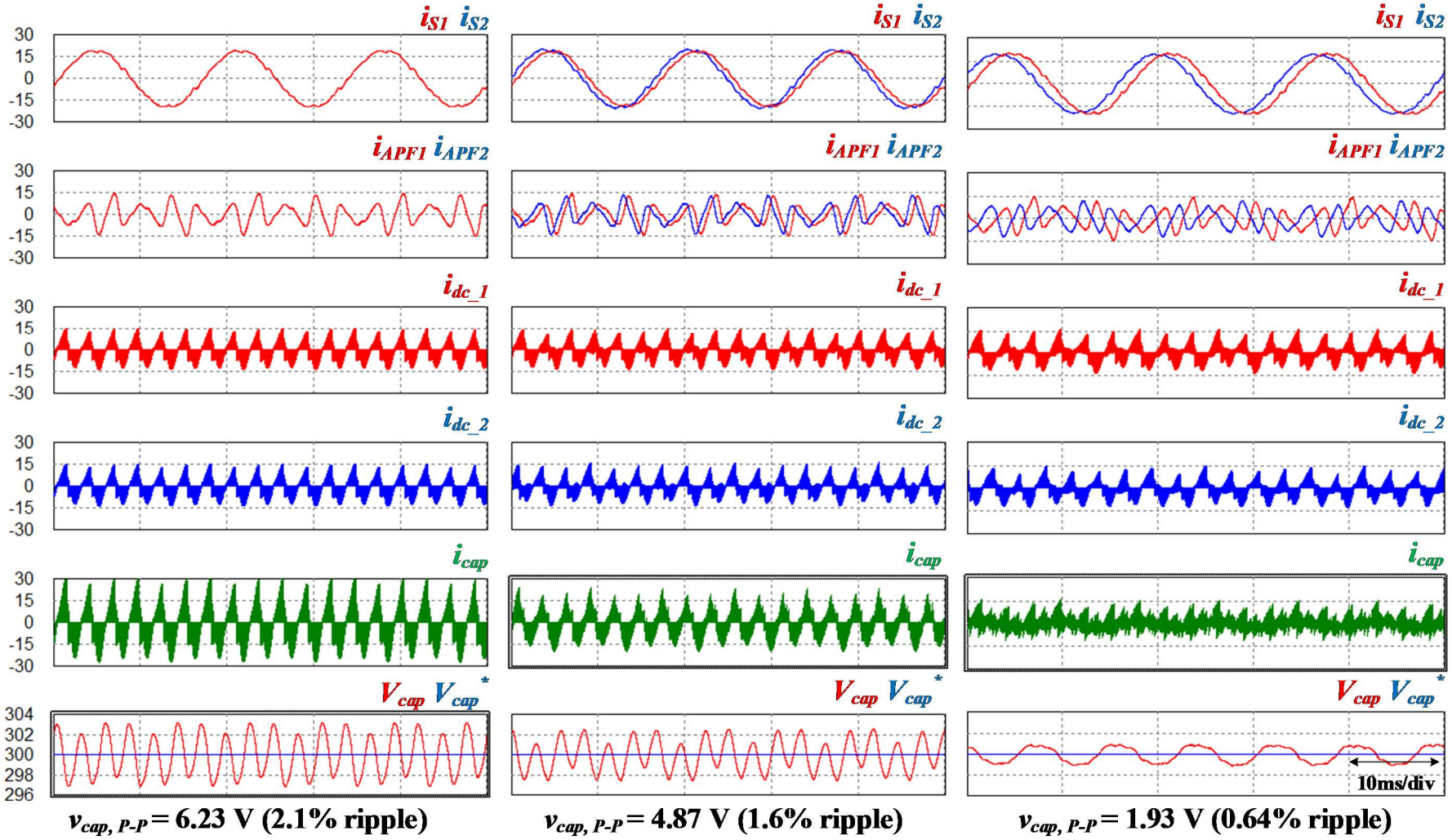

Fig. 4-17. Time domain waveform of source, APF, load currents, capacitor current and voltage (a) $\theta = 0°$ (b) $\theta = 15°$ (c) $\theta = 30°$

All the passive front-end shows a significant harmonic current reduction. In terms of THD, back to back APF shows the lowest number. This is mainly because it will effectively eliminate harmonics up to 1440 Hz. In addition to the harmonic cancellation performance, the back to back APF has to reduce the dc voltage ripple by adjusting the phase-shift angle. The simulation results shown in Fig.4-17 show the waveforms of back to back APF in different phase-shift angles. Regardless of the phase-shift angle, back to back APF provides excellent harmonic cancellation performance. The key part is the capacitor voltage V_{cap} waveforms. The voltage ripple is significantly changed by adjusting the phase-shift angle. Compared to 0° condition, the voltage ripple is reduced by more than 70 % under 30° phase-shift condition. In other words, the required size of dc-link capacitor can be reduced by 70%. The simulation results are summarized in Fig.4-17.

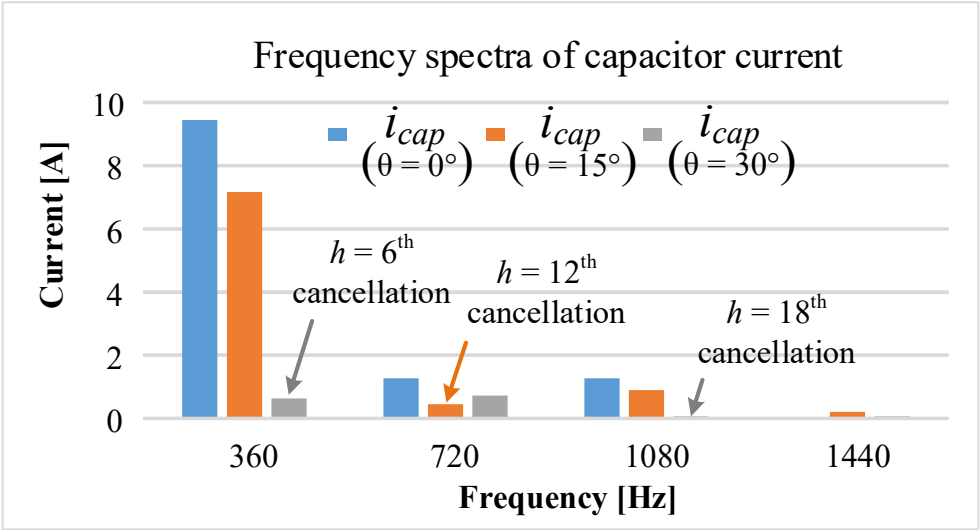

(a)

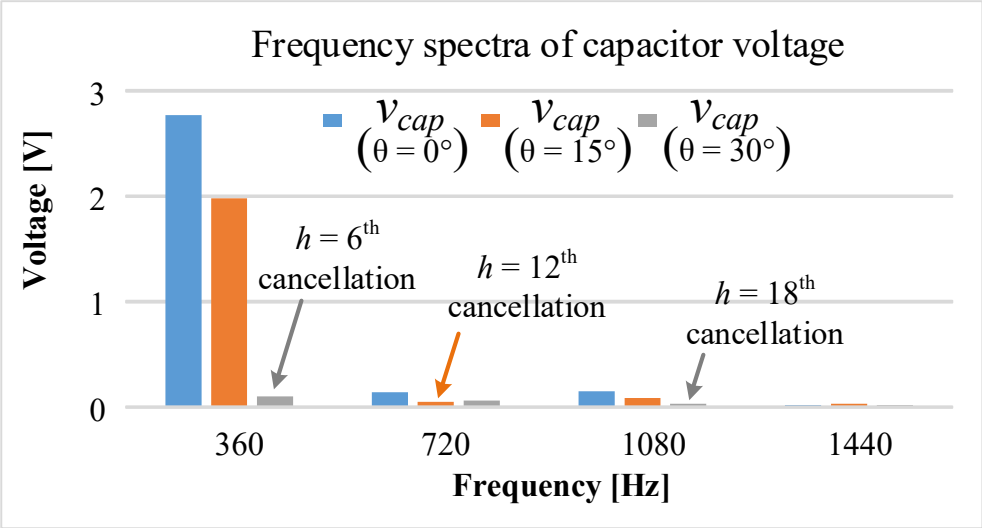

(b)

Fig. 4-18. . The frequency spectra of (a) capacitor voltage and (b) capacitor voltage

4.5 Experimental test results

The digital implementation of back to back APF with multi-genset power architecture requires multiple PWM signals and ADC channels to run the whole system. The system includes 2 VSIs for the source side and another 2 VSIs in front-end. Therefore, 24 PWM signal output is required to drive the whole 3-phase inverters.

Referred to Fig.4-19, 3 current sensors are required for each side to extract harmonics. Under the balanced condition, only 2 current sensors can be utilized but the test setup is not guaranteed to be balanced all time. Additionally, each APF needs 3 current sensors for closed-loop current control. 2 sensors may enough for the balanced condition but 3 sensors are installed for the best performance. One voltage sensor is required for dc-link capacitor voltage control. Overall, 13 ADC channels needed.

The phase-locked loop (PLL) may require 6 more voltage sensors for the phase detection of VSIs in the source side. To avoid additional sensors, the whole system is driven by a single control board. In a single board operation system, the phase angles of 3 phase inverters are

generated by internal ramp function provided by dsp and therefore, it does not requires an extra PLL for synchronization.

The control board was designed to fulfill all the required ADC channels and PWM outputs. TMS320F28377D from Texas Instruments was selected for its powerful computing power and ample peripherals. It has a dual-core processor (200 Mhz) and provides up to 24 PWM outputs and 20 ADC channels.

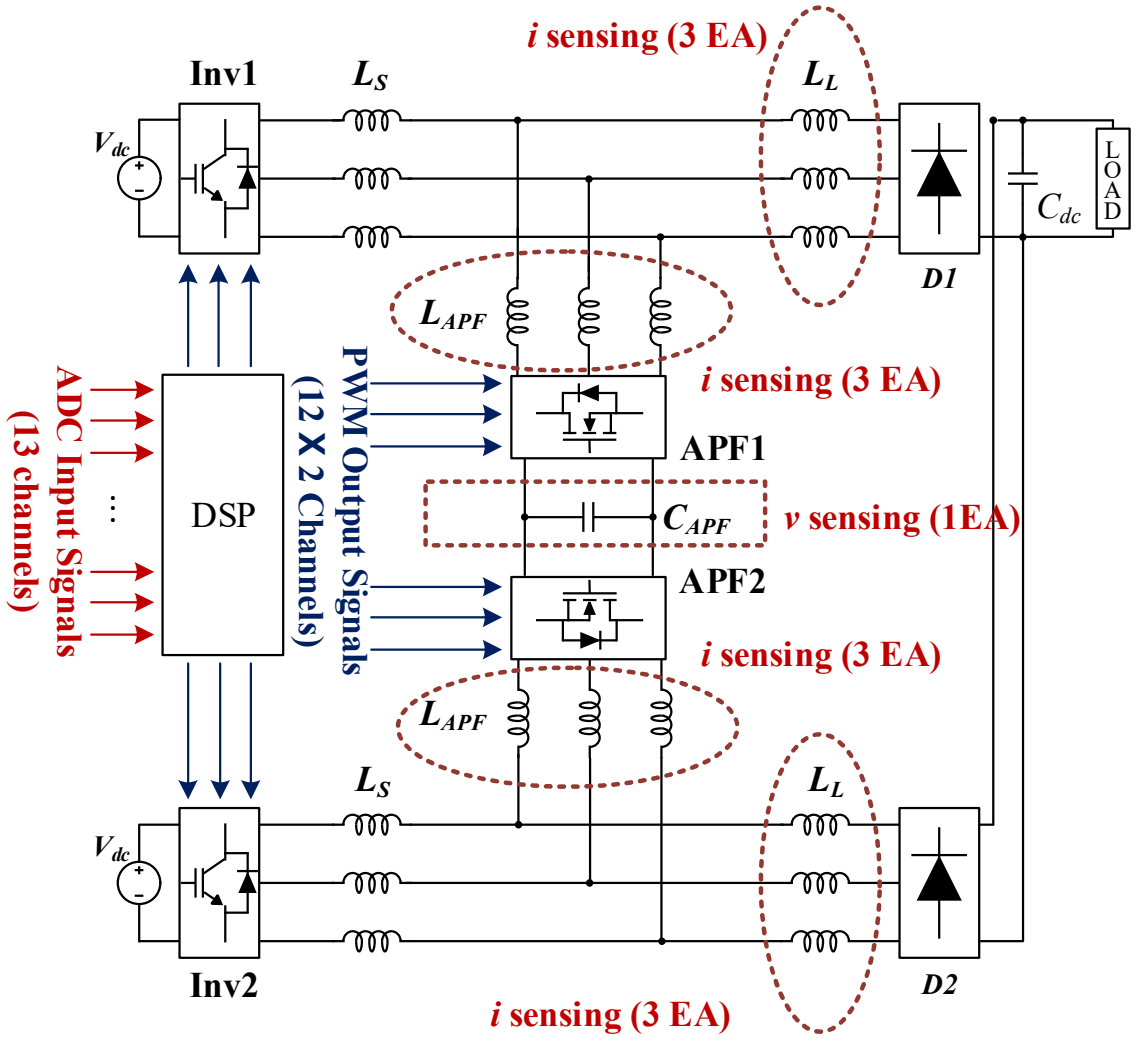

Fig. 4-19. The circuit diagram and the location of current and voltage sensors

The key components of the system are provided in Table 4-5. 2 IGBT modules are used for 2 VSIs in the source side and SiC MOSFETs are utilized for back to back AFP. As the APF was originally designed for the actual shipboard power system where ac mains are 690 V, the voltage and current ratings for power devices are more than enough for the lab test environment (70V).

Table 4-5
The key component for the prototype hardware

Model	Manufacturer	Feature	Specification
TMS320F28377D	TI	Dual core DSP	24 ADC channel 24 PWM outputs
FSBB30CH60D	Onsemi	IGBT Module (INV1, 2)	600 V, 30A
SCT3022KL	ROHM	SiC MOSFET (APF1, 2)	1200 V, 95 A
LA-55 P	LEM	Current Sensor	Current measurement range :50 A
LV-25 P	LEM	Voltage Sensor	Voltage measurement range :500 V

4.5.1 Hardware Design

The control board was designed for the prototype system and shown in Fig. 4-20. The design goal was to accommodate enough peripherals (24 PWM channels, 13 ADC channels, and 4 DAC outputs) in the compact size. As the new board runs 13 ADC at the same time, 15 V power supply had to be carefully selected to supply enough power to transducers.

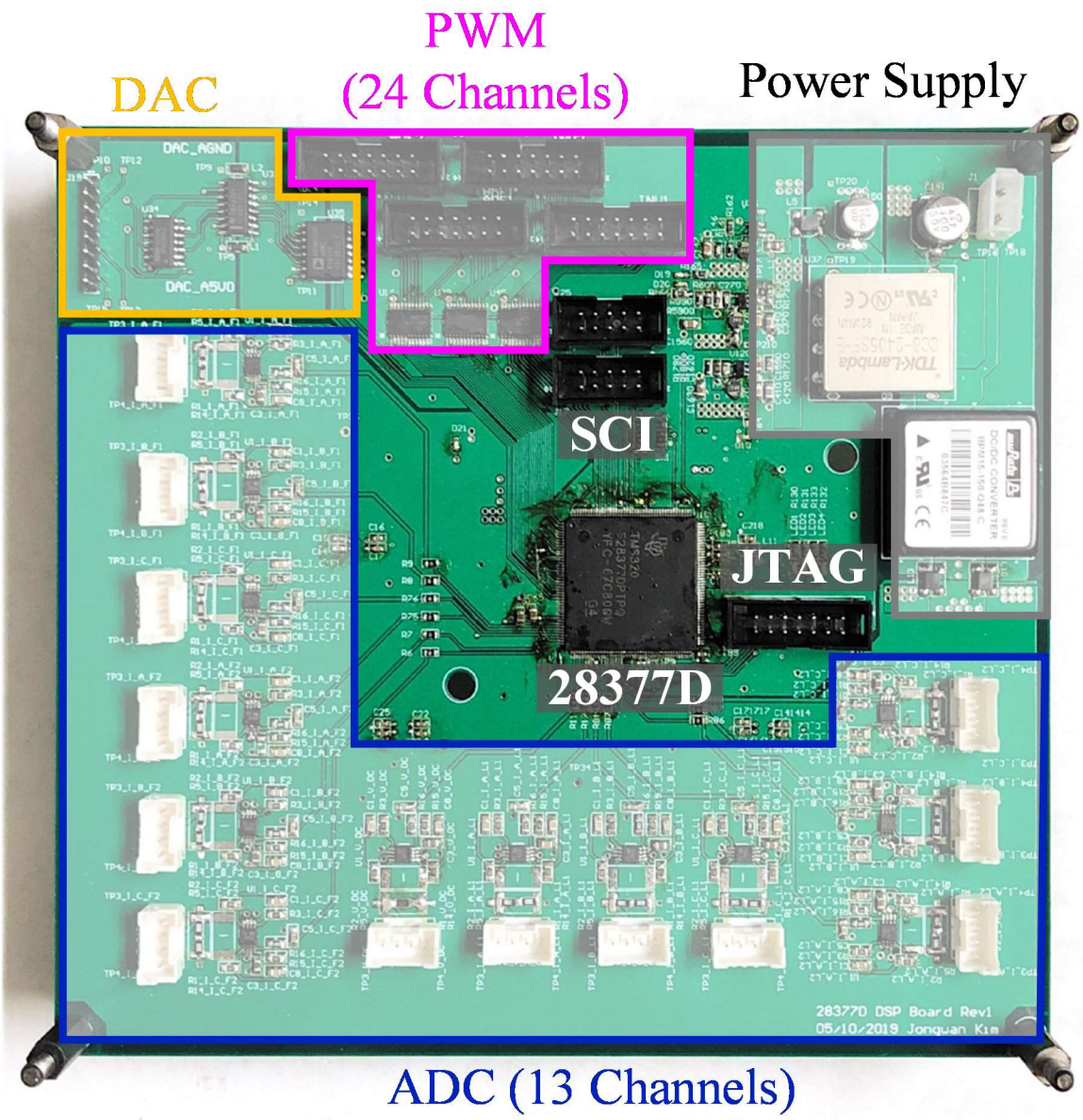

Fig. 4-20. Control board hardware design

The back to back APF is shown in Fig. 4-21. Two 3 phase VSIs are stacked together to minimize the space for the installation. The experimental set up follows the circuit diagram shown in Fig.4-19 and the simulation specification shown in Table 4-4. The prototype hardware set up is presented in Fig. 4-22.

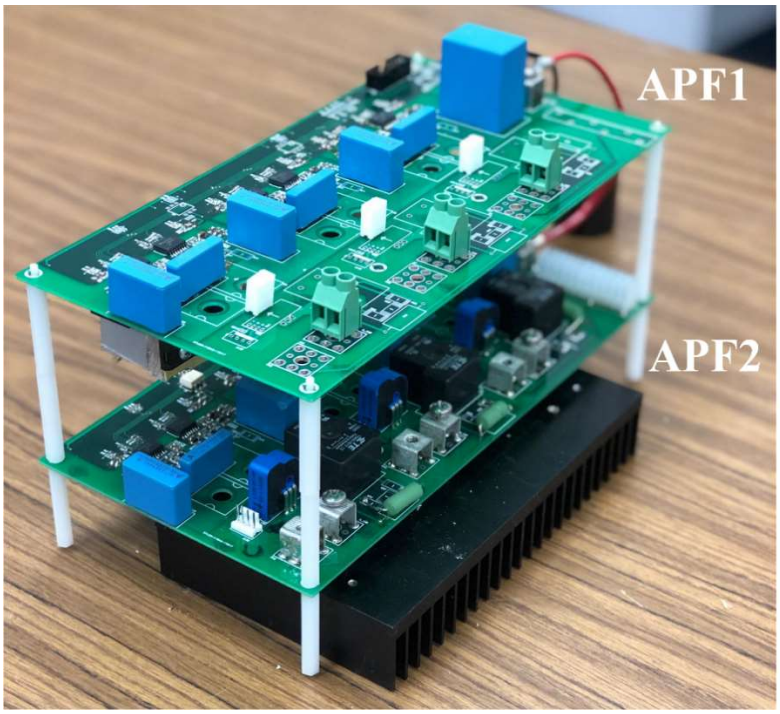

Fig. 4-21. Back to back APF hardware design

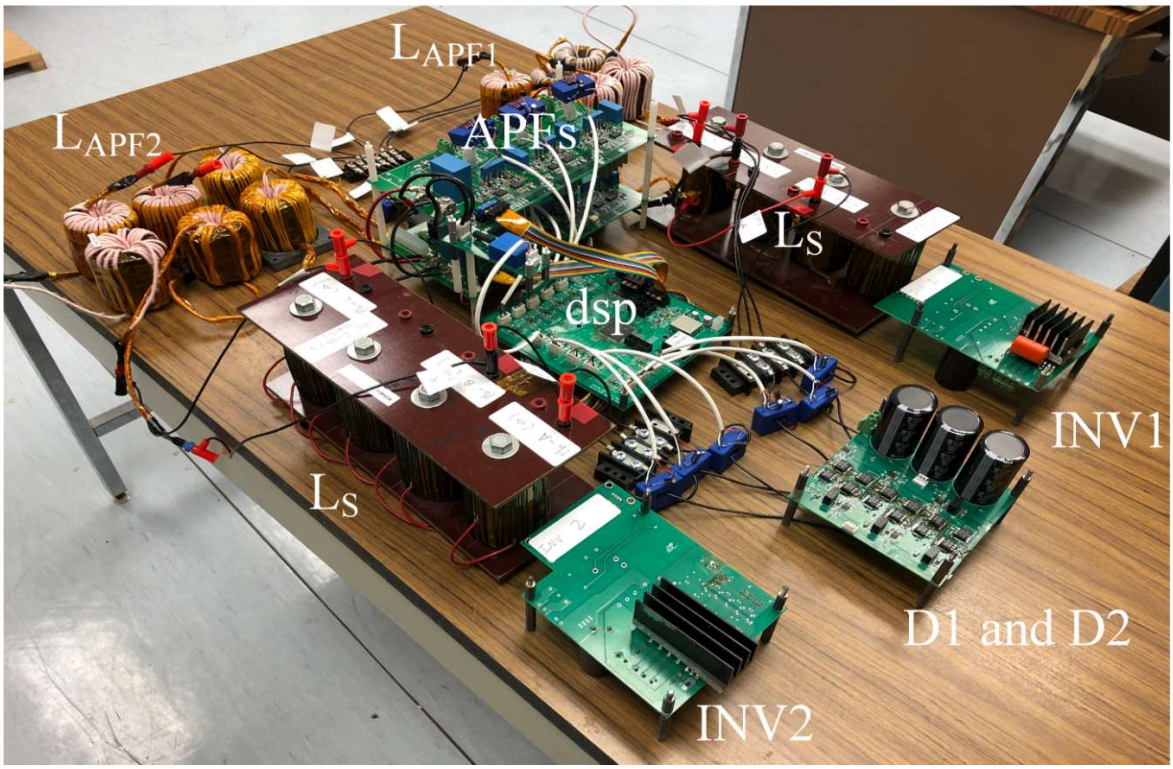

Fig. 4-22. Proto-type hardware setup for back to back APF

4.5.2 Bandpass filter digital implementation

The digital implementation of bandpass filter stars from the transfer function in Laplace domain.

$$G_{BPF}(s) = \frac{2\omega_c s}{s^2 + 2\omega_c s + \omega^2} \tag{4.5.1}$$

By Tustin approximation, G_{BPF} can be represented in Z-domain

$$G_{BPF}(z) = \frac{4\omega_c T_s (z^2 - 1)}{[4 + 4\omega_c T_s + (\omega T_s)^2]z^2 + [2(\omega T_s)^2 - 8]z + [4 - 4\omega_c T_s + (\omega T_s)^2]} \quad . \tag{4.5.2}$$

For derivation purpose, let define $den = 4 + 4\omega_c T_s + (\omega_c T_s)^2$ and re-write the transfer function as

$$\begin{aligned} G_{BPF}(z) &= \frac{\frac{4\omega_c T_s}{den}(z^2 - 1)}{z^2 + \frac{[2(\omega T_s)^2 - 8]}{den} z + \frac{[4 - 4\omega_c T_s + (\omega T_s)^2]}{den}} \\ &= \frac{a_2 + a_0 z^{-2}}{b_2 + b_1 z^{-1} + b_0 z^{-2}} \\ &= \frac{y(z)}{u(z)} \end{aligned} \tag{4.5.3}$$

From the inverse Z-transform, the difference equation is derived as

$$y(n) = [b_2 u(n) + b_0 u(n-2)] - [a_1 y(n-1) + a_0 y(n-2)] \tag{4.5.4}$$

Where $a_2 = 4\omega_c T_s \times den$, $a_0 = -4\omega_c T_s \times den$, $b_2 = 1$, $b_1 = [2(\omega_c T_s)2 - 8] \times den$, $b_0 = [4 - 4\omega_c T_s + (\omega_c T_s)^2]$. These coefficients are plugged into dsp to implement a digital BPF. The time-domain waveforms of implemented BPF is shown in Figs. 4-23. The bandwidth f_c is set to 10 Hz in this example.

In Fig. 4-23 (a), the input ($u(t)$) is the summation of the fundamental and 6th harmonic and the BPF with 360 Hz (6th harmonic) resonant frequency extracts only 6th harmonic component and filter out the fundamental component. The output of BPF y(t) only shows the 6th harmonic component. The waveform with 720 Hz harmonic component and BPF at 720 Hz resonant frequency is provided in Fig. 4-23 (b). Again, BPF output only contains 12th harmonic component.

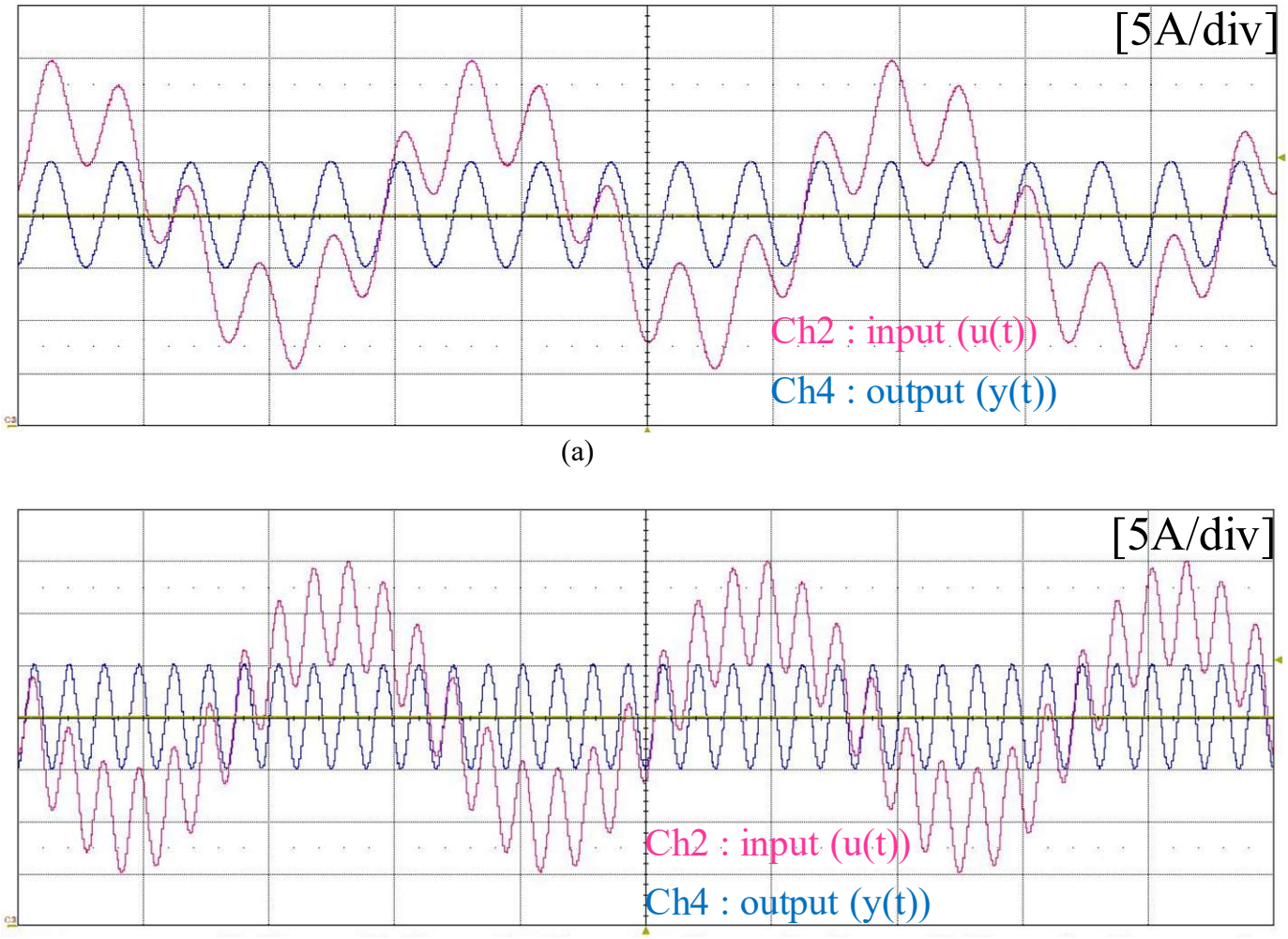

Fig. 4-23. The time-domain waveform of input and output of BPF (a) u(t) = sin(ωt) + sin(6ωt) (b) u(t) = sin(ωt) + sin(12ωt)

4.5.3 Test Waveforms

Fig. 4-24 gives the source current i_{S1} and i_{S2} waveforms without the front-end. Due to the diode rectifier and capacitor charging and discharging current, it draws highly non-linear current and significantly impacts on ac mains. The total harmonic distortion (THD) of i_{S1} and i_{S2} is 22.84% and 21.74% respectively and it is not acceptable.

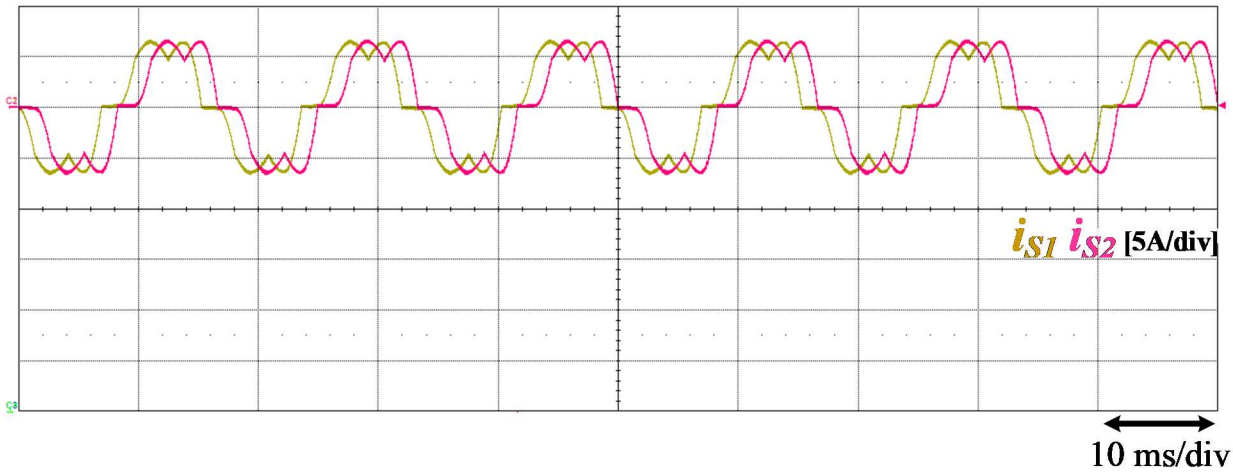

Fig. 4-24. Source currents i_{S1}, i_{S2} waveforms without front-end

To validate the harmonic cancellation performance and the impact of the proposed front-end, source current waveforms with back to back APF are presented in Fig. 4-25. The phase shift angle θ between two gensets is 0°. The active power filter current i_{APF1} provides most of the harmonic components drawn by non-linear load and the source current becomes more sinusoidal compared to the waveforms without front-end. THD of i_{S1} and i_{S2} are 3.10 % and 3.12 % respectively. The average dc-link capacitor voltage is regulated at 120 V and clearly shows that 6^{th} harmonic component in the waveform.

The waveforms under 30° phase shift condition are provided in Fig.4-26. Back to back APF effectively eliminate harmonics and THD of i_{S1} and i_{S2} are 3.14% and 3.06% individually.

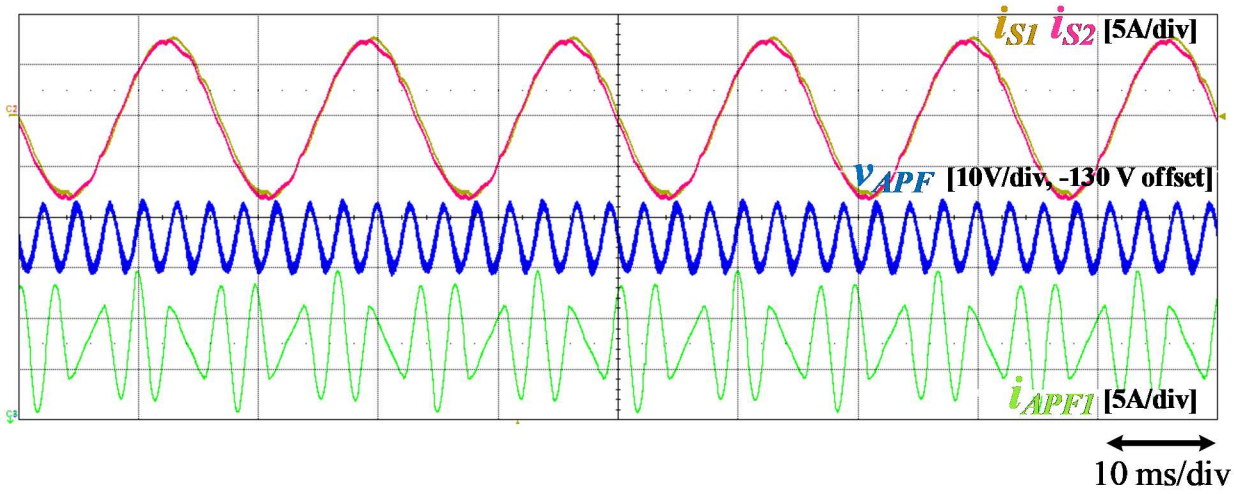

Fig. 4-25. Source currents i_{S1}, i_{S2} waveforms with back to back front-end ($\theta = 0°$)

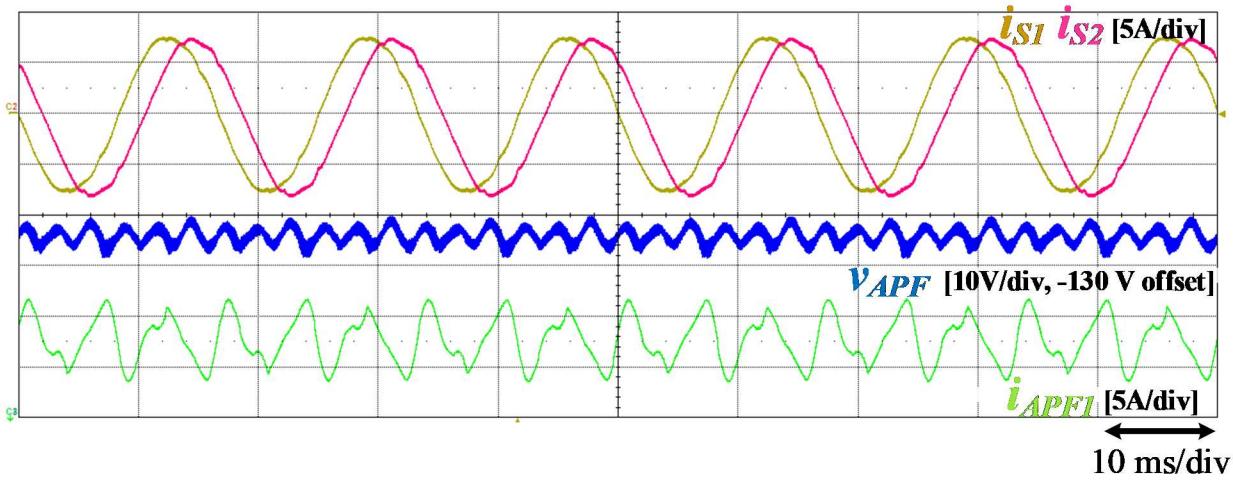

Fig. 4-26. Source currents i_{S1}, i_{S2} waveforms with back to back front-end ($\theta = 30°$)

Fig. 4-27 and shows the amount of harmonic components in the source current. The shunt phase-shift transformer rectifier shows the harmonic reduction in 5th and 7th component but 11th and 13th harmonics can not be eliminated by harmonic cancellation principle. Hybrid front-end further eliminates 11th and 13th harmonics on top of the shunt phase-shift transformer rectifier. The back to back active front-end shows the best performance among all frequencies. Fig.4-28

provides THD under different load conditions. Again, the active front-end shows the lowest THD regardless of the amount of load. The comparison results are recapped in Table 4-6 and 4-7.

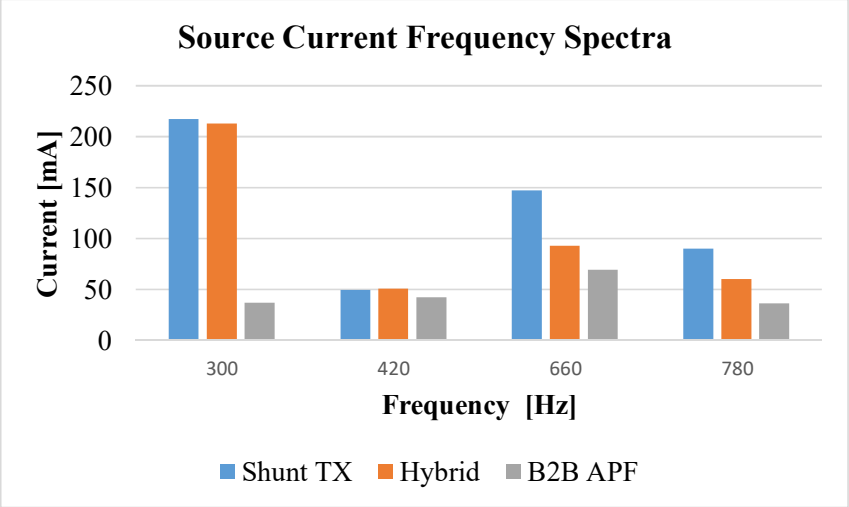

Fig. 4-27 Frequency spectra of source currents in different front-ends

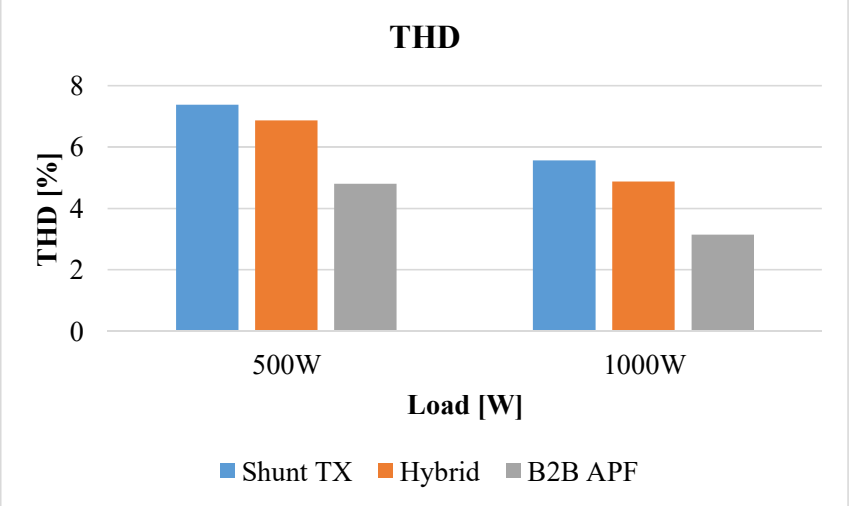

Fig. 4-28 THD of source current in different front-ends

Table 4-6. The magnitude of harmonic components in different front-ends

	Current [mA]		
	Passive front-end	**Hybrid front-end**	**B2B APF**
300 Hz	217.3	212.93	36.96
420 Hz	49.51	50.64	42.09
620 Hz	147	93	69
780 Hz	90	60	36

Table 4-7. THD of source current in different front-ends

	THD [%]		
	Passive front-end	**Hybrid front-end**	**B2B APF**
500W	7.37	6.87	4.8
1000 W	5.56	4.87	3.14

4.6 Summary

Back to back APF was proposed and the analytical derivation was provided to explain the concept of the proposed front-end. The comparison between shunt phase-shift transformer, hybrid front-end, and back to back APF showed that the performance of back to back APF is far superior to the passive and hybrid front-end. This is mainly because the impedance of harmonic conduction path provided by back to back APF is much lower than that of the shunt phase-shift transformer. Therefore, the proposed front-end achieves excellent harmonic cancellation performance without a huge line reactor in ac mains.

The impact of the phase shift angle on the capacitor voltage ripple has to be highlighted to show the advantage of the proposed front-end. In Fig. 4-29, the phase-shift angle θ is changed from 30° to 0° at t = 50 ms. Regardless of the phase-shift angle, THD is below 5% and the average dc link voltage v_{APF} tracks the reference dc link voltage (120 V). However, the amplitude of peak

to peak voltage changes from 7.11 V ($\theta = 30°$) to 15.62 V ($\theta = 0°$). Also, the amount of harmonics in active power filter current i_{APF1} is significantly increased. In other words, when $\theta = 30°$, the dc-link voltage ripple is reduced by 55% and reduce the burden of active power filter compared to $\theta = 0°$ condition. Considering that the voltage ripple determines the size of the capacitor, back to back APF with 30° phase shift requires relatively small capacitance compares to synchronized back to back configuration or 2 separate APF front-ends.

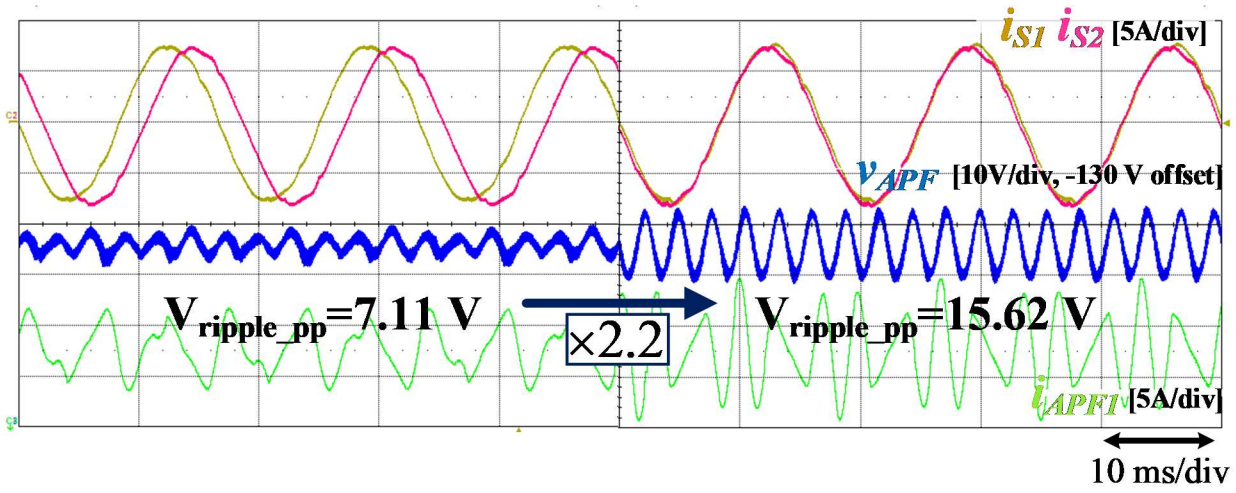

Fig. 4-29. The experimental waveform of back to back APF with dynamically changing the phase shift angle θ at 50 *ms*

In addition to the performance and required capacitor size, the overall volume and weight of the proposed front-end is only a fraction of the shunt phase-shift transformer rectifier.

Fig. 4-30 shows the size comparison between Y-Δ transformer and back to back APF. The dimensions and weight are provided in Table 4-8. Compared to the Y-Δ transformer, back to back APF has much small volume (66% reduction) and weight (96% reduction). The weight of back to back APF is mostly determined by the heat sink and the required heat sink may vary depending on the power rating. The prototype hardware utilizes Y-Δ transformer rated at 4.5 kVA while the power rating for APF is 8 kW. Considering that back to back APF has an even higher power rating,

the advantages of volume and weight are noticeable and extremely attractive to marine transport where installation volume and weight are concerns.

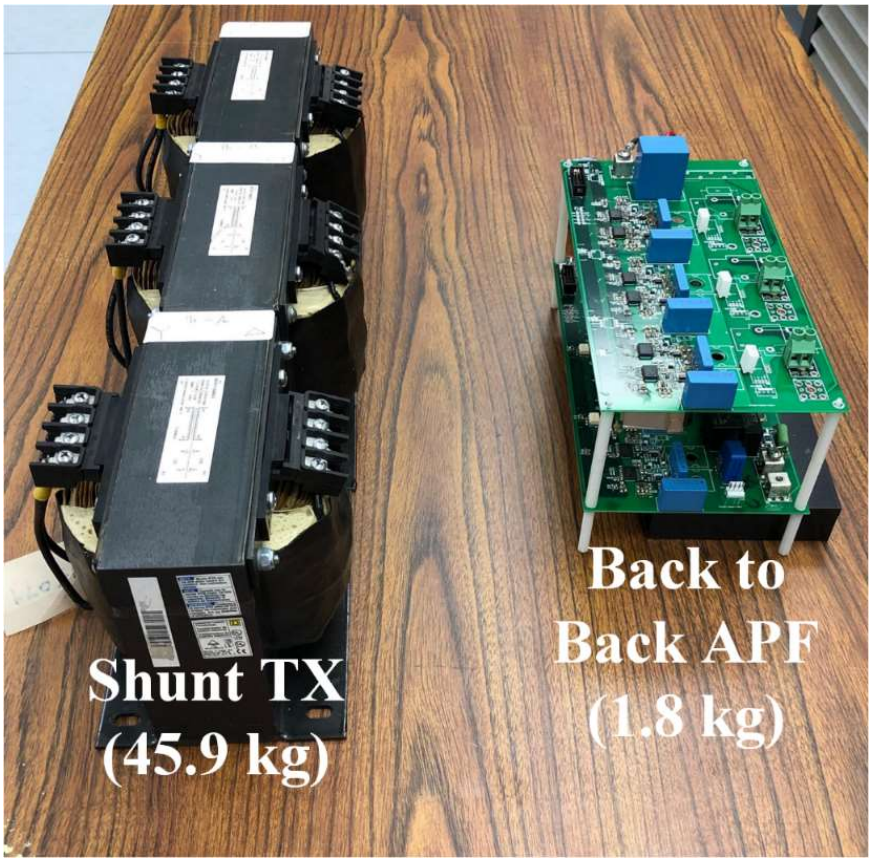

Fig. 4-30. Comparison between Y-Δ transformer and back to back APF

Table 4-8. Dimension and weight comparison

	Height [mm]	Width [mm]	Depth [mm]	Weight [kg]
Y-Δ TX	156.72	537.96	150.37	45.9
B2B APF	120.3	135.9	260.8	1.82

Chapter 5

Conclusion and Future work

In this dissertation, a back to back active front-end for the multi genset power system is proposed. The idea of the proposed font-end is originated from the passive shunt phase-shift transformer rectifier, which utilizes the benefit of the multiple gensets in the shipboard power system.

In Chapter 1, the power architecture of the shipboard power system and the concept of the integrated power system (IPS) is discussed. As a result of the shipboard electrification, ac mains are significantly distorted by the non-linear load (VFDs, SMPSs, and etc) and the system requires a front-end to meet the harmonic regulations such as MIL STD 1399 and IEEE STD 519. The basic concept of 12 pulse converter and the shunt phase-shift transformer rectifier are compared and

The advantages of the shunt type front-end are highlighted in Chapter 2 and a detailed analysis is provided. The key aspect of the shunt phase-shift transformer front-end is the selective harmonic elimination without being involved in the fundamental power flow. Accordingly, the required transformer VA rating is only a fraction of that of 12-pulse converter and the size and weight for the transformer can be significantly reduced. To see the effectiveness of the shunt phase-shift transformer rectifier under the practical operating condition, the behavior of front-end under the non-ideal condition is investigated and verified by analytical analysis, simulation, and prototype hardware. The analysis discovered the origin of the source current unbalance when the phase angle difference of gensets is not at 30° and the impact of the line reactor on the generator side.

Based on the analytical derivation of the shunt phase-shift transformer rectifier, a hybrid shunt front-end is proposed in Chapter 3. By adding a 3-phase shunt active power filter, it further improves the harmonic distortion of ac mains. The equivalent circuit analysis and harmonic cancellation mechanism show that only a single 3 phase active power filter is required for 11^{th} and 13^{th} harmonic elimination in both drive trains. Simulation and test results show that 70% of 11^{th} and 13^{th} harmonic components are eliminated by a single active power filter. Overall, the most significant harmonic component seen from ac mains is pushed to 23^{rd} instead of 11^{th} harmonic component. However, the harmonic conduction path of the hybrid front-end is still determined by the impedance of the transformer branch and therefore, the overall performance is significantly affected by the ratio between the transformer leakage inductance and the source inductance.

Due to the recent advances in wide bandgap devices and microcontrollers, the high-performance active front-end becomes practical and reasonable. To take advantage of the state of the art technologies, two active power filter in back to back configuration is proposed in Chapter 4. It replaces the phase-shift transformer that shunting the two gensets and eliminates all the undesired harmonics. The main advantage of the proposed front-end over the passive and hybrid shunt front-end is the harmonic cancellation performance and size. As the proposed front-end actively compensates the unwanted harmonics, the source impedance dependency is minimized and it provides far superior harmonic cancellation performance. Furthermore, the proposed front-end reduced the overall volume and weight by 66% and 96% respectively by eliminating the bulky phase-shift transformer in the system. This is remarkably beneficial to the shipboard power system in two aspects. First of all, the proposed front-end provides better installation flexibility for the shipboard power system. Secondly, the lightweight front-end contributes to better fuel efficiency. By introducing 30° phase angle difference between the two gensets, the proposed system achieved

55% reduction in voltage ripple in the shared dc link and it will eventually reduce the size of dc-link capacitor.

The comparison between the passive, hybrid, and proposed front-end is shown in Table 5-1. The proposed front-end shows the best performance among the shunt type front-end (below 5% THD) and does not require a bulky phase-shift transformer.

Table 5-1
The comparison between passive, hybrid and back to back active front-end

Topology	**Shunt TX (passive front-end)**	**Shunt TX +APF (hybrid front-end)**	**Back to back APF (active front-end)**
Source inductance	1.5 mH	1.5 mH	1.5 mH
System volume	Bulky	Bulky	Compact
THD	6.4 %	5.2 %	3.5 %
# of required TX	1	1	0
APF inductance	0	0.7 mH	0.7 mH
APF dc link cap	0	800 uF	360 uF
The # of SW device	0	6	12
The # of required sensor	0	6 current sensors 1 voltage sensor	12 current sensors 1 voltage sensor
DSP requirement	No	Yes (Low end)	Yes (High end)

However, the trade-off for the performance and compact size is the requirement of active components for active power filter and voltage and the current sensor for the closed-loop control. Also, back to back APF requires high-end dsp for computationally intensive tasks and ample peripherals.

Given that the importance of the harmonic elimination performance and the front-end size and weight become more and more important, the proposed front-end is a promising option for the future marine transport.

The list of future work is provided below

- The test under the actual shipboard power system has to be followed. Due to the limited resources and safety issues, the line to line voltage of the ac mains and the

load size has to be significantly reduced. The test under the low/medium voltage shipboard power system is necessary to validate the proposed front-end.

- The experimental test under the transient condition has to be investigated. Although the active harmonic cancellation is evaluated under the steady-state condition, it is required to see the behavior of front-end under the transient state to guarantee to fail-safe operation
- Thermal analysis and the actual size and volume evaluation of the proposed front-end under the practical condition.

Reference

[1] Z. Jin, G. Sulligoi, R. Cuzner, L. Meng, J. C. Vasquez, and J. M. Guerrero, "Next-Generation Shipboard DC Power System: Introduction Smart Grid and dc Microgrid Technologies into Maritime Electrical Netowrks," *IEEE Electrification Magazine,* vol. 4, no. 2, pp. 45-57, 2016.

[2] (Nov.8). *New and improved technical solutions from Kongsberg Maritime*. Available: https://hedinn.com/kongsberg-maritime-solutions/

[3] "IEEE Recommended Practice and Requirements for Harmonic Control in Electric Power Systems," *IEEE Std 519-2014 (Revision of IEEE Std 519-1992),* pp. 1-29, 2014.

[4] *ABS Guidance Notes on Control of Harmonics in Electrical Power Systems*, May 2006.

[5] G. E. April and G. Olivier, "A Novel Type of 12-Pulse Converter," *IEEE Transactions on Industry Applications,* vol. IA-21, no. 1, pp. 180-191, 1985.

[6] J.-N. Fiorina, "Static converter with electric valves comprising a twelve-phase connection with two Graetz bridges for the suppression of harmonics 5 and 7 of network current."

[7] McMurray, *Harmonic blocking converter system*. 1995.

[8] D. A Paice, *Power electronic converter harmonics : multipulse methods for clean power / Derek A. Paice*. 1996.

[9] B. Singh, S. Gairola, B. N. Singh, A. Chandra, and K. Al-Haddad, "Multipulse AC–DC Converters for Improving Power Quality: A Review," *IEEE Transactions on Power Electronics,* vol. 23, no. 1, pp. 260-281, 2008.

[10] H. Akagi and K. Isozaki, "A Hybrid Active Filter for a Three-Phase 12-Pulse Diode Rectifier Used as the Front End of a Medium-Voltage Motor Drive," *IEEE Transactions on Power Electronics,* vol. 27, no. 1, pp. 69-77, 2012.

[11] S. Fukuda and I. Hiei, "Auxiliary Supply-Assisted 12-Pulse Phase-Controlled Rectifiers With Reduced Input Current Harmonics," *IEEE Transactions on Industry Applications,* vol. 44, no. 1, pp. 205-212, 2008.

[12] M. S. Hamad, M. I. Masoud, K. H. Ahmed, and B. W. Williams, "A Shunt Active Power Filter for a Medium-Voltage 12-Pulse Current Source Converter Using Open Loop Control Compensation," *IEEE Transactions on Industrial Electronics,* vol. 61, no. 11, pp. 5840-5850, 2014.

[13] M. S. Hamad, M. I. Masoud, and B. W. Williams, "Medium-Voltage 12-Pulse Converter: Output Voltage Harmonic Compensation Using a Series APF," *IEEE Transactions on Industrial Electronics,* vol. 61, no. 1, pp. 43-52, 2014.

[14] M. E. Villablanca, J. I. Nadal, and M. A. Bravo, "A 12-Pulse AC–DC Rectifier With High-Quality Input/Output Waveforms," *IEEE Transactions on Power Electronics,* vol. 22, no. 5, pp. 1875-1881, 2007.

[15] R. Kalpana, K. S. Chethana, P. S. P, and B. Singh, "Power Quality Enhancement Using Current Injection Technique in a Zigzag Configured Autotransformer-Based 12-Pulse Rectifier," *IEEE Transactions on Industry Applications,* vol. 54, no. 5, pp. 5267-5277, 2018.

[16] M. Kang, B. O. Woo, P. Enjeti, and I. J. Pitel, "Autoconnected-electronic-transformer-based multipulse rectifiers for utility interface of power electronic systems," *IEEE Transactions on Industry Applications,* vol. 35, no. 3, pp. 646-656, 1999.

[17] A. C. Neto, A. L. Soares, G. B. Lima, D. Rodrigures, E. A. Coelho, and L. C. G. Freitas, "OPTIMIZED 12-PULSE RECTIFIER WITH GENERALIZED DELTA

CONNECTION AUTOTRANSFORMER AND ISOLATED SEPIC CONVERTERS FOR SINUSOIDAL INPUT LINE CURRENT IMPOSITION," *IEEE Transactions on Power Electronics,* pp. 1-1, 2018.
[18] C. Sewan, L. Bang Sup, and P. N. Enjeti, "New 24-pulse diode rectifier systems for utility interface of high-power AC motor drives," *IEEE Transactions on Industry Applications,* vol. 33, no. 2, pp. 531-541, 1997.
[19] M. Djuve and E. Hystad, "Low loss propulsion system."
[20] T. L. Baldwin and S. A. Lewis, "Distribution load flow methods for shipboard power systems," *IEEE Transactions on Industry Applications,* vol. 40, no. 5, pp. 1183-1190, 2004.
[21] C. Su, K. Lin, and C. Chen, "Power Flow and Generator-Converter Schemes Studies in Ship MVDC Distribution Systems," *IEEE Transactions on Industry Applications,* vol. 52, no. 1, pp. 50-59, 2016.
[22] S. Y. Kim, S. Choe, S. Ko, and S. K. Sul, "A Naval Integrated Power System with a Battery Energy Storage System: Fuel efficiency, reliability, and quality of power," *IEEE Electrification Magazine,* vol. 3, no. 2, pp. 22-33, 2015.
[23] J. Kim and J. Lai, "Analysis of a Shunt Wye–Delta Transformer for Multi-Generator Harmonic Elimination Under Non-Ideal Phase-Shift Conditions," *IEEE Transactions on Industry Applications,* vol. 55, no. 3, pp. 2412-2420, 2019.
[24] J. Lai and P. Venkatesh, "A shunt-connected phase-shift transformer for shipboard harmonics eliminating rectifiers," in *2016 Asian Conference on Energy, Power and Transportation Electrification (ACEPT)*, 2016, pp. 1-5.
[25] H. Oster. (2010, Dec 15 2019). *Low Loss Concept offers improved performance at lower cost*. Available: https://www.wartsila.com/products/marine-oil-gas/power-systems/electric-propulsion/electric-propulsion-systems/low-loss-concept/
[26] J. Millán, P. Godignon, X. Perpiñà, A. Pérez-Tomás, and J. Rebollo, "A Survey of Wide Bandgap Power Semiconductor Devices," *IEEE Transactions on Power Electronics,* vol. 29, no. 5, pp. 2155-2163, 2014.
[27] J. Palmour, "Power products rel data & pricing forecasts for 650V-15kVSiC power modules, MOSFETs & diodes," 2014.
[28] M. D. a. E. Hystad, "Low loss propulsion system," US Patent 11,570,015,June.6, 2005.
[29] P. Fang Zheng, "Application issues of active power filters," *IEEE Industry Applications Magazine,* vol. 4, no. 5, pp. 21-30, 1998.
[30] M. I. Mohammed, "Power Quality: Harmonics," in *Shipboard Power Systems Design and Verification Fundamentals*: IEEE, 2018, p. 1.
[31] H. Akagi, Y. Kanazawa, and A. Nabae, "Instantaneous Reactive Power Compensators Comprising Switching Devices without Energy Storage Components," *IEEE Transactions on Industry Applications,* vol. IA-20, no. 3, pp. 625-630, 1984.
[32] A. Hirofumi, W. Edson Hirokazu, and A. Mauricio, "The Instantaneous Power Theory," in *Instantaneous Power Theory and Applications to Power Conditioning*: IEEE, 2017, p. 1.
[33] Y. Xiaoming, W. Merk, H. Stemmler, and J. Allmeling, "Stationary-frame generalized integrators for current control of active power filters with zero steady-state error for current harmonics of concern under unbalanced and distorted operating conditions," *IEEE Transactions on Industry Applications,* vol. 38, no. 2, pp. 523-532, 2002.

[34] S. Buso, L. Malesani, and P. Mattavelli, "Comparison of current control techniques for active filter applications," *IEEE Transactions on Industrial Electronics,* vol. 45, no. 5, pp. 722-729, 1998.
[35] L. Malesani, P. Mattavelli, and P. Tomasin, "Improved constant-frequency hysteresis current control of VSI inverters with simple feedforward bandwidth prediction," *IEEE Transactions on Industry Applications,* vol. 33, no. 5, pp. 1194-1202, 1997.
[36] L. Malesani, P. Mattavelli, and P. Tomasin, "High-performance hysteresis modulation technique for active filters," *IEEE Transactions on Power Electronics,* vol. 12, no. 5, pp. 876-884, 1997.
[37] Q. Yao and D. G. Holmes, "A simple, novel method for variable-hysteresis-band current control of a three phase inverter with constant switching frequency," in *Conference Record of the 1993 IEEE Industry Applications Conference Twenty-Eighth IAS Annual Meeting*, 1993, pp. 1122-1129 vol.2.
[38] B. K. Bose, "An adaptive hysteresis-band current control technique of a voltage-fed PWM inverter for machine drive system," *IEEE Transactions on Industrial Electronics,* vol. 37, no. 5, pp. 402-408, 1990.
[39] L. Malesani and P. Tenti, "A novel hysteresis control method for current-controlled voltage-source PWM inverters with constant modulation frequency," *IEEE Transactions on Industry Applications,* vol. 26, no. 1, pp. 88-92, 1990.
[40] G. Wang and Y. W. Li, "Parabolic PWM for Current Control of Voltage-Source Converters (VSCs)," *IEEE Transactions on Industrial Electronics,* vol. 57, no. 10, pp. 3491-3496, 2010.
[41] R. I. Bojoi, G. Griva, V. Bostan, M. Guerriero, F. Farina, and F. Profumo, "Current control strategy for power conditioners using sinusoidal signal integrators in synchronous reference frame," *IEEE Transactions on Power Electronics,* vol. 20, no. 6, pp. 1402-1412, 2005.
[42] L. Herman, I. Papic, and B. Blazic, "A Proportional-Resonant Current Controller for Selective Harmonic Compensation in a Hybrid Active Power Filter," *IEEE Transactions on Power Delivery,* vol. 29, no. 5, pp. 2055-2065, 2014.
[43] C. Lascu, L. Asiminoaei, I. Boldea, and F. Blaabjerg, "High Performance Current Controller for Selective Harmonic Compensation in Active Power Filters," *IEEE Transactions on Power Electronics,* vol. 22, no. 5, pp. 1826-1835, 2007.
[44] P. Mattavelli, "A closed-loop selective harmonic compensation for active filters," *IEEE Transactions on Industry Applications,* vol. 37, no. 1, pp. 81-89, 2001.
[45] Y. Tang, P. C. Loh, P. Wang, F. H. Choo, F. Gao, and F. Blaabjerg, "Generalized Design of High Performance Shunt Active Power Filter With Output LCL Filter," *IEEE Transactions on Industrial Electronics,* vol. 59, no. 3, pp. 1443-1452, 2012.
[46] R. Teodorescu, F. Blaabjerg, M. Liserre, and P. C. Loh, "Proportional-resonant controllers and filters for grid-connected voltage-source converters," *IEE Proceedings - Electric Power Applications,* vol. 153, no. 5, pp. 750-762, 2006.
[47] A. G. Yepes, F. D. Freijedo, L. Ó, and J. Doval-Gandoy, "High-Performance Digital Resonant Controllers Implemented With Two Integrators," *IEEE Transactions on Power Electronics,* vol. 26, no. 2, pp. 563-576, 2011.
[48] S. Nirmal, K. N. Sivarajan, E. A. Jasmin, M. Nandakumar, and B. Jayanand, "Steady state error elimination and harmonic compensation using proportional resonant current

controller in grid-tied DC microgrids," in *2018 International Conference on Power, Instrumentation, Control and Computing (PICC)*, 2018, pp. 1-5.
[49] R. Teodorescu, F. Blaabjerg, U. Borup, and M. Liserre, "A new control structure for grid-connected LCL PV inverters with zero steady-state error and selective harmonic compensation," in *Nineteenth Annual IEEE Applied Power Electronics Conference and Exposition, 2004. APEC '04.*, 2004, vol. 1, pp. 580-586 Vol.1.
[50] H. Cha, T. Vu, and J. Kim, "Design and control of Proportional-Resonant controller based Photovoltaic power conditioning system," in *2009 IEEE Energy Conversion Congress and Exposition*, 2009, pp. 2198-2205.
[51] D. N. Zmood and D. G. Holmes, "Stationary frame current regulation of PWM inverters with zero steady-state error," *IEEE Transactions on Power Electronics,* vol. 18, no. 3, pp. 814-822, 2003.
[52] D. N. Zmood, D. G. Holmes, and G. H. Bode, "Frequency-domain analysis of three-phase linear current regulators," *IEEE Transactions on Industry Applications,* vol. 37, no. 2, pp. 601-610, 2001.